IMPERIAL COLLEGE LONDON

Dyson School of Design Engineering

Electrochemical Metal 3D Printing

A thesis submitted to Imperial College London for the Degree of PhD in the Dyson School of Design Engineering

Xiaolong Chen

Supervisors:

Dr Billy Wu — Dyson School of Design Engineering
Professor Peter Childs — Dyson School of Design Engineering

September 2018

谨以此文 献给我最亲爱的父母

This thesis is dedicated to my dear parent

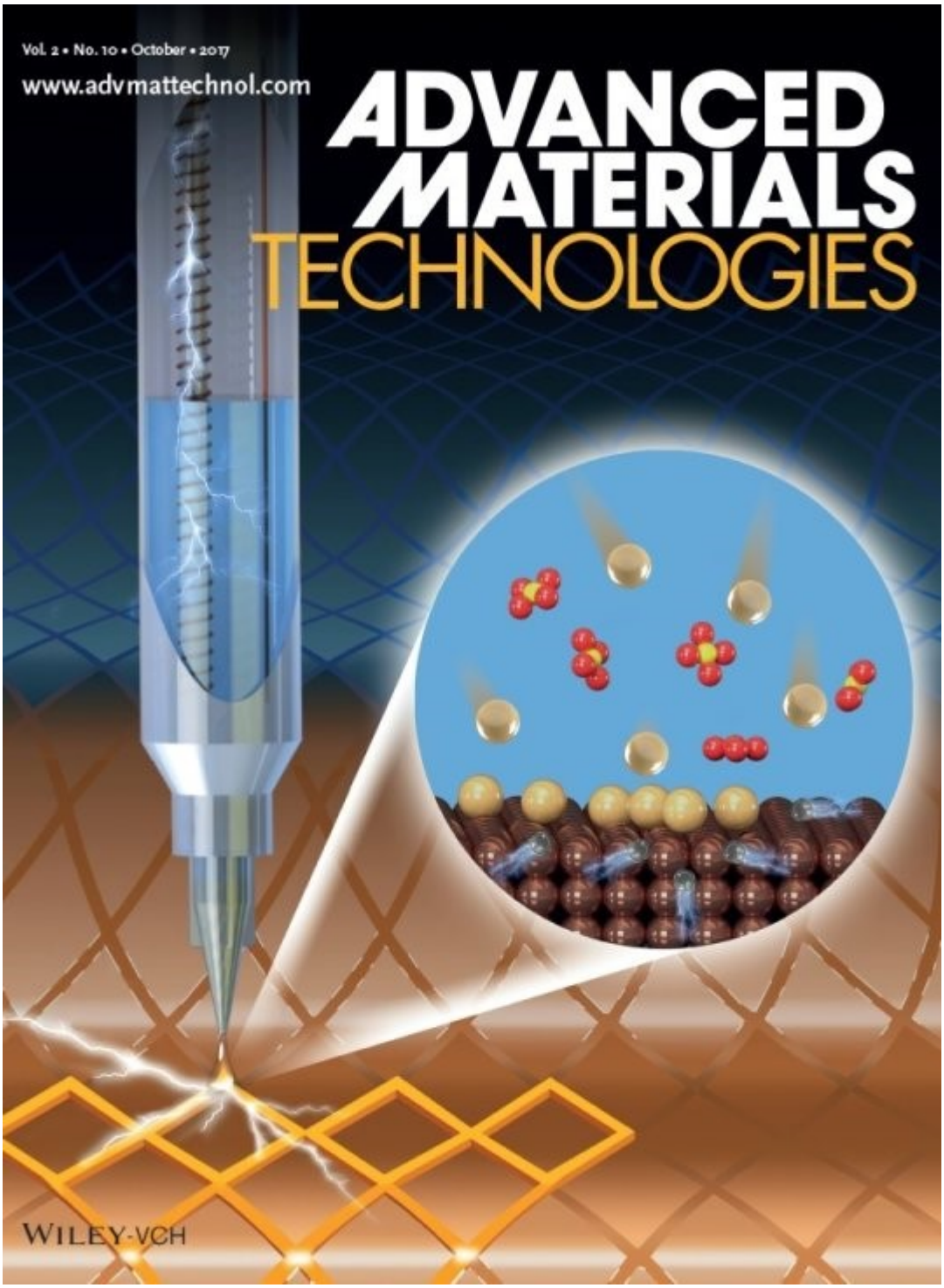

Inside Front Cover, ***Advanced Materials Technologies***, Volume 2, Issue 10

I hereby declare that this thesis and the work presented herein is my own work except where appropriated or acknowledges.

Xiaolong Chen

Acknowledgements

Firstly, I would like to sincerely express my gratitude to my supervisors Dr. Billy Wu and Professor Peter Childs. I was so fortunate to have their continued interest in my work and their invaluable guidance. They taught me how to be a good researcher, how to get over the problems and challenges. They also provided me with great opportunities to broaden my knowledge and introduced me to the world of academia.

I would also like to extend my thanks to Dr. Xinhua Liu and Professor. Nigel Brandon for their respective help and guidance in the field of electrochemical engineering through my PhD. I am also grateful to Dr. Sam Cooper and Dr. Gregory Offer for their assessment of my research work and invaluable advices.

I gratefully acknowledge the funding received towards my PhD from the Chinese Scholarship Council (CSC) and Imperial College London. I would like to thank all colleagues of design engineering research group and fuel cell battery research group: Mengzheng Ouyang, Yuhua Xia, Jingyi Chen. Their daily support, friendship and our discussion helped me to move forward. Doing lab with you is a relaxing time for me. Big thanks to all my friends, old and new, who have made the last few years so enjoyable.

Last but not least, I would like to acknowledge from the bottom of my heart the endless love and support of my family, especially: my parents, Peihua Chen and Shuying Liu, and my fiancé Fengyuan Liu. They all kept me moving forward and without them it would be very difficult to successfully complete my PhD project. I know that you are always there, whenever for whatever.

Disseminations

Journal articles

Chen, X., Liu, X., Ouyang, M., Song, B., Childs P., Brandon N.P., Wu B., 2019. **Fabrication of an integrated copper-fibre supercapacitor via a desktop electrochemical 3D printer.** *Journal of Energy Storage,* 26, p.100993

Chen, X., Liu, X., Ouyang, M., Chen, J., Taiwo, O., Xia Y., Childs, P., Brandon, N. P., Wu, B., 2019. **Multi-metal 4D printing with a desktop electrochemical 3D printer.** *Scientific Report.* 9 (1), pp. 1-9.

Ouyang, M., Boldrin P., Maher R.C., Chen, X., Liu, X., Cohen, L. F., Brandon, N.P., 2019. **A mechanistic study of the interactions between methane and nickel supported on doped ceria.** *Applied Catalysis B: Environmental,* 248, pp.332-340.

Liu, X., Marlow, M., Cooper, S.J., Song, B., Chen, X., Brandon, N.P., Wu, B., 2018. **Flexible All-Fibre Electrospun Supercapacitor.** *Journal of Power Sources,* 384, pp.264-269.

Chen, X., Liu, X., Childs, P., Brandon, N.P., Wu, B., 2017. **A Low Cost Desktop Electrochemical Metal 3D Printer.** *Advanced Materials Technology,* 2(10), p.1700148.

Conference papers

Chen, X, Wu, B. **Design and Fabrication of a low-cost electrochemical 3D printer.** *Proceedings of 3rd international Conference on Progress in Additive Manufacturing (Pro-AM),* Edited by C.K., Chua, W.Y., Yeong, M.J., Tan, E., Liu, S.B., Tor, Singapore, 2018. (ISSN: 2424-8967).

Conference presentations

Design and fabrication of a low-cost electrochemical 3D printer, Chen, X., **3***rd International Conference on Progress in Additive Manufacturing (Pro-AM),* Singapore, 16 May 2018.

Posters

Chen, X., Childs, P., Wu, B, 4D printing of multi-metal structures via a desktop electrochemical 3D printer. *2nd Additive Manufacturing Network.* London, UK, 19 Feb 2018.

Chen, X., Liu, X., Childs, P., Brandon, N. P., Wu, B. **A Desktop Electrochemical 3D Printer.** *China-Britain Joint Science and Technology Summit*, London, UK, 15 Nov 2017.

Chen, X., Childs, P., Wu, B. Design and modification of a Desktop Electrochemical 3D printer. *1st Additive Manufacturing Network.* London, UK, 5 Sep 2016.

Abstract

Additive manufacturing (AM) is the process of creating 3D objects from digital models through the layer-by-layer deposition of materials. Electrochemical additive manufacturing (ECAM) is a relatively new technique which can create metallic components-based on depositing layers of metal onto the surface of the conductive substrate through the reduction of metal ions. It is advantageous compared to other metal AM processes due to the absence of high temperature processes enabling a lower-cost and safer fabrication process, however, to date, all of the presented ECAM methods (Localized Electrochemical Deposition (LED) and Meniscus Confined Electrochemical Deposition (MCED) have been designed to achieve micro or nanoscale structures with limited deposition rates, and only focused on single material fabrication. Furthermore, all the printed structures are limited in the complexity of geometries, with the majority being wire-based architectures of porous and rough morphologies, with limited characterisation of the properties of the printed structures. Additionally, there is no available system able to create temperature-reactive multi-metallic functional 4D structures and no research has been presented on the potential application of ECAM in the field of electrochemical energy storage devices.

To bridge the gaps, this thesis investigates the development of a low-cost ECAM system capable of producing single and multi-metal structures by using multi-meniscus confined extrusion heads with volumetric deposition rates 3 times higher than what has previously been reported (~ 2×10^4 $\mu m^3.s^{-1}$), enabling large-scale fabrication of complex structures in multiple metallic materials. Scanning electron microscopy, X-ray computed tomography and energy dispersive X-ray spectroscopy measurements confirm that multi-metallic structures can be successfully created, with a tightly bound interface. Analysis of the thermo-mechanical properties of the printed strips shows that mechanical deformations can be generated in Cu-Ni strips at temperatures up to 300 °C, which is due to the thermal expansion coefficient mismatch generating internal stresses in the printed structures. Electrical conductivity measurements show that the bimetallic structures have a conductivity between those of nanocrystalline copper and nickel. Vicker's hardness tests, show that there is a clear correlation between the applied potential and the hardness of the printed product, with higher potentials resulting in a harder deposition. This increased hardness was found to be due to

the smaller grain sizes produced during higher potential deposition which restricted dislocation movement through the material.

Finally, this thesis presents the first reported combination of electrochemical 3D printing and electrospinning for building a high mass loading and high performance copper-fibre based supercapacitor which enables the potential to create more integrated electrodes and eventually to enhance the performance of supercapacitors. The results highlight the influence of the substrate conditioning and the resulting effects on the wetting characteristics of the meniscus and the subsequent distribution of the deposition which impacts the electronic conductivity of the overall electrode. In this the fibre-based supercapacitor was constructed, the carbon was doped with manganese oxides to enhance the capacitance through introducing pseudo-capacitance at the cost of electronic conductivity. With the printing of current collectors, a highly bound electrode-current collector interface was formed, reducing the interfacial resistance and enhancing the accessible capacitance at high scan rates.

In summary, this thesis presents work towards creating lower cost metal additive manufacturing through the development of an electrochemical metal 3D printer. A meniscus confined approach was taken to localise the deposition, with subsequent microstructural, mechanical and spectroscopic analysis of the printed product. Novel contributions to the field were further presented through developing understanding around multi-metal ECAM, with investigations around their coupled thermo-mechanical properties. Finally, the applicability of this approach was investigated in the field of electrochemical devices, where the influence of a porous substrate was investigated, whereby tightly bound and highly conductive current collectors were printed onto fibre based supercapacitors, enhancing their accessible capacitance. This work, therefore, demonstrates the potential for the ECAM approach in a diversity of applications.

Table of Contents

List of Figures

List of Tables

List of Abbreviations

1D	One Dimensional
2D	Two Dimensional
3D	Three Dimensional
4D	Four Dimensional
ABS	Acrylonitrile Butadiene Styrene
AFM	Atomic Force Microscope
AM	Additive Manufacturing
CAD	Computer Aided Design
CCD	Charged Coupled Device
CFRP	Carbon Fibre Reinforced Polymer
CNC	Computer Numerical Control
CT	Computed Tomography
Cu	Copper
DED	Direct Energy Deposition
DMD	Digital Micro-mirror Device
DMLS	Direct Metal Laser Sintering
DOD	Drop-on-demand
ECAM	Electrochemical Metal Additive Manufacturing
EDS	Energy Dispersive x-ray Spectroscopy
EFAB	Electrochemical FABrication
EPSRC	Engineering and Physical Sciences Research Council
FDM	Fused Deposition Modelling
FFF	Fused Filament Fabrication
HV	Hardness Value

LED	Localized Electrochemical Deposition
LOM	Laminated Object Manufacturing
MCE	Meniscus Confined Electrode
MCED	Meniscus Confined Electrochemical Deposition
Ni	Nickel
PA	Polyamide
PC	Polycarbonate
PLA	Polylactic Acid
PP	Polypropylene
PED	Pulsed Electrochemical Deposition
SEM	Scanning Electron Microscopy
SL	Stereolithography
SLS	Selective Laser Sintering
SMPs	Shape Memory Polymers
UV	Ultraviolet

List of Notations

Θ	Folding angle
ϕ	Porosity
w	Weight of the electrode
γ	Surface energy
ρ	Resistivity
$p_b - p_a$	Pressure drop
Q	Flow rate
K	The intrinsic permeability of the medium
A	The cross-sectional area of the flow
d	The diagonal length of contact area
F	Applied load
I	Current according to the applied potential
l	Length between the measurement points
L	Length of the pressure drop
V	Applied voltage
$Z_b - Z_a$	Height of the fluid

Chapter 1 Introduction

1.1 Background

Additive manufacturing (AM) (3D printing) is the process of creating complex 3D geometries, through the layer-by-layer solidification of material, as opposed to traditional subtractive manufacturing methodologies [1]. The design freedom offered by the AM of metals has seen industrial uptake in aerospace [2, 3], automotive [4] and medical [5] applications (Figure 1.1). Metal 3D printing has broad industrial and consumer applications due to the ability to create complex geometries from engineering metals such as stainless steel and titanium without the need for costly tooling [6]. Of the metal AM processes, direct metal laser sintering (DMLS) is the most common and works through the selective laser sintering of layers of metal powders [7, 8]. However, the high capital cost, use of hazardous metal powders, component defects, inability to work with multiple materials and need for inert gases has limited its broader use [9]. Thus, there is a need to develop novel non-laser based 3D printing techniques for metals which enable multiple materials to be deposited at reduced cost in order to unlock functional structures.

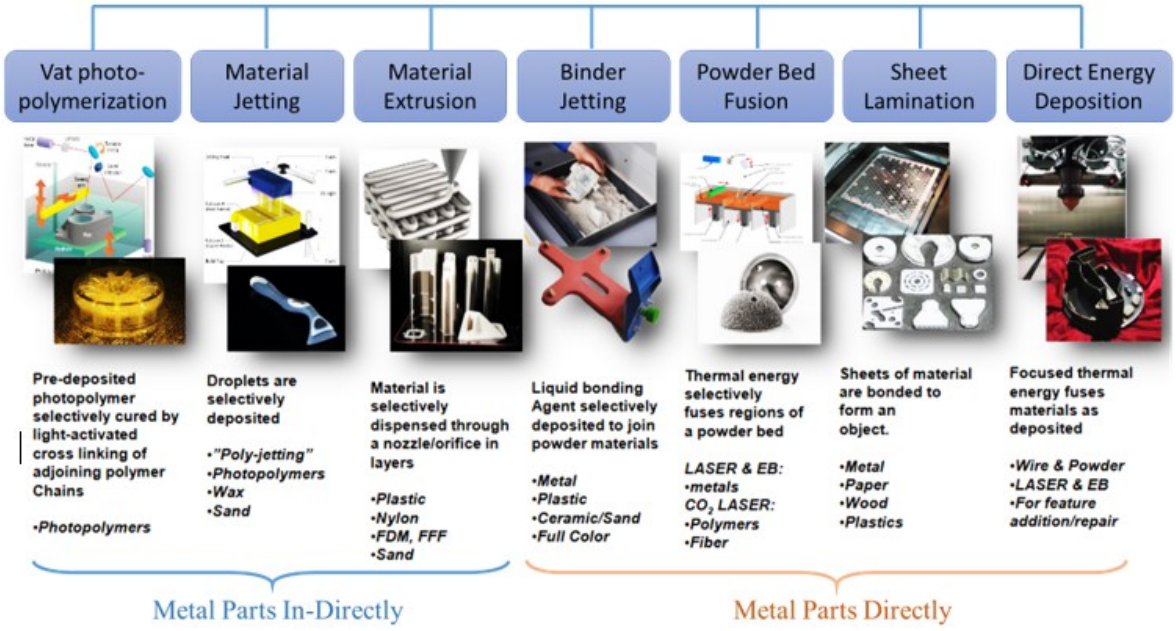

Figure 1.1 Traditional Additive Manufacturing processes [10].

Electrochemical additive manufacturing (ECAM or electrochemical 3D printing) is a relatively new form of metal 3D printing that deposits thin and highly adherent layers of

metals onto the surface of a conductive substrate through the reduction of metal ions in a solution [11, 12]. There have been two main approaches developed to build an electrochemical metal 3D printer; a meniscus-confined pipette and a localised deposition approach. The meniscus-confined process exploits the stability of a liquid meniscus to print 3D metal structures in ambient air conditions [13] Localised electrochemical process uses an ultra-sharp electrode submerged in an ionically conductive electrolyte close to a conductive substrate where the deposition occurs [14]. However, both techniques have slow deposition rates ranging from ~100 $nm.s^{-1}$ to ~0.18 $nm.s^{-1}$ or 0.008 -20.4 $\mu m^3.s^{-1}$ which remains the main barrier to enlarging the products scale from the micro or nano to macro [15].

Furthermore, all the printed products are limited in the complexity of geometries, with the majority of products bring wire-based architectures featuring rough morphology and porous detailed structures [16, 17] and are made from a single metal.

1.2 Research aim and objectives

The main aim of this project is the development of a meniscus confined low cost electrochemical metal 3D printer with improved deposition rates and capabilities. In the meniscus confined deposition process, a stable meniscus acts as a bridge connecting nozzle and conductive substrate to precisely guide the metal deposition.

The objectives to achieve this aim are as follows:

- To understand the underpinning factors which limit ECAM approaches to metal 3D printing.
- To design and develop a new meniscus confined extrusion head capable of producing stable meniscus at an increased deposition rate.
- To understand the key parameters, such as nozzle size, solution concentration and deposition potential, required to produce high quality metal parts.
- To evaluate the developed system, printing metal dots, lines and complex architectures and to characterise physical properties (e.g. hardness test and conductivity test).
- To apply this technique in fabricating functional products, such as bimetallic strips and supercapacitors through multi-metal ECAM.

1.3 Outline of Thesis

The thesis, based on published and submitted journal and conference papers, is divided in seven chapters, which progress in accordance with the identified research objectives. The first chapter comprises an introduction that in addition to listing the key objectives and the novelty of this research, also briefly describes the context of the research. The contents of the remaining chapters are summarized below:

Chapter 2: Literature review

- This chapter introduces the state-of-the-art in AM techniques comprising various types of manufacturing processes, materials and applications and identifies the current gaps in the academic literature. It consists of five main sections:
  (i) Review of all kinds of AM processes, including stereolithography, inkjet printing, selective laser sintering, fused deposition modelling, material extrusion and laminated object manufacturing;
  (ii) Review of the developments of all types of ECAM techniques, including mask-based, probe-based and pipette-based approaches. An emphasis on the meniscus confined electrochemical deposition process is also included, comprising the developments of the technique, the formation of meniscus and associated influence factors.
  (iii) Review of electrochemical theory in meniscus-confined electrochemical deposition process, as well as the key aspects for high-quality structures printing in terms of meniscus stability maintenance, evaporation in the process and substrate properties.
  (iv) Review of four-dimensional (4D) additive manufacturing techniques where smart materials are combined with 3D additive manufacturing techniques. Related researches using thermal, humidity and current stimuli smart material are reviewed.
  (v) Review of applications of AM techniques in the field of electrochemical energy storage devices including sandwich-type configurations and in-plane type configurations.

Chapter 3: Design and fabrication of a low-cost desktop electrochemical 3D printer

- This chapter describes and compares two proposed print head designs, the gear-assisted print head and sponge-assisted print head respectively, for the developed system (Desktop Electrochemical 3D Printer). The content of this chapter corresponds to the optimization process of the printer design, and the definitive use of sponge-assisted print head allows for higher volumetric deposition rates compared

with other electrochemical manufacturing approaches. The influence of deposition potential and concentration are also shown for copper deposition from an aqueous copper sulphate solution. Furthermore, optimization of the nozzle infill material is presented, using an electrospun fibre mat for improved consistency and the efficiency of the deposition process. 2D CAD drawings of fabricated parts of the printer are presented in Appendix A, while devices selected for the printer are included in Appendix B. Appendix C presents the cost of the system.

Chapter 4: 3D printing and characterisation of single dots and lines

- This chapter assesses the capability of the Desktop Electrochemical 3D printer by printing metal dots, lines and letters. The meniscus confinement approach is described. The novel design prints polycrsytalline copper structures at a volumetric deposition rate 3 order of magnitude higher than other equivalent systems. The printed structures are assessed from a morphological, mechanical (Vickers hardness) and electrical perspective. The results verified the printability of the system with a fast deposition speed, especially for large-scale single metallic (copper) structure fabrication. Indentation and resistivity tests suggest that the nanocrytsalline printed structures have increase hardness and resistivity compared to cold worked course grained copper.

Chapter 5: Metal 4D printing of multi-material structures with a desktop electrochemical 3D printer

- This chapter presents the further development of the electrochemical 3D printer with two deposition nozzles for multi-material 4D printing. An improved version of nanofiber-assisted print nozzle is described. The mechanism of shape morphing has been explored by printing pure copper strip, Cu-Ni bilayer strip and Cu-Ni-Cu trilayer strip. A systematic assessment of impact factors, such as layer thickness, temperature, deposition position, metallic conductivity and metallic surface morphology has been investigated. The results show the possibility shaping the multi-material multi-layer strips by changing temperature and altering the layer thickness, allowing for fabricating functional and customized thermally responsive materials. This work thus explore basic research of in multiple metals shape morphing with expanding research in the complex metal 4D printing.

Chapter 6: Fabrication of an integrated copper-fibre supercapacitor via a desktop electrochemical 3D printer

- This chapter presents the application of the developed desktop electrochemical 3D metal printer for the optimization of energy storage for an all-fibre flexible supercapacitor.

Chapter 7: Conclusions

- This chapter provides an overall summary of the thesis and main conclusions that can be drawn from the research work carried out. Possible future directions for research following on from this thesis are also presented.

The structure of the thesis therefore is divided into four main sections of technical content (Figure 1.2). The first chapter describes the design and fabrication of the low cost desktop electrochemical 3D printer with emphasis on the development of print head. The following two chapters illustrate the experimental validation of the 3D printer including initial validation of printing single-material dots, lines and letters, and further validation of multi-material multi-layer structures. The final chapter then applies the developed 3D printer in optimizing the all-fibre flexible supercapacitor in terms of energy charge storage

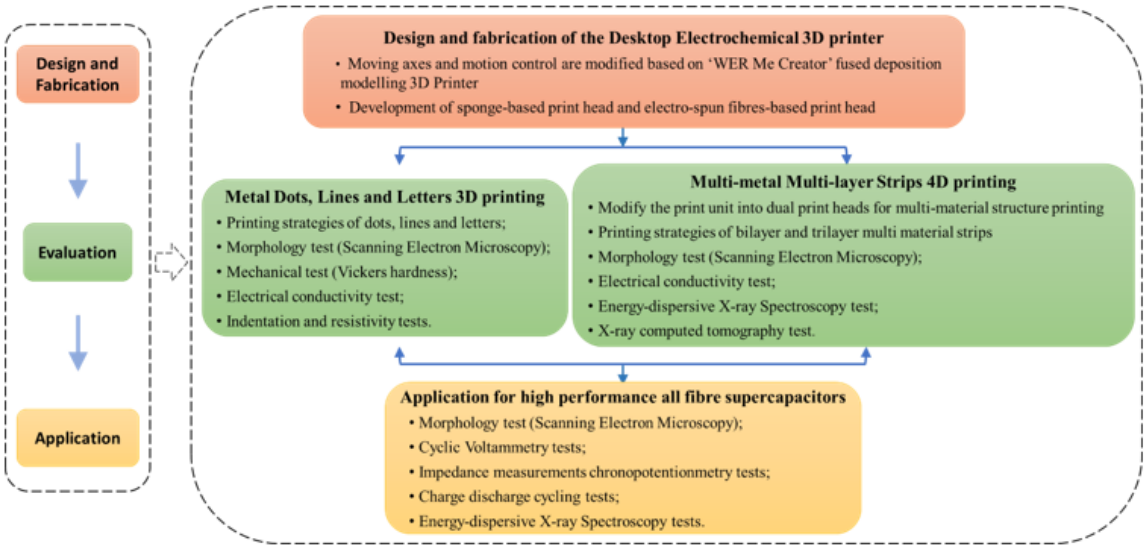

Figure 1.2 Overview of structure of PhD project.

Chapter 2: Literature Review

2.1 Additive manufacturing techniques

AM is defined as a process to produce 3D products from computer model data by depositing successive layers of material, which is opposite to the traditional subtractive manufacturing approach [18]. Several factors are considered to choose a suitable fabrication technique such as the product complexity, material, number of replicates and cost [19]. AM approaches have the advantage in the degree of freedom for complex designs, for example, lattice structures can only be easily obtained by AM techniques with material waste also being low due to the additive nature of the manufacturing process [20]. While subtractive manufacturing is appropriate for a large number of replicates in a short time in a lower cost.

The processes of 3D AM (Figure 2.1) are listed as follows [19]:

(i) The creation of a 3D model; 3D models can be obtained by computer-aided design (CAD) software, 3D scanner and photogrammetry through a combination of photos taken from different directions.

(ii) STL file generation; the STL file is regarded as a universal format for all 3D printers, where the model surfaces are divided into a list of coordinates of triangulated sections

(iii) Slicing and tool path generation; the slicing process is usually conducted with a function embedded in the 3D printer software. Certain number of 2D cross sections are created from the entire object after defining the layer thickness. The tool path, usually presented in G-codes, is generated based on the cross section. It should be noted that the layer thickness is crucial in order to achieve a high surface finish.

(iv) Printing process.

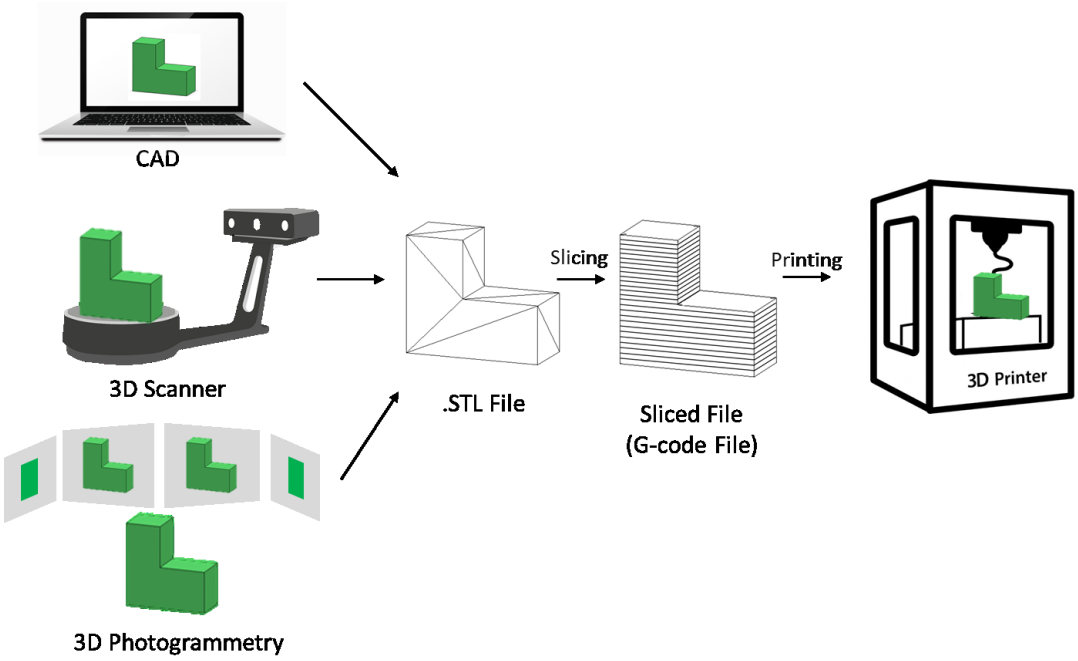

Figure 2.1 Schematic illustration of 3D printing process.

The first form of 3D printer was developed by Charles Hull from the University of Colorado (US) in the early 1980s for fabricating plastic models and prototype parts from photopolymers [21]. This type of fabrication process continued to develop and was termed 'Stereolithography' (SL), and the first commercial 3D printer called SL-250 was developed by 3D SYSTEMS established by Hull in 1986 [22]. From then on, AM has gone through a rapid development including the inventions and commercialization of different types of printing techniques [23], the extended use of various materials such as plastics[24], metals [8], ceramics [25] and composites [26], and the broad applications in the fields of automotive [27], aerospace [28], chemical [21], food [29], medical [30] and fashion [31]. Currently, AM techniques are traditionally grouped into six categories based on the mechanism/principle of solidification of material: (1) stereolithography, (2) inkjet printing, (3) selective laser sintering (SLS), (4) fused deposition modelling (FDM), (5) material extrusion (6) laminated object manufacturing (LOM). The characteristics and achievements of the above techniques are discussed in the following sections.

2.1.1 Stereolithography

SL (Figure 2.2), as introduced above, was one of the first employed and commercialized 3D printing techniques. SLA is divided into direct/laser writing (Figure 2.2a) and mask-based digital light curing (Figure 2.2b) approaches. The direct/laser writing system consists of a laser (or UV light beam) moving across the surface of the liquid resin to cure the layer covering the surface, and then the stage moves lower by one layer thickness. This curing process repeats until the whole product is complete. In this configuration, the stage is located below the liquid resin [32]. While the mask-based digital light curing approach use digital

mirror device (DMD) to cure one whole layer of resin between the laser and the stage. The stage then rises with one layer thickness, and the curing process is repeated until the whole product is printed. In this configuration, the stage is submerges with a certain distance into the resin. Compared to the traditional direct/laser SLA technique, which is time-consuming, the projection-based approach can cure an entire layer at once since it uses a DMD consisting of millions of mirrors working as a mask allowing for a greatly reduced printing time [33].

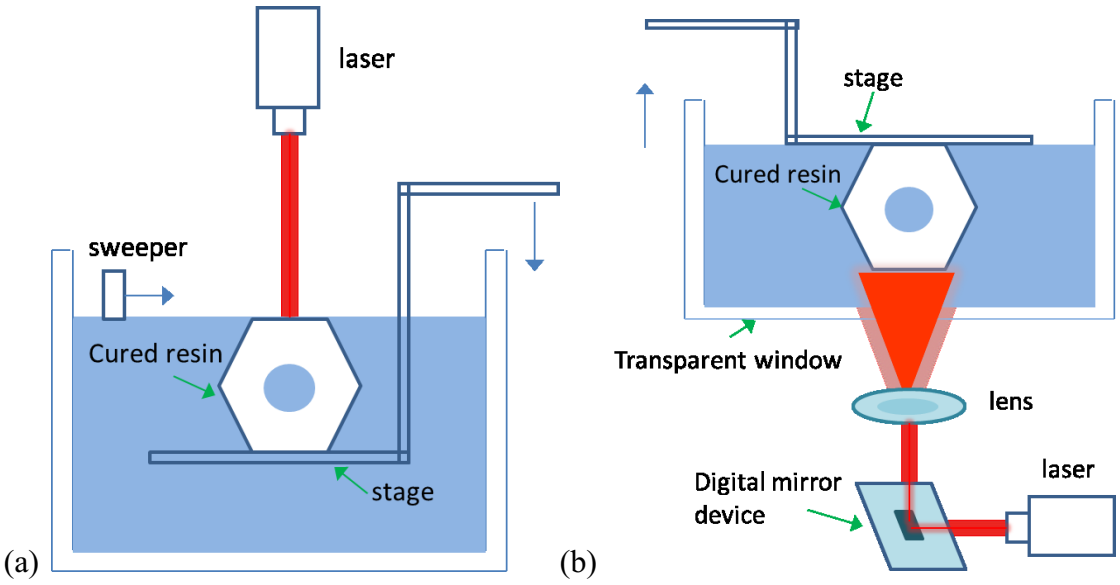

Figure 2.2 Schematics of (a) direct/laser writing SLA printer; (b) mask-based SLA printer.

The resolution in the vertical direction depends on the cured layer thickness, and the diameter of the UV beam determines the lateral resolution (80-250 μm) [34, 35]. Two photon polymerization (TPP) utilized a femtosecond laser in SLA fabrication, allowing for the printing of micro/nanoscale structures [36]. The SLA technique has the advantages in terms of high resolution and efficiency. Resins, either epoxy or acrylic bases, limit the application of SLA since the choice of UV light source depends on the resin. Moreover, the device design is limited as only one resin can be used at a time.

2.1.2 Inkjet printing

Inkjet printing was initially patented as a Reyleigh break-up inkjet device by Rune Elmqvist, in 1951 [37]. Currently this technique has been developed into two main types, called continuous and drop-on-demand (DOD) printing. the continuous inkjet printing technique was developed by Sweet from Stanford University in the 1965 [38]. The droplet size and spacing are controlled by piezoelectric module, and are directed onto platform or recycled into a waste compartment (Figure 2.3a). The DOD printing technique was firstly developed by Zoltan in 1972 [39], which deposits a cartridge of ink to build up a multi-layer structure in a predesigned printing process. The size of the printed droplets is precisely controlled by the pressure pulses generated by a thermal or piezoelectric actuator (Figure 2.3b). The

continuous inkjet printing is mainly used for high-speed graphical printing on papers, such as labelling, or textile printing. DOD inkjet printing is more often used due to the smaller droplet size and higher deposition accuracy. The DOD thermal inkjet printers use the quick temperature increase controlled by the heating element (ink contacted with the heating element was heated up to ~300°C in a few microseconds to generate vapour bubbles as the drive force to eject ink droplets and deposit on the substrate. While the DOD piezoelectric inkjet printers use the pressure increase generated by applying the piezoelectric changes [40].

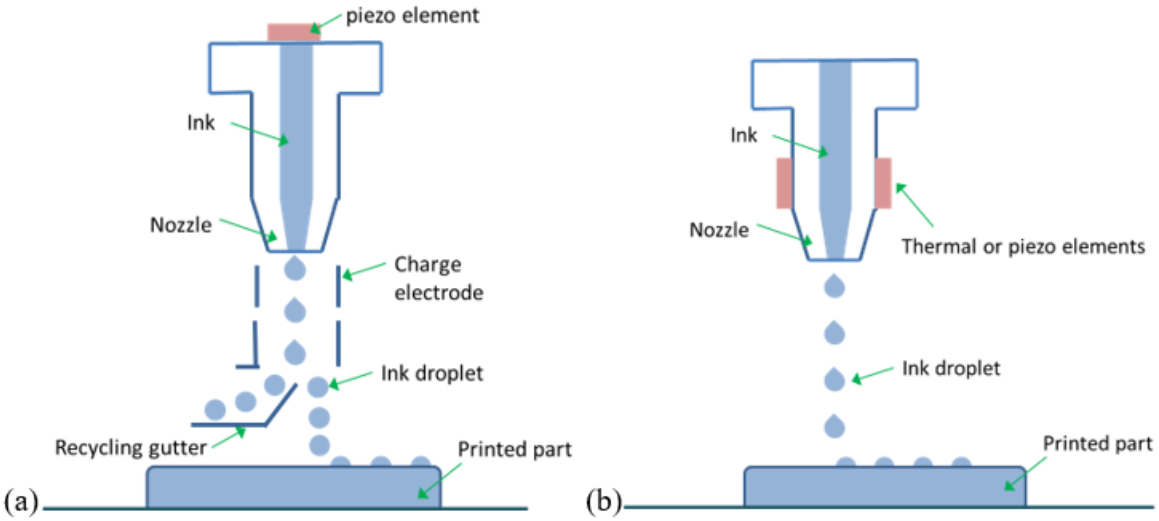

Figure 2.3 Schematics of (a) continuous inkjet printing system; (b) drop-on-demand inkjet printing system.

The ink and its associated properties, such as viscosity and surface tension, are crucial in the inkjet printing technology. In order to avoid too much kinetic energy and shear stress, low viscosity ink is preferred, which is typically below 20 mPa·s [41]. So that inkjet printing is limited to low viscosity material. Inkjet printing has been referred to be the printing process of high resolution, fast speed [42]. The parallel working mode with multiple jets gives rise to the fast printing speed.

2.1.3 Selective laser sintering

Selective laser sintering (SLS) was developed by Carl Deckard and Joseph Beaman at the University of Texas-Austin in 1990 [43]. The powder bed-based SLS process (Figure 2.4a) is similar to SLA, with the liquid photopolymer being replaced by powder, with particle size ranging between 50-100 μm [44]. It uses a laser source to sinter the powder layer, evenly distributed on the top of the build platform by a roller, at desired areas of solidification. After the first layer is completed, the stage moves down by one layer thickness, and the steps are repeated until the final model is generated. Blown powder deposition (Figure 2.4b), also known as a form of Direct Energy Deposition (DED), is a converted AM technique based

on powder bed-based SLS technique. During the laser deposition process, powder is delivered from the jet by pneumatic control of inert gas [45].

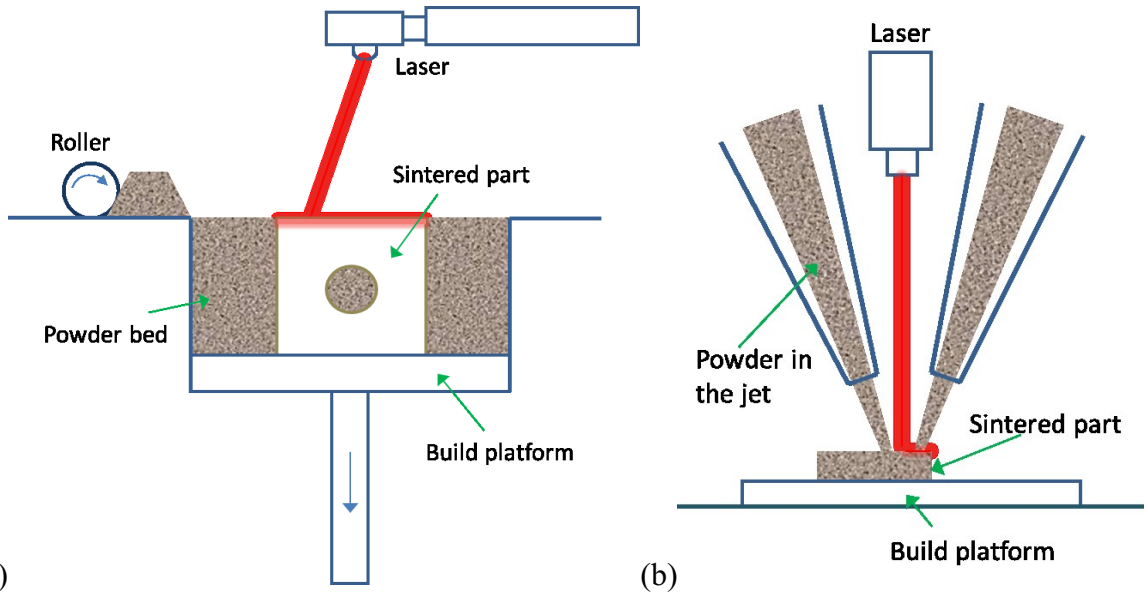

Figure 2.4 Schematics of (a) powder bed-based SLS process; (b) blown powder deposition process.

A large variety of materials including plastic, ceramics, metals, nylon and acrylic powders can be used in the SLS process. One major advantage of this configuration is that there is no support structure needed (in certain materials) as the unbounded powder works as material support during the process and can be removed and recycled after fabrication. the resolution is dependent on processing parameters, including laser power, laser focusing and the size of powder material, which is roughly 50 µm [46]. Also, DED has the potential to create complex geometries, including parts with internal cavities, the repair and modification of existing components, the fabrication of fully dense and high strength components and the creation of bi-metallic or gradient material structures [45, 47, 48], especially for applications in aerospace and automotive industries. In this configuration, the resolution is related to laser power, powder flow rate, process feed rate and powder size [45]. In both techniques, the major drawback is the shrinkage and deformation sue to the heating and cooling process, and it is dependent on the solidification rate [49, 50].

2.1.4 Fused deposition modelling

Fused deposition modelling (FDM) uses a polymer filament which is unwound from a material spool by a roller or gear and fed into a temperature controlled extrusion nozzle (Figure 2.5). The filament is melted in the nozzle and specifically deposited onto the build platform where the polymer cools and solidifies. This is repeated in a layer by layer process to fabricate a 3D structure. Support structures may be required for overhanging features or to anchor the build part to the platform. The technology was initially developed in the late

1980s by Scott Crump who went onto commercialise the technology by co-founding Stratasys Inc. [51, 52]. The term fused filament fabrication (FFF) is a synonymous term for FDM which allows unconstrained usage and was popularised by the RepRap project, an open-source self-replicating rapid prototyping machine [53]. Common polymers for both the model and support structures are polylactide (PLA), acrylonitrile butadiene styrene (ABS), polycarbonate (PC), polyamide (PA), polypropylene (PP), and mixtures of thermoplastic polymers [54-56].

The expansion of FFF hardware coincided with the expiration of patents associated with FDM in 2007 and the development of the open-source RepRap community. The RepRap project has served as the foundation of start-ups worldwide which have expanded the range FFF hardware available whilst lowering costs. An estimated 278,385 low-cost (< $5,000) FFF machines were sold worldwide in 2015 compared with only 66 in 2007 [57].This has enabled the wide adoption of FFF technology in industry for rapid prototyping and final part fabrication, furthermore, educational institutes are utilising the technology for educational purposes.

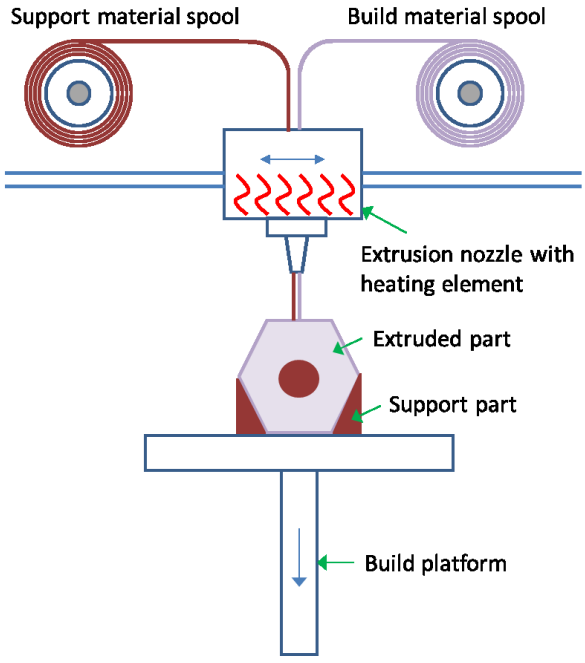

Figure 2.5 Schematic of Fused Deposition Modelling.

FFF has traditional been used for model making and prototyping as the filaments used are typically not strong enough for load-bearing applications [58, 59]. However, the development of composite filaments has enabled FFF to be utilised in a wider range of industries and for final product fabrication. For example, the addition of carbon fibres to polymer filaments results in the creation of carbon fibre reinforced polymer (CFRP) which increases the polymers mechanical properties [60, 61]. This has enabled CFRP filament

composites to be utilised in fabrication of components for the aerospace, automotive, energy (turbine blades), and medical (endoscopic surgery) industries [62-64]. Moreover, the addition of metals into polymer matrices has been investigated to produce composites with unique properties [65, 66]. Copper and iron particles have been introduced into ABS to produce composite filaments [67]. The copper-ABS composite exhibited improved thermal conductivity and increased tensile strength with increasing metal content. The improvement in thermal conductivity can also reduce thermal expansion of the thermoplastic during the printing process thus reducing distortion in the final product. The composite material could be used in large-scale 3D objects where distortion needs to be minimised and in 3D printed electronic circuits and electromagnetic structures.

The FDM process is a more cost effective technique where the machines and materials are less expensive. In addition, no chemical post-processing and curing process is required. While the resolution in z direction limits its application in the precise machining. A finishing process is needed if a smooth surface is required. Moreover, it often takes days to build up a complex large part. FDM technique has been applied to a wide range of applications including aerospace, automotive and energy industries because of the low cost of the machines and the superior mechanical properties of the printed samples. There are, however, limitations of this technique in terms of build speed, accuracy and material density. A major limitation of FDM is the requirement of a polymer filament for extrusion which restricts the materials available for printing.

2.1.5 Material extrusion

Systems have been developed based on material extrusion-based processes which utilise material chambers rather than the filaments used in FDM. This offers flexibility in material selection based on the use of pneumatic, piston, and screw assisted extrusion systems enabling a wider variety of materials to be used. The primary methods of extrusion with a material chamber are either using pneumatic or mechanical assistance, utilising a piston or a screw, to apply the extrusion force (Figure 2.6).

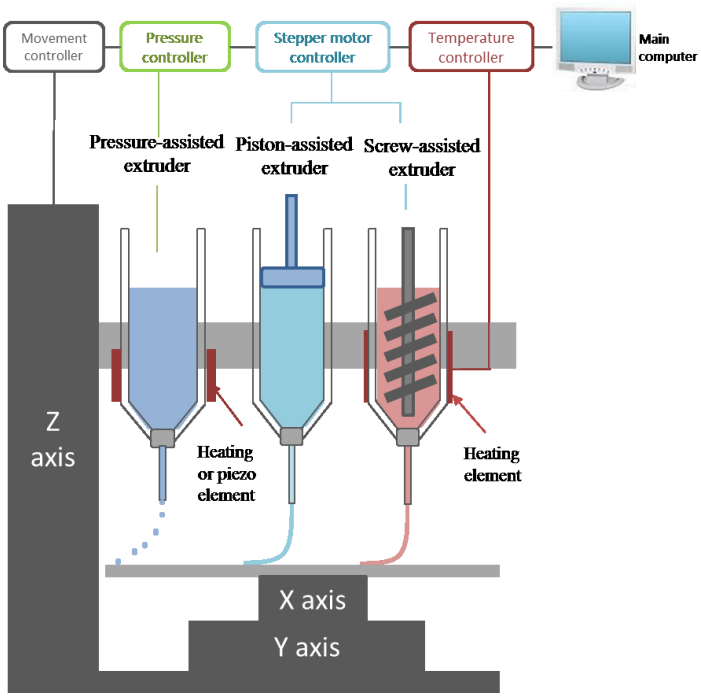

Figure 2.6 Schematic of Material Extrusion with pneumatic-assisted extruders, piston-assisted extruders and screw-assisted extruders.

Pneumatic extrusion is based on the use of a compressed gas to provide pressure which forces the material through a nozzle onto the build platform (Figure 2.6). The extrusion process is straightforward and easy to control by directly adjusting the gas pressure. Additionally it is more suitable for low viscosity material extrusion [68]. However, using pneumatic generated force to extrude polymers and polymer composites can require high temperatures to reduce the viscosity to allow printability [69]. Furthermore, the deposition process can be slow due to the limited force applied to the material that results in long print times especially if the material has a high viscosity and is temperature sensitive.

Piston-assisted extruders use a linear actuator to push a piston to force a material out of a nozzle (Figure 2.6). Compared with pneumatic extruders, the feed rate of the piston can be precisely controlled by the stepper motor [70]. This allows more precise control of material extrusion as there is no delay due to the compression of the gas volume as is typical in pneumatic-assisted systems. Furthermore, greater force can be utilised which allows more viscous materials to be extruded.

Screw-assisted extrusion, which can be termed precision extruding deposition (PED), was initially developed by Bellini *et al*. [71] at Drexel University. The system consists of a rotational screw, driven by stepper motors, to mix and force the material out of a nozzle (Figure 2.6). Almeida *et al*. [72] improved this design by including an additional temperature controlled material chamber in which the material can be liquefied and fed into the screw chamber using air pressure. Compared with the previous types of extruders, screw extruders

present more precise deposition ability, faster deposition velocity, improved material mixing, and greater suitability to manipulate materials with high viscosity [73].To achieve precise material deposition, the positioning system must be accurate but also the parameters associated with material extrusion such as deposition velocity, screw rotational speed, and temperature should be optimised.

Material extrusion has been applied mainly in the bioengineering field, which is also called bioextrusion. A wide range of materials, such as biopolymers, hydrogels, and cells can be used for building up the tissue mimic structures.

2.1.6 Laminated object manufacturing

Laminated Object Manufacturing (LOM), is one of the first commercialized AM methods, which was initially developed by Helisys [74]. It utilized sheets materials such as papers, plastic and metal [75], to fabricated 3D model by stacking layers of material togeher. One layer of a sheet material is rolled to the build platform, and then a laser traces the designed pattern on the layer of material according to the information of cross section. A heated roller is then used to help bonding the new layer to the previous layers (Figure 2.7).This process is repeated until all the layers for the 3D model are completed. Example systems include the use of paper [76] or metal [77] with the used of adhesive and welding used to fuse the layers together, respectively.

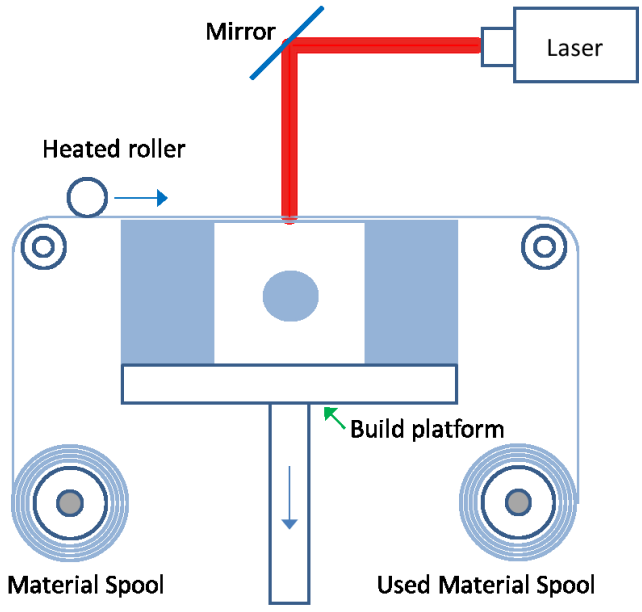

Figure 2.7 Schematic of the LOM process.

LOM has been used for a variety of materials, such as polymers, polymer composites, paper and metal-filled tapes. The temperature control of the roller is vital as the part could be fragile due to insufficient temperature, or the part could be damaged due to overheat [78]. Post processing, such as high temperature treatment, is also required depending on type of

materials and desired properties. Also, the heating process leaves large residual stress in the fabricated part. LOM is advantageous in fabricating large structures which could be done in the open air. It has been used in a wide range of industries, however, the materials applied to LOM are limited as they have to be formed into sheets and integrated with adhesive. Additionally, the surface finish and resolution are comparably poor. Also, it is time-consuming for removing the excess parts of laminates after fabrication of the objects. It is not recommended for fabricating complex structures.

2.1.7 Summary of traditional additive manufacturing techniques

Based on the literature review of the common additive manufacturing techniques, the advantage and disadvantages of AM techniques are summarized respectively as below:

Advantages:

- Large freedom of design and high complexity. AM techniques allow for manufacturing extremely complex shapes by engineering novel materials such as semi-crystalline polymer composites without the need for bespoke tooling.
- Small production quantities. AM is more cost-effective for lower production volumes compared to traditional manufacturing methods. Prototype parts can be printed faster than conventional methods, such as moulding, forging and milling.
- On demand manufacturing. AM is capable of manufacturing parts on demand, and therefore reducing the maintenance time.
- Easy public access. CAD models can be easily shared to reproduce the same design. There is no need to accept strict technical training before using any AM machines.

Disadvantages:

- Poor interlayer bonding strength leads to reduced mechanical properties.
- Anisotropic behaviour of the printed components results from the layer-by-layer production approach.
- Inaccuracies and defects involved in the process of transferring CAD into 3D-printed parts. The error is more apparent in curved surfaces due to the tessellation concept of CAD.

Table 2.1 shows the summary of the main methods of traditional AM in terms of materials, applications, benefits, drawbacks and range of resolution.

Table 2.1 the summary of the main methods of traditional additive manufacturing in terms of materials, applications, benefits, drawbacks and range of resolution

AM techniques	Materials	Applications	Benefits	Drawbacks	Resolution (μm)
Stereolithography (STL)	Resin with photo-active monomers Polymer-ceramic composites	Prototype Biomedical	High resolution High quality	Limited applied materials High cost Long printing time	10 μm [79]
Inkjet Printing	Liquid material (ink or paste) Ceramic, polymers and concrete	Biomedical	Wide range of applied materials Quick printing	Lack of adhesion between layers Coarse resolution	5-200 μm [80, 81]
Selective laser sintering (SLS)	Metals and alloys powder or wire Ceramics, polymers	Biomedical Electronics Aerospace Lightweight structures	High resolution High quality	High cost Long printing time	80-250 μm [82, 83]
Fused deposition modelling (FDM)	Thermoplastic polymers in the form of filaments	Prototype Composite parts	Low-cost High speed Easy to process	Weak mechanical properties Limited applied materials	50-200 μm [84, 85]
Material extrusion	Polymer, polymer-ceramic composites, food, concrete	Biomedical Large structures Buildings	Able to print large structures Quick printing Wide range of applied materials	Lack of adhesion between layers Coarse resolution	10-500 μm [86]
Laminated object manufacturing (LOM)	Polymer composites Paper Metal-filled tapes Metal rolls	Model Making	Reduced tooling and manufacturing time Low cost Able to print large structures	Poor surface quality and dimensional accuracy Limitation in fabricating complex structures	Depend on the thickness of the laminates [87]

2.2 Electrochemical additive manufacturing

All the traditional AM processes show limitations in terms of interlayer binding, strength, resolution, and surface finish of the fabricated microstructures. For example, during the inkjet printing and material extrusion processes, the clogging of the nozzle impedes the jetting and extrusion processes [88]. Also the thermal gradient involved in the SLS/SLM process results in the residual stresses (>200 MPa) which limits the wall thickness of the fabricated parts and causes undesirable mechanical deformation [89]. Also, the traditional AM machining processes often require complex systems, such as inert gas chamber for SLM to reduce oxidation [90]. Moreover, support structures are required for overhanging features in traditional AM processes. It is very difficult to remove the support structures, especially in micro-/nano- scales, and the removal process involves risks in the damage of delicate features and part distortion [91].

ECAM is a relatively new form of AM that deposits thin and highly adherent layers of metal onto the surface of a conductive substrate through the reduction of metal ions in a solution [92]. This technique combines electroplating technique and AM principles to achieve a novel AM process. Comparing to the traditional laser- and sintering-based AM techniques for metallic structures fabrication, ECAM is a non-thermal process which is advantageous in minimizing the thermal effects, full-scale control over the growth of deposition allowing for greater flexibility in avoiding support structures [93]. So far, ECAM has been applied in micro-/nano- fabrication as deposition rates have been limited [94]. Furthermore, a variety of conducted materials can be applied including metals, metal-alloys, conductive polymers and even semiconductors [95].

2.2.1 Fundamentals of electrochemical deposition

Electrochemical deposition, also known as electroplating, is an electrochemical process to coat a thin layer of material on to the surface of conductive object by reducing cations of a desired material from an electrolyte via an electrical current [96]. The reaction during the process is shown in Equation 2.1 where M represents the metal and z represents the number of electrons forming the ionic state of metal is M.

$$M^{z+}_{solution} + ze^{-} \rightarrow M_{lattice} \tag{2.1}$$

The electroplating process can be achieved by either (a) an electrodeposition process where an external power supply is used for providing z electrons, or (b) an electroless deposition process where the electron source is obtained by a reducing agent in the solution [97]. For

ECAM techniques, the first approach is generally applied since deposition rates are higher and can be more easily controlled.

Figure 2.8 shows the schematic set up of a traditional electrodeposition system. The work piece to be plated is the cathode, and the anode is made of certain metal to be plated on the work piece. Both cathode and anode are immersed in a chemical solution called AN electrolyte, which contains one or more dissolved metal salts and ions enabling the flow of electricity. The power supply passes a direct current to the anode, allowing for oxidization and reduction of the metal atoms in the solution. At the cathode, the dissolved metal ions are reduced between the solution and the cathode enabling the electroplating onto the cathode. The ions in the electrolyte are thus continuously replenished by the anode, where the ion dissolve rate at anode is equal to the metal plating rate at cathode.

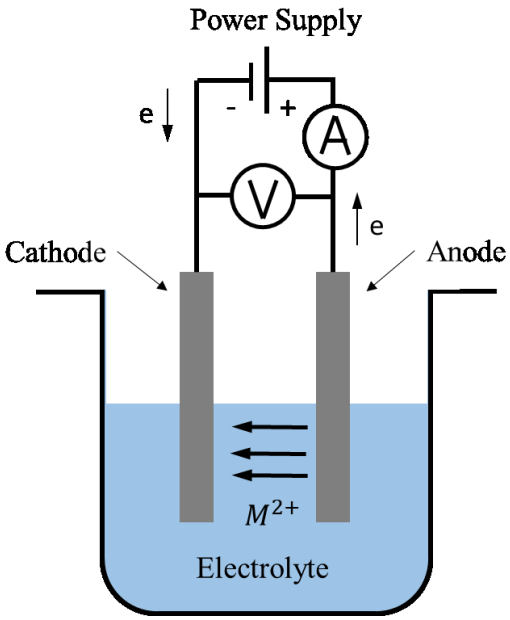

Figure 2.8 Schematic setup of a traditional electrodeposition system.

2.2.2 Mask-based electrochemical additive manufacturing

The mask-based electrochemical additive manufacturing, also known as Electrochemical FABrication (EFAB), was invented by Cohen [98] and it combines electrochemical deposition of metals and photolithography to produce 3D structures ustilizing masks for patterning. It requires to electroplating multi-layers of at least two materials, structural material and sacrificial material, known as 'instant masking', and is followed by a surface planarization process [99]. EFAB can be applied with a wide range of electro-depositable metals. Copper and nickel are the most commonly used sacrificial and structural materials respectively as copper can be much easier removed through chemical etching compared to

nickel. This technique has been commercialized by Microfabrica [98]. The process consists of mainly three steps (Figure 2.9):

- Initially, a sacrificial material (usually copper) is deposited and negatively micro-moulded.
- Then the structural material (usually nickel) is deposited filling the micro-mould on the top of the prefabricated sacrificial material.
- Finally, both materials are planarized to a defined layer-thickness.

The whole process is repeated until the product is completed. And the sacrificial material is removed leaving the structural material with micro-features of about 20 µm with 2 µm resolution and repeatability [100].

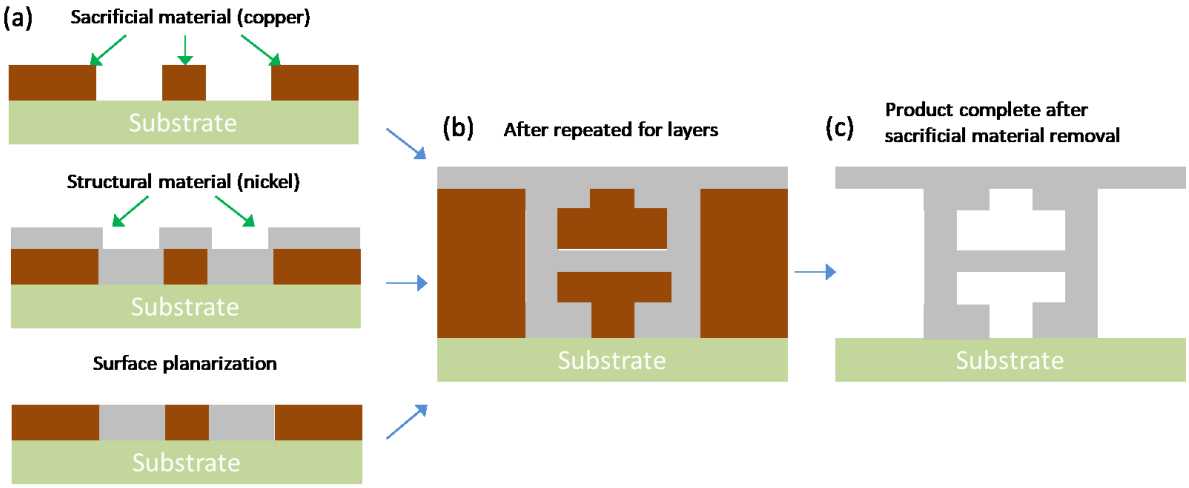

Figure 2.9 Schematic of EFAB fabrication process comprising three steps: (a) depositing sacrificial material; (b) depositing structural material and (c) surface planarization.

The use of sacrificial material allows for fabricating overhang structures enhancing the complexity of the fabricated structures. However, the masks have to be fabricated for each layer depending on the geometries of the layer cross sections and require separate processing time for mask fabrication. In order to precisely control the instant masking process, techniques such as real-time monitoring systems were developed for recording and checking the cell voltage during the electroplating process [101]. EFAB is more suitable for volume production as a large number of custom-designed masks are required to produce for each layer. Recently, to overcome this limitation, a novel system combining a programmable femtosecond light sheet based on DMD and EFAB has been developed, which is called ultrafast laser-enabled 3D metal printing [102] which allows for fast pattern generation in synchronization with laser pulses.

EFAB is suitable for fabrication of robust micro-metal parts with a wide range of applications in industries requiring micron scale components such as: coil structures [103], micro-gears [104], integrated circuits boards [105], invasive surgery tools [106, 107], adaptive optics [108] and microfluidic devices [109]. EFAB is not a fully AM process as it requires masks, a planarization process, and is not fully software-reconfigurable. Also the internal channels are difficult to remove with release holes have to be considered for the design. The efficiency is low and cost is high due to the requirements of design and fabrication of masks for each product.

Considering the limitations of mask-based electrochemical deposition, especially in the context of less control of mass transfer rates at the deposition substrate, promote the development of mask-less electrochemical deposition methods, which has precise control over the convective and diffusive mass transfer rate via the full software-control of all electrodeposition parameters [110]. The micro-/nano- structures are directly fabricated without using masks allowing for applications including nano-electronic and biotechnology industries. There are mainly two categories of direct writing electrodepositon methods which are probe-based electrochemical deposition consisting of Localized Electrochemical Deposition (LED) and Pulsed Electrochemical Deposition (PED), pipette-based electrochemical depositing consisting normal pipette-based electrochemical deposition method and meniscus confined electrochemical deposition (MCED).

2.2.3 Probe-based electrochemical deposition

Localized electrochemical deposition

LED uses an ultra-sharp electrode submerged in an ionically conductive electrolyte close to a conductive substrate where the deposition occurs. A potential is applied between the tip and the substrate, which results in a localized deposition [111]. The selection of the electrolyte is determined by the metal which is desired for the final product. The setup of LED (Figure 2.10) includes a three axis moving stage with an electrolyte tank on the top, a substrate for material deposition as the cathode of the circuit, the metal to be deposited as the anode electrode and a power supply directly connected to the anode and cathode. At the anode, the metal atoms comprised in the metal are reduced into metal ions which diffuse in the solution. The metal ions in the electrolyte are deposited between the solution and the cathode, with factors including electrochemical reactions kinetics, and ion transport via diffusion, convention and electromigration playing a key role [112]. This is also described as an atom-by-atom process providing a complete control over deposition process [113].

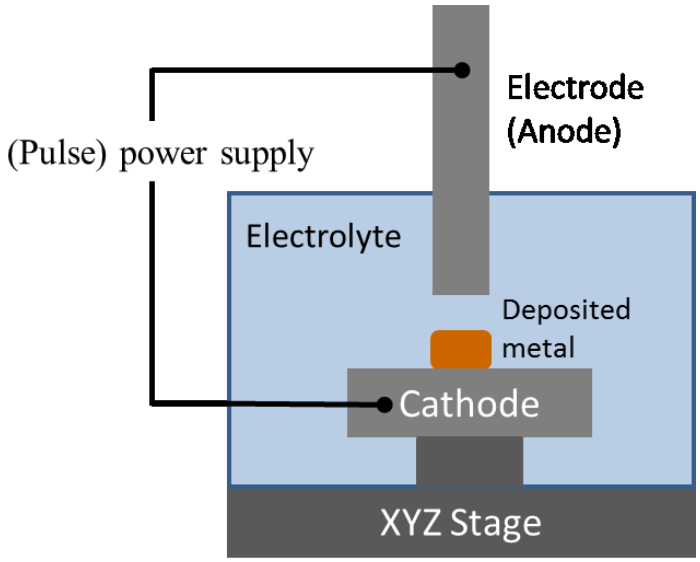

Figure 2.10 Schematic of Localized Electrochemical Deposition (LED) and Pulsed Electrochemical Deposition (PED) with normal and pulse power supplies respectively.

The effects of processing parameters include applied potential, inter-electrode gap and electrolyte concentration on fabricated structures have been investigated. The potential is applied between the electrodes to drive the deposition process, which has a threshold value which is defined by the thermodynamics of the process. In aqueous based electrodeposition processes if the applied voltage is above the a certain limit, bubbles of hydrogen and oxygen are generated, resulting in poor porous structure formation [114]. The criticality of the interelectrode gap for the LED technique was highlighted in the numerical study by Kamaraj *et al.* [94] and Müller *et al.* [115] which discusses the effects of inter-electrode gap on the diffusion controlled deposition and electric field migration. They found that inconsistent deposition could be localized if the gap is too small. However, Seol *et al.* [116] found that the inter-electrode gap also influences the accuracy of the deposited dimension, with no significant effect on the quality of deposited structures. Also, too small the inter-electrode gap (less than the threshold value) results in the electro tunnelling behaviour, which means that the electrons are not available to initiate the ions deposition [117]. In order to control the lateral resolution of the process and the porosity of deposited structures, they proposed the use of in operando X-ray microradiography which could be used to retract the electrode at a suitable speed to maintain a certain interelectrode gap. By using this approach they found a critical range of inter-electrode distance in which the deposition is dominated by migration resulting in a porous structure. However, this approach is not practical due to the need for in operando X-ray radiography monitoring. In addition, The electrolyte concentration was reported to have little impact on the process [118], while another study reported that lower electrolyte concentration negatively affects the quality of the deposited structure since the quasi-static concentration gradients will be different [116]. A strategy was proposed by Said

[113] that the deposition current are monitored during the process to avoid short-circuiting. Here, they were using a platinum wire partially encased in glass as their electrode with the addition of laser based solution jetting to promote mass transport, and managed to increase the LED deposition rates of up to 10 μm·s^{-1} for a 50 μm gold deposition (19, 634 μm^3·s^{-1}) [119]. Yeo *et al*. [120, 121] improved the deposition morphology and deposition speeds via a rotating electrode and investigated the use of ultrasonic vibration with the LED technique and showed that concentricity of the printed wires improved but at the cost of increased porosity.

LED is an inexpensive, free-form and well controlled process for metal AM. The process repeatability, automation, integration and structures printed by LED have been investigated and emphasized by Said [113]. LED has been applied mainly to fabricate structures in the range of micro and submicron scale, while still limited in the fabrication of simple structures, such as tube structures [113], metal lines [120] and helix structures [111], hardly achieving the fabrication of complex 3D structures derived from CAD models [93].

Pulsed electrochemical deposition

PED, based on the LED process, modifies the power supply into pulse power supply by swiftly alternating the potential or current to generate pulses of equal amplitude, polarity and duration. The setup of PED (Figure 2.10) is similar to LED where only the power supply is changed to pulse power supply. PED is a step forward to LED that better-controls deposits with smooth surface can be obtained as the beneficial highly asymmetrical electric field is enhanced in PED [122].

In this case, the factors that define the quality of prints in PED consist of peak current/potential, duty cycle, frequency and effective current/potential. A high peak current/potential is essential to provide ensure fast deposition. Duty cycle and frequency are related to the pulse period, and it is found that lower duty cycles results in a better surface finish as the replenishment of the ions is enhanced due equalisation of concentration gradients during the off time [123]. Lin *et al.* [122] investigated the influence of potential and duty cycles on the structure and surface morphologies of microscale copper columns finding that a short duty cycle (0.1) combined with low potential (2.8 V) benefits dense structure and good surface finish of finer grains and less surface cracks compared with a comparatively higher voltage (3.2 V) and lager duty cycles (0.5) due to the change of surface morphology from a nodular to an acicular structure [124]. Free hanging nickel structures with feature size down to 100 μm as well as freeform shapes with multiple layers were achieved from CAD models [125]. Moreover, it is found that the composition and thickness

of the deposition are dependent on the pulse amplitude and width [126]. The main drawback of PED is that the deposition rates can be slower and the electronics are more complicated. The potential applications of PED involve micro-implants of biomedical field, electronics and microgears of mechanical industry.

The traditional probe-based electrochemical deposition has shown great potential as a fast and inexpensive way to fabricate porous 3D microstructures of various shapes applied with a wide range of conductive and semi-conductive materials. However, due to the limitations in fabricating the sharp conductive probe and confining the electric field down to nanoscale dimension [15], the feature sizes and resolution are limited in the tens of micrometres [113].

2.2.4 Pipette-based electrochemical deposition

Normal pipette-based electrochemical deposition

Based on the limitations of probe-based electrochemical deposition method, Suryavanshi and Yu [15] developed the nanopipette-based probe in a replacement of the traditional sharp conductive probe achieving the external dimeter of the tip down to 200 nm. The setup (Figure 2.11) consists of a quartz pipette filled with electrolyte, an anode electrode inserted into the electrolyte, and a silicon substrate coated with gold film serving as a cathode and also platform for deposition. The pipette is mounted a piezo-driven linear moving system of nanometre resolution. An electric potential is applied between the copper electrode and the substrate. The deposition is initiated by moving the pipette towards the substrate until an electrolyte meniscus is formed between the pipette and substrate. Structures can be deposited by reversely moving the pipette and slowly pulling it away from the substrate at a constant speed with the application of a potential. During the electrodeposition, the contact area on the substrate is determined by the pipette size, thus nano-pipettes achieved very fine resolutions [127].

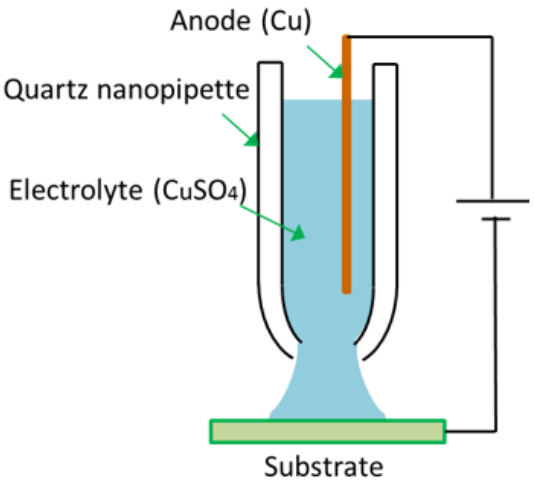

Figure 2.11 Schematic of pipette-based electrochemical deposition.

A uniform and solid nanowire of 200 nm diameter and 10 μm length was demonstrated in [15]. However, the deposited Cu nanowires produced exhibited a polycrystalline nature, which can be overserved from the transmission electron microscopy diffraction patterns. The single crystal formation in the deposits was preferred and the process could be controlled if the kinetics of the initial nuclei growth is faster than the formation of new nuclei. In addition, the clogging of the nozzle occurs, especially at low operating humidity (<30%-35%) since the high evaporation rate results in the crystallization of the copper sulphate closer to the pipette tip. The nucleation of the metal and crystallization of the metal salts on the electrode surfaces were further examined regarding different length scales and time scales in [128]. The deposition potential was limited to avoid the electrolysis of water and thus their deposition rates were relatively slow. An increase in electrolyte concentration was suggested to increase the current density and thus deposition rate; however, this would exasperate the blockage issue.

The pipette-based electrochemical deposition process is similar to extrusion-based AM techniques. The deposition process is reliable and repeatable with a wide range of metal types. However, this approach is limited in fabricating free standing deposits and tube-like structures since the deposition process is constrained from the top onto the substrate in the vertical direction. Fabrication of overhanging or hollow structures remains challenging.

Meniscus confined pipette-based electrochemical deposition

Due to the limitations in the previous techniques, Hu and Yu [129] proposed a meniscus confined electrode (MCE) approach for creating copper wires. A micropipette containing electrolyte with a micro-dispensing nozzle with a diameter ranging from several μm to 100 nm was used as the print head (Figure 2.12). An electrolyte meniscus is established between the nozzle and the substrate, and by applying an appropriate potential, the electrodeposition could be initiated within the meniscus. The maintenance of a stable meniscus has been emphasized requiring the moving speed of the micro-pipette to properly match the growth rate of the local deposits with a high degree of control. With this novel method, the continuous growth of the metals can be in any directions controlled by the programmed tool path achieving full AM.

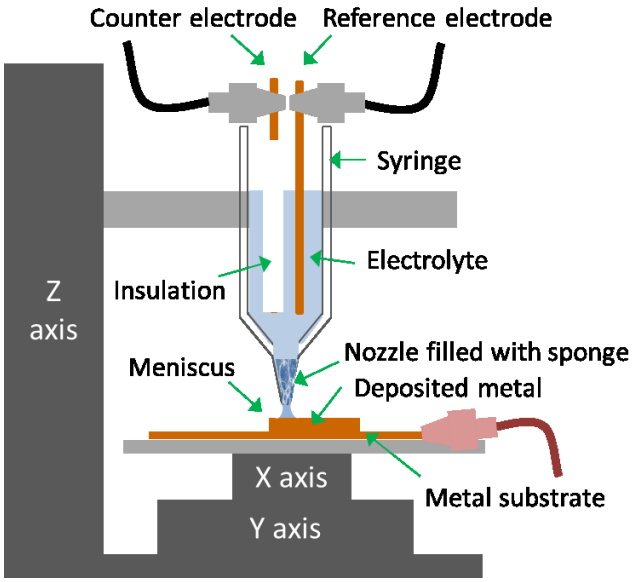

Figure 2.12 Schematic of MCED.

Hu and Yu demonstrated the electrochemical deposition of copper interconnects for circuits at a growth rate of ~0.25 µm/s with a 5 µm sample at a potential of 0.2 V with 0.05 M $CuSO_4$. They showed that the retraction speed could be used to control the thickness of the wire through the narrowing of the meniscus. The pipette size was limited to 1.6 µm in diameter with a retraction speed between 0.3 and 0.6 $\mu m \cdot s^{-1}$, to generate a wire diameter between 800 and 1,600 nm (Maximum deposition rate of 1.2 $\mu m^3 \cdot s^{-1}$). In order to increase the deposition rate and decrease the size of the deposits, they suggested an increase in electrolyte concentration and pipette size. However, this involves challenges in the thermodynamic conditions of the interfacial forces at the three-phase region between the electrolyte, air, and growing wire [129, 130] which could result in an unstable meniscus.

Seol *et al.* [16] developed a simple strategy to improve the previous meniscus guided direct writing approaches by modulating the applied potential with different amplitudes and durations. A hollow microtube was deposited by modulating the pulse potentials (2 V with a duty cycle of 33%, with 0.8 V being applied during the rest cycle). This promoted preferential deposition at the meniscus edge. In order to obtain a solid structure, they added a negative etching step (−0.1 V) with the positive deposition potential (2 V) to suppress preferential deposition at the tip. With this approach, complex 3D metallic microarchitectures were achieved with a diameter of 12 µm equating to a deposition rate of 20.4 $\mu m^3 \cdot s^{-1}$ (0.18 $\mu m \cdot s^{-1}$), with an electrolyte concentration of 1 M and relative humidity of 50%.

Due to the difficulty in maintaining the meniscus on arbitrary positions, Hirt *et al.* [127] used an atomic force microscope (AFM) cantilevers with a nanopipette (FuildFM probe) to

precisely control the deposition of metals voxel-by-voxel (800 nm to more than 5 μm in width) through a pressure-controller. With the AFM cantilever, the growth is detected directly by the force feedback with a LabVIEW routine and thus this achieves an *in situ* precise control. This method allows for metal growth of arbitrary shapes. They have achieved various structures, including hollow vase, triple helix and array of pillars with a deposition speed of ~ 250-500 $nm \cdot s^{-1}$ with a voxel of 250 nm.

2.2.5 Patent review for ECAM based systems

Whilst the ECAM process is a relatively new form of AM, with various research efforts presented on understanding the capabilities of the technique, there is also a number of notable patent disclosures relevant to this work.

Schartz and Whitaker [131], for instance, presented an electrochemical printing system which consists of a print head that expels a small jet of electrolyte towards a conductive substrate. This facilitates the electrodeposition of the material in the printing process. In one embodiment of the invention, multiple electrodes make up the print head, each with their own electrolyte channel. A diagram of this setup is shown in Figure 2.13.

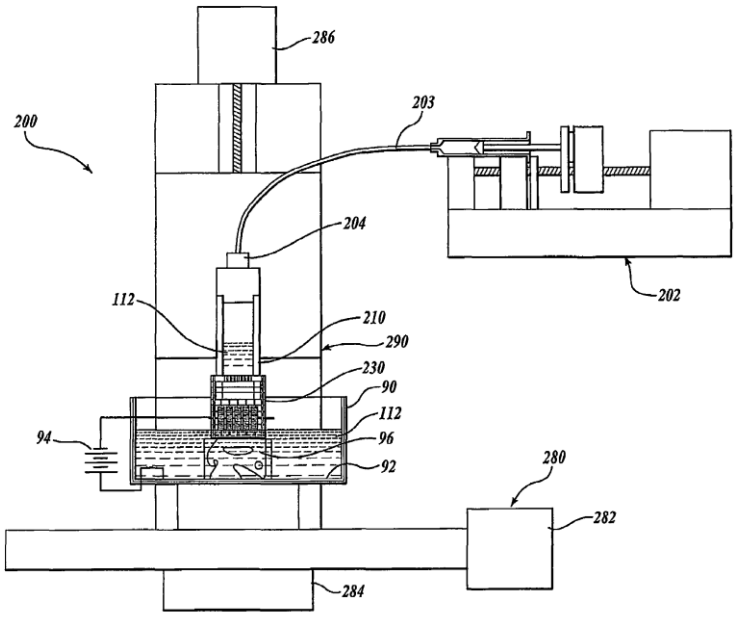

Figure 2.13 The diagram of the setup of an electrochemical printing system proposed by Schartz and Whitaker [131].

Whilst, this electrolyte jetting system is a promising way of reducing mass transport losses this comes with additional hardware complexity which leads to a higher cost system. Hunter *et al.* [132] proposed a solution whereby a fine tipped electrode, which is immersed into a liquid electrolyte, is used to create regions of localised reaction current density leading to

the controlled deposition of material. Here the electrode can be moved around in order to create 3D objects, as well as operated in the reverse direction to etch material away. Here it was highlighted that forced convection of the electrolyte solution could be used. However, whilst mass transport can be improved with this simple design, there is a need for excessive amounts of electrolyte, and also a high sharpness electrode. Furthermore, whilst the fine tipped electrode can create localised currents the resolution of the features will still exhibit a normally distributed morphology, due to the unrestricted electrodeposition. This is diagrammatically shown in Figure 2.14.

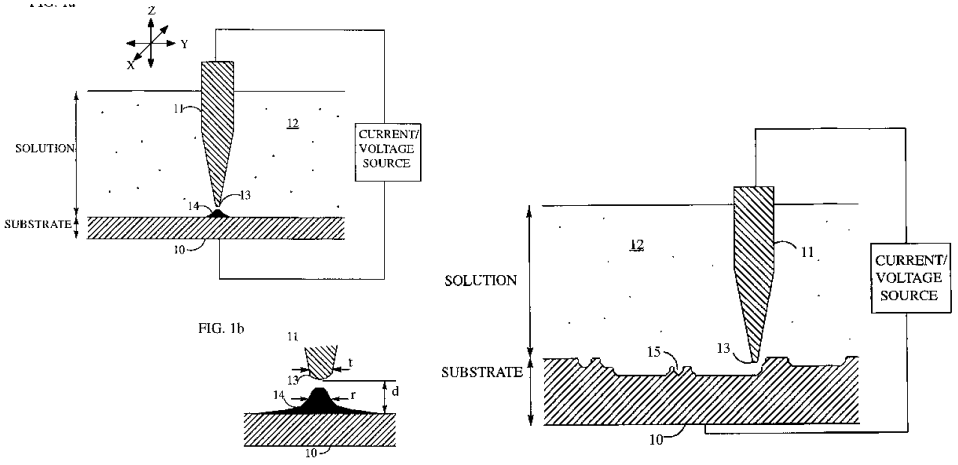

Figure 2.14 The diagram of the setup of an electrolyte jetting system proposed by Hunter *et al*. [132].

In order to improve the complexity of the deposited structures by ECAM, an electrolysis reverse process was developed to remove the electroplating metal deposited onto the surface of a conducting roll [133]. Further development was conducted by Taylor *et al.* [134] to remove metallic structures deposited in acidic electrolyte which contains the metal ions therein is passed between an electrowinning cathode and an anode in a second electrolytic process.

A new branch of ECAM, Stereo Electrochemical Deposition (SED), was developed by Wirth et al., [135] which is able to produce extreme overhang angles layers using a two-dimensional array of anodes to fabricate approaching 90 degrees without the need for a support by inducing an electric field between the anode and the cathode. Furthermore, Sundaram developed a method of electrolytic additive manufacturing process to fabricate metallic micro components layer by layer via localized electrochemical deposition (Figure 2.15). And it allows for the fabrication of powder and powder-less metal parts without thermal damage. Further, the properties of the deposited materials can be modified according to the experimental conditions.

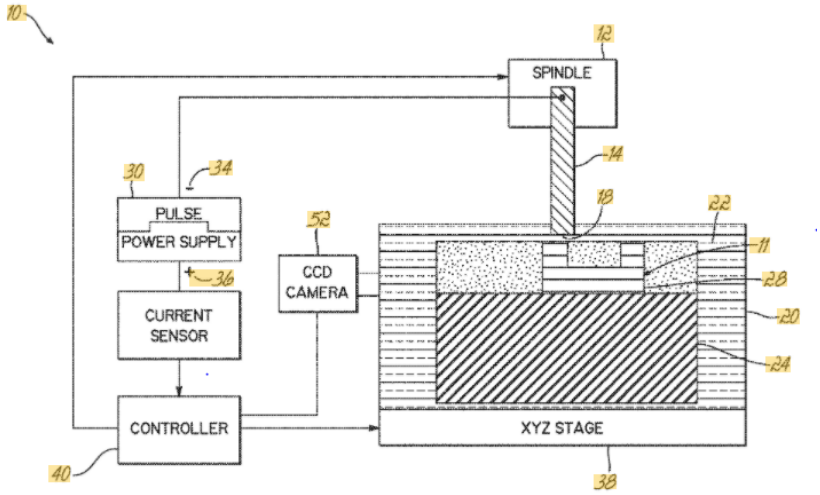

Figure 2.15 Electrolytic additive manufacturing process [136].

2.2.6 Summary of electrochemical additive manufacturing techniques

To date, all of the presented ECAM methods (LCD and MCE) are designed to achieve micro or nanoscale structures using expensive piezo-based movement stages and nano-pipettes. Limited deposition rates for copper-based systems ranging from ~100 $nm \cdot s^{-1}$ to ~0.18 $\mu m \cdot s^{-1}$ (0.008–20.4 $\mu m^3 \cdot s^{-1}$) remains the main barrier to upscaling and competing against conventional 3D printing methods such as DMLS. Furthermore, all the printed structures are limited in the complexity of geometries, with the majority being wire-based architectures with often porous and rough morphologies and limited characterization of the properties of the printed structures. Thus, there is a need to develop larger ECAM systems with improved deposition rates capable of printing more complex structures than linearly extruded microscale objects.

Table 2.3 shows the summary of ECAM techniques in terms of materials, applications, benefit, drawbacks and resolutions.

Table 2.2 Summary of electrochemical additive manufacturing techniques in terms of materials, applications, benefit, drawbacks and resolutions.

ECAM techniques		Materials	Applications	Benefits	Drawbacks	Resolution
Mask-based ECAM		Electro-disposable metals Conductive and semi-conductive materials most commonly: Copper Nickel	Micro-industries Coil structures, microgear, integrated circuits boards, invasive surgery tools, adaptive optics and microfluidic devices	Suitable for volume production	less control of mass transfer rates High cost for a large number of custom-designed masks fabrication Low efficiency	2 μm [101]
Probe-based ECAM	Localized Electrochemical Deposition (LED)		Simple structures such as tube structures, metal lines, and helix structures	Inexpensive, free-form and well controlled process	Not able to produce complex structures	Micron and submicron [113]
	Pulsed Electrochemical Deposition (PED)		Micro-implants of biomedical field electronics and microgears of mechanical industry.	Good surface finish Overhanging structures and multi-layer structures can be fabricated	Reverse electrodeposition involved in the process Contamination of the anode Resolution limited by the electrode size	10-100 μm [124]
Pipette-based ECAM	Normal pipette-based ECAM		Free standing deposits and tube-like structures	Fine resolution Reliable and repeatable	Blockage of the nozzle cannot be avoided	Down to 100 nm [15]
	Meniscus-confined Electrochemical Deposition		Complex 3D microstructures hollow microtube hollow vase triple helix and array of pillars	Fine resolution Able to print complex structures	Difficult to maintain the meniscus	Down to 100 nm [129]

2.3 Electrochemistry theory in meniscus-confined electrodeposition

The meniscus-confined electrochemical deposition technique is the most advanced technique among all ECAM techniques, which has drawn the fabrication resolution down to nano- scale and improved the fabrication ability with more complex architectures [129]. The fundamental electrochemical theory and mechanism in the meniscus-confined electrochemical deposition are of importance to understand before applying the techniques. The deposition dynamics to enhance the feasibility of the process include considerations about growth rate, dimensional limitations and structure qualities. The maintenance of the dynamic stability of the meniscus has been investigated to sustain a continuous 1-D wire growth in a stability region [137].

2.3.1 Basic electrochemical principles

In ECAM, the idea for producing metallic structures is to reduce metal ions out of the selected electrolyte according to basic electrochemical principles. The deposition process depends on a variety of processing parameters, such as the selection of electrolyte, the type of electrode, the applied potential. A large number of metals can be applied, such as gold, silver, nickel, copper and zinc.

As copper is a vital material in industry, which has been used for electrical connections in circuit boards and integrated circuit chips, this will be the focus of this work. The basic electrochemical reaction for electrodeposition of copper with a typical electrolyte of $CuSO_4$ is shown in Equation 2.2.

$$Cu^{2+}_{solution} + 2e^{-} \rightarrow Cu_{solid} \tag{2.2}$$

The electrodeposition in a meniscus-confined AM process is the same as the traditional electrodeposition, with the only difference being the electrochemical deposition only happening inside a meniscus instead of in an electrolyte bath [15, 129, 138].

Cyclic Voltammetry Profile

The potential used in this work was initially is determined by the cyclic voltammetry (CV) profile [11, 139]. CV is a powerful and popular technique for electrochemical analysis to understand the reduction and oxidation processes of species occurring at electrode-electrolyte interfaces [140]. The electrode potential is changed linearly with time during the cycling phase in CV with a certain ramp rate, with the current being measured. A CV plot is obtained between potential values at a constant sweep rate and shows the current flowing through the electrochemical cell versus the applied potential, and this is cycled at a constant sweep rate between two limits. Figure 2.16a shows a typical CV plot for 1 mM

ferrocene/ferrocenium solution at a scan rate of 100 mV/s, which is often used as a model system. The x-axis represents the applied potential (E) imposed on the system and the y-axis is the response, which is the resulting current (i) passed. A crucial parameter is scan rate which indicates that the potential was changed linearly at the scan rate of 100 mV per second.

Understanding the CV 'Duck' shape curve

The peaks in a CV can be understood with reference to the Nernst Equation (2.3), which is used to describe the equilibrium potential between different species, which in this case is Fc^+ and Fc. The potential of an electrochemical cell (E) to the standard potential of a species (E^0), and the relative activities of the oxidized (Ox) and reduced (Red) analyte at equilibrium are related by the Nernst Equation. In the equation, F is Faraday's constant, R is the universal gas constant, n is the number of electrons and T is the temperature

$$E = E^0 - \frac{RT}{nF} \ln \frac{(\text{Red})}{(\text{Ox})} \tag{2.3}$$

In the case of the one-electron reduction of Fc^+ to Fc, the activities can be replaced with their concentrations in the Nernst Equation, where the standard potential E^0 is replaced with the formal potential $E^{0\prime}$, and n is set equal to 1.

$$E = E^{0\prime} + \frac{RT}{F} \ln \frac{(Fc^+)}{(Fc)} = E^{0\prime} + 2.3026 \frac{RT}{F} \ln \frac{(Fc^+)}{(Fc)} \tag{2.4}$$

The formal potential $E^{0\prime}$ is determined by the experiments and estimated with the experimentally derived $E_{1/2}$ value (Figure 2.16a, average value between points F and C). This equation shows how a system equilibrium potential responds to a change of electrolyte concentration. The Butler-Volmer equation then relates the reaction current density to the over-potential (i.e. difference in the applied potential to the equilibrium potential). Here the exchange current density is a function of the concentration of the oxidant and reductant. This correlation between current density and concentration of reductant/oxidant gives rise to the "duck" curve as species are consumed/generated at the electrode/electrolyte interface.

In Figure 2.16a, when the potential is scanned positively from point A to point D, the Fc around electrode surface is oxidized to Fc^+. The peak anodic current is observed at point C. When the switching potential (D) is reached, the scan direction is reversed to the negative direction. While the concentration of Fc at the electrode surface was decreased, the concentration of Fc^+ at the electrode surface was increased. From point D to point G, Fc^+ is steadily reduced to Fc near the electrode. The current is dictated by the delivery of Fc^+ via diffusion from the electrolyte, and the volume of electrolyte containing the reduced Fc is the diffusion layer, which is increasing through the scan. The diffusion layer slows down the

diffusion of Fc^+ to the electrode resulting in the decrease in the current from point F to point G. Additionally, at points B and E, the concentration of Fc and Fc^+ are equal. This shows an example of the reduction process, which is chemically and electrochemically reversible, the difference between two peaks, called peak-to-peak separation (ΔE_p).

Figure 2.16b shows a CV plot for 5 mM $CuSO_4$ solution with an Ag/AgCl reference electrode obtained from the meniscus-confined electrodeposition process [132]. The cathodic reduction and oxidation peaks can be clearly seen at -0.4 V and 0.03 V, indicating the reactions during the deposition process. Once the deposition potential is above the hydrogen evolution potential, the formation of hydrogen bubble can agitate the meniscus and block stable deposition resulting in the highly porous structures (Figure 2.16b). Information about the onset and peak potentials during the metal deposition process can be retrieved by evaluating the deposition potential for the produced metal parts [138]. The results emphasized the importance of maintain the stability of meniscus using the meniscus-confined approach.

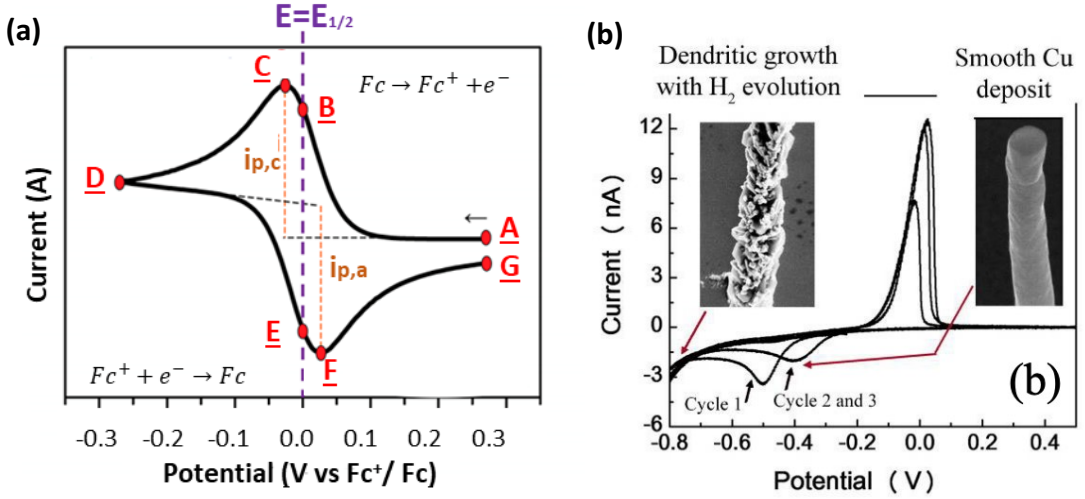

Figure 2.16 (a) a typical voltammogram of the reversible reduction of a 1mM Fc+ solution to Fc at a scan rate of 100 mV/s [140]; (b) the cyclic voltammetry plot in meniscus-confined electrochemical deposition for 5 mM $CuSO_4$ with respect to a Ag/AgCl reference electrode at a scan rate of 100 mV/s [138].

Electrochemical impedance spectroscopy (EIS)

EIS is an electrochemical technique to measure and decouple the frequency dependent impedance of a system. A Nyquist plot is the most popular form of visualising the impedance spectra and is obtained with a potentiostat applying a sinusoidal potential/current to a cell and recording the resulting current/potential profile over a range of frequencies. Three parameters are necessary to define the impedance, the total impedance Z, the phase shift Φ and the frequency. The phase shift is the constant time shift between the two waves. The

total impedance is the ratio of the potential's amplitude and the current's amplitude. The advantage of using EIS is that it can separate the influences of different components, which means the contribution of the charge transfer resistance and double layer capacitance. This technique will be useful later in the thesis when analysing the response of supercapacitors which have been modified with ECAM.

Chronoamperometry (CA)

CA is an electrochemical technique that has been frequently used to study the electrodeposition. Typically, a constant voltage is applied to a cell, while current is recorded as a function of time at the working electrode, relative to the reference electrode. The current behaviour recorded under CA conditions can often reveal a wealth of electrochemical insights such as the columbic efficiency, voltage efficiency, capacitance and the nature of the underlying electrochemical reactions.

Faraday's Law of Electrolysis

The relationship between the electric charge and chemical change in oxidation and reduction reactions is established by Faraday's Law of Electrolysis (2.5), referring that the amount of substance consumed or produced at one of the electrodes in an electrolytic cell is directly proportional to the amount of electricity that passes through the cell.

$$n = \frac{Q}{zF} \tag{2.5}$$

Where n is the number of moles, Q is the total electric charge passed through the substance in coulombs, F is Faraday's constant (F = 96485.33289(59) C mol^{-1}), z is the valence number of ions of the substance. This relationship is important when determining the deposition efficiency, discussed in later chapters.

2.3.2 Meniscus stability

A meniscus is formed in the moving liquid-gas-solid three-phase contact region between material provider (e.g. nozzle) and substrate. Here the deposition of material is allowed to occur owing to the accessible ionic pathway [13]. The stability of the meniscus is of great importance for sustaining the continuous and uniform growth of structures in the meniscus-confined electrodeposition approach. During the deposition, a digital camera is used to capture the image of the meniscus, where the meniscus shape and geometric properties can be easily extracted from the image (Figure 2.17). The metal growth is localized within the meniscus-confined region during electrodeposition. The meniscus-confined electrochemical 3D printing process combines both the vertical wire direct-writing process, forming a

vertical quasi-static meniscus in the direction parallel with the printing direction, and the horizontal dynamic contact lines perpendicular to the printing direction.

In terms of a quasi-static meniscus, as shown in Figure 2.17a, a pipette filled with $CuSO_4$ liquid electrolyte is used for printing Cu structures. A coordinate system is introduced with the z-axis in the vertical direction and y in the horizontal direction. The growth angle (φ_0) is defined as the angle between the line tangent to the meniscus and the wire axis. The meniscus shape during quasi-stable growth is described in Equation (2.6) [129],

$$h_0(w) = \frac{1}{2} w \cos\varphi_0 \left(\cosh^{-1}\frac{D_0}{w\cos\varphi_0} - \cosh^{-1}\frac{1}{\cos\varphi_0}\right) \quad (2.6)$$

Where w is the diameter of the deposited wire, D_0 is the diameter of the pipette nozzle, φ_0 denotes the growth angle, and h_0 is the meniscus height.

By analyzing the plot generated from Equation (2.6) [129], the maximum height of the meniscus occurs at $h_{0_{max}} = 0.28D_0$. When the meniscus height increases from 0 to $h_{0_{max}}$, the liquid meniscus is stretched, whereas the diameter of the deposited structure reduces from D_0 to the value of $0.5D_0$. When the meniscus is stable, a continuous structure deposition can be sustained. Once the meniscus height is further increased, the meniscus is shifted to be unstable, resulting in the breakage of the liquid meniscus and the deposition stops [141].

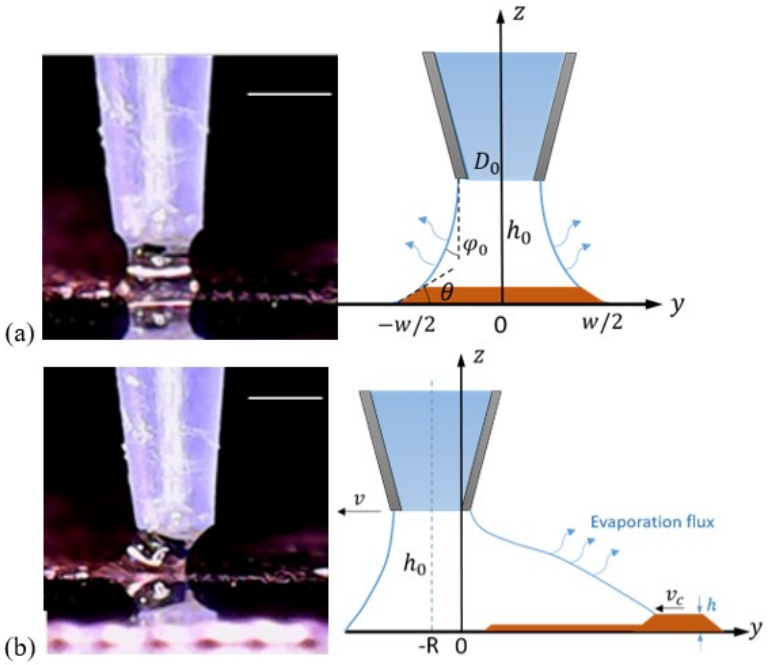

Figure 2.17 (a) quasi-static meniscus (scale bar: 1 mm) and (b) dynamic moving meniscus (scale bar: 1 mm).

When a pipette is moving on the substrate at a constant speed v, the growth in quasi-static meniscus is controlled by the meniscus stability (Figure 2.17a). Furthermore, the dynamic electrodeposition on the copper contact lines is controlled by the balance between the

evaporation flux (mass flux to the right side) and the receding velocity of the contact lines (mass flux to the left side) (Figure 2.17b). The criteria for the stability in terms of optimizing the processing parameters which have been researched and summarized in [142-145].

According to Lei *et al*. [13], the surface morphologies and roughness are mainly governed by evaporation-driven electro-crystallization dynamics near the receding moving contact line. For continuous growth, during the dynamic electrodeposition process (Figure 2.17b), the evaporation induced mass transfer rate must match with the electrodepostion rate v_c to maintain the meniscus stability. And v_c of copper is defined by the Faraday's law [13]:

$$v_c = -\frac{iM_{Cu}}{z_{Cu}\rho_{Cu}F} \tag{2.7}$$

Where i is the electric current density, $z_{Cu}$is the electric charge of the Cu ions, F is the Faraday constant, $M_{Cu}$and ρ_{Cu} are the molar mass and density respectively of the deposited copper line.

Under different scanning speeds, the width, height and surface roughness of copper lines change accordingly with the scanning rate (Figure 2.18). With a scan speed of 0.08 μm/s, a uniform copper line with a relatively smooth surface (12.6 nm Ra) is produced. Here the surface of the copper line becomes rougher with the increase of scan speed. This is due to the enhanced water evaporation and changes in the ion concentration resulting from the increased speed, leading to a coarse surface by the dominant diffusion-controlled electrodeposition.

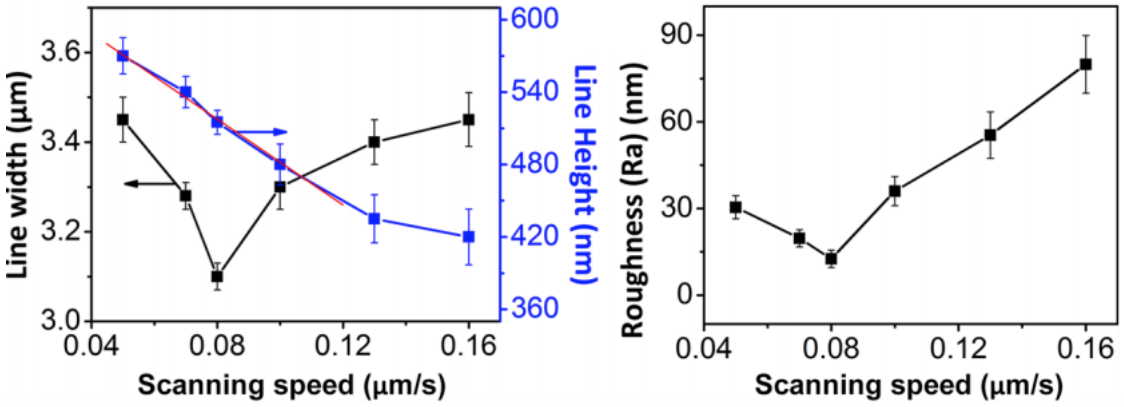

Figure 2.18 The width and height, and roughness vs. scanning speed during dynamic electrodeposition [13].

The results show that the morphology of the printed conductive pattern is related to the scan speeds, controlled by the crystallization dynamics. During the electrodeposition printing, the concentration of the electrolyte at the deposited line changes and the formation of deposits on the substrate is initiated, indicating the growth of the deposition nucleus. The

growth of grains is influenced by the ion concentration distribution and the charge transfer characteristics of the system. Irregular growth is caused by mass-transportation limitations [146]. With slow scanning speeds, copper lines with a smooth surface can be obtained by activation-diffusion-controlled growth. While water evaporation and ions concentration were enhanced with an increase in the scanning speed, leading to a coarser surface of irregular crystal shapes due to diffusion-controlled irregular growth.

2.3.3 Influence of evaporation and humidity control

According to the discussion in Section 2.3.2, the evaporation process is a key factor in controlling the growth rate and geometrical uniformity of the electrochemical deposited structures due to the high surface-to-volume ratio of meniscus at small scale.

During the dynamic deposition, there are two main factors influencing the copper formation:

- Mass flux in the meniscus resulting from the evaporative-induced hydrodynamics at the meniscus surface [147];
- Electrodeposition current at the cathode surface [148-150].

Morsali *et al.* [141] utilized multi-physics finite element simulation, guided by experimental data, to reveal the effect of water evaporation from the liquid meniscus at the tip for deposition in MCED process. Here, key competing factors which influence the total flux of ions include convection, diffusion and migration effects. They used a pipette nozzle of 0.86 μm in diameter. During the evaporation, heat and mass transfer were taken into account. Heat transfer can be expressed in Equation (2.8) [141],

$$\rho C\left(\frac{\partial T}{\partial t}+v\cdot\nabla T\right)-K\nabla^2 T=Q \tag{2.8}$$

Where C is the heat capacity, T is the temperature, K is isotropic thermal conductivity, Q is the heat source, and v is the velocity.

The mass transport is expressed with diffusion equation (2.9) for water vapour concentration within the air domain,

$$\frac{\partial C_v}{\partial t}=D_v\nabla^2 C_v \tag{2.9}$$

Where C_v donates vapour concentration, and D_v is diffusivity of water vapour in air. The local evaporation flux at the meniscus-air interface is expressed in Equation 2.10,

$$J = D\nabla c \tag{2.10}$$

According to the study [141], the average evaporation rate decreases linearly with the relative humidity (RH). At RH=100, the evaporation rate is zero. By lowering the RH, the flux of ions toward the cathode increased, due to the increased evaporation rate from the meniscus surface. In addition, the concentration of the ions at the cathode surface was influenced by the convective flow generated during the evaporation process, controlling the growth rate of the microwire. And the impact of the RH increases with the increase of the nozzle diameter. In addition, the concentration of ions within meniscus increases as the nozzle speed (v_N) increases (Figure 2.19). This is due to the fact that at higher v_N, the radius of the deposited wire decreases because of the stretched meniscus, resulting in the reduced ions at the wire growth front.

Also, it is to be noted that, the clogging of the pipette is mainly due to the evaporation of electrolyte near the tip, which tends to form crystallites on the tip, and will terminate the deposition process [137]. The humidity control is important to the deposition process. In my research, some of the single dots and single line experiments were conducted from April 2015 to July 2016. Table 2.3 shows the average humidity in London during this period is 62%. This is slightly higher than the suggested optimal humidity level of 50% [138]. However, there was no obvious clogging of pipette in my experiment which is likely because the pipette diameter used in my experiment (400 μm) is one order magnitude larger than the micropipette (10 - 40 μm) used in the study of R. Tishkova *et al*. [138]. In addition, a higher RH leads to a lower evaporation rate according to the work of Morsali *et al.* [141]. That leads to a lower mass flux towards cathode electrode. As a result, the mass transfer rate of copper ions at high RH is lower than that at low RH. This thus limits the maximum electrochemical deposition rate as it is linearly proportion to the mass transfer rate from the study of Lei *et al*. [13]. Therefore, a better control over RH can improve ECAM in electrochemical deposition rate and quality.

Table 2.3 London average relative humidity [151]

Category	Least humid	Most Humid	Average Humid
Month	May 2016	Dec 2015	April 2015 - July 2016
RH (%)	50	73	62

2.3.4 Influences of substrate properties

The properties of the substrates have been reported to have an influence on the quality of electrochemical deposited material. The effect of substrate composition on the mechanical properties of electrochemical deposition was investigated by Cakmak *et al.* [152] through scratch tests. Their results show that the electrodeposited materials have better morphological performance, electrochemical corrosion and mechanical properties when deposited on AZ series (Mg-AL-Zn) alloys than AM (Mg-Al-Mn) series alloys. The differences are also attributed to the hardness differences between AZ and AM series alloys, where AZ is lower than AM. In addition, the substrate microstructure have been reported to have a strong effect on the early stage of crystal growth, which is known as α-phase, in the deposited material [153].

2.3.5 Summary of theories and key features in MCED

The maintenance of meniscus stability and the effect of evaporation are both of great importance to minimize the problems involved in the meniscus-confined electrochemical deposition process and assure the quality of printed structures. However, previous research [13, 129] has investigated mainly micropipette electrodeposition and micro-/nano- scale fabrication. There are no researches related to the macro-scale electrochemical deposition and the associated influencing parameters. Research efforts are on their way to find out the similarities and differences between micro-/nano- scale and macro scale meniscus-confined electrochemical deposition processes in terms of effects of processing parameters and maintenance of the printing quality in the process.

The previous literature reviews are focused on all types of AM techniques, especially on the ECAM technique that will be applied in this research. Another actively researched area lies in the AM of smart materials and structures, which have the ability to change the shape and properties as a response to the external stimuli, giving rise to a new term called ‘4D printing’. It is of interest to apply the ECAM technique into 4D printing for smart metal parts fabrication, and the reviews of 4D AM printing techniques are provided as in Section 2.4.

2.4 4D additive manufacturing

AM techniques have been widely applied in various fields, such as fashion industries, biomedical engineering, supercapacitors, sensors, and mechanical metameterieals etc. due to the high design flexibility and ability to fabricate complex structures (Section 2.1 and 2.2). Smart material, which have been utilized for shape recovery, sensors and actuators, have the unique properties to response to external stimuli [154, 155]. By adding smart materials into

the AM process, 3D printed structures therefore can be activated with external stimuli, which were named '4D printed objects' involving time as the fourth dimension [156]. 4D printing can be categorized according to the types of environmental stimuli such as temperature, humidity, solvents, pH or light [157-164]. The induced shape variations can be expansion, shrinkage or folding of the printed objects.

2.4.1 Transformation with thermal stimuli

A common method of creating 4D structures is to synthesize active materials with temperature-responsive properties and to control the thermal boundary conditions to achieve different temporary shapes. Ge *et al.* [165] for instance, proposed a method of adding shape memory polymer (SMP) fibres into an elastomeric matrix to fabricate a hinge. By utilizing the thermal responsive properties of SMPs and the different glass transition temperatures of the materials, the hinge bent with a maximum deformation angle of ~20° and deformation length of 10 mm. Wu *et al.* [166] and Yu *et al.* [167] then progressed this concept by adding different types of SMP fibres with different glass transition temperatures. With this modification, the printed hinges exhibited more varied movements however the maximum operating temperature was limited by the thermal stability of the polymers used, with this often below 100 °C due to the use of a water bath to control the environmental temperature. And the permanent shape can only be recovered with the temperature above the glass transition temperatures of all types of SMP fibres.

These examples, however, only demonstrate limited motions and at modest operational temperatures. To improve this, Zhang *et al.* [168] fabricated a six-petal leaf with a bilayer structure (polylatic acid on paper). By changing the external temperature, the bilayer could uniformly curl into a flower shape. This technique is able to create different kinds of complex structures such as helical structures and corrugated structures. However, the bilayer is fragile with delamination possible after repeated thermal cycles. Printed object composed of seven thermal response SMPs with difference glass transition temperatures (ranging from ~32 ºC to ~65 ºC) was fabricated by Mao *et al.* [169] More complex motion and sequential shape recovery motion was achieved by immersing the printed structure in 100 ºC hot water.

Apart from SMP fibre composite structures, Bakarich *et al.* [170] fabricated a 4D valve with hydrogels. Due to the temperature-sensitive properties of their developed hydrogel, the designed valve was able to control the environmental temperature (20 °C- 60 °C) of the working fluid through moderating the flow rate. The smart valve achieves length changes of 41-49% at 60 ºC. However, thermal stability beyond this range remains a challenge.

Functional components, such as actuating units in planar and tubular shapes were fabricated by Bodaghi *et al.* [161] using different SMP fibres in a flexible beam, allowing for both self-expansion and self-shrinkage during the printing process. A multi-material gripper was fabricated with photo-curable polymers with various cross-linkers monomers with the ability of deformation in high-resolution of a few microns.

2.4.2 Transformation with humidity stimuli

Another approach to 4D printing is to use humidity-responsive materials to actuate the transformation upon absorbing or releasing moisture [171, 172]. Raviv *et al.* [159] printed objects with a rigid plastic base and humidity-responsive materials which expand upon moisture changes. The volume of printed object is able to extend and fold by as much as 200% relative to the original size. However, this expansion is fragile, with the repeatability and reversibility of the folding and unfolding motion limited when more cycles are applied. Zhang *et al.* [172] also fabricated composite films which are able to quickly transform in response to humidity changes. Moreover, shape changes such as bending, helical twisting and rolling can be driven not only by changes in humidity but also by ultraviolet light due to the photomechanical response of the material.

2.4.3 Transformation with current stimuli

Besides temperature-actuated and humidity-actuated materials, current-actuated materials have also been explored as potential materials for 4D printing. Okuzaki *et al.* [173] fabricated a bent accordion-like object by using a conductive polymer combination of polyaniline and polypyrrole (PPy). After applying an electric potential, the shape transformed due to the water vapour in the PPy evaporating due to Joule heating. However, the reversibility of this movement is slow due to the sluggish rehydration of the polymer. Another strategy for the fabrication of electrically responsive materials includes adding conductive media into SMPs. For instance, Lu *et al.* [174] combined carbon nanotubes with a shape-memory polymer. When applying an electrical current the film quickly folded from a flat shape to ‘U’-like temporary shape with the original shape recovered within 120 s. Some other active materials, such as magnetic-responsive materials [175, 176], light-responsive materials [177, 178], and pH-responsive material [179] have also been explored as materials for 4D printing.

2.4.4 Summary of 4D printing

In summary, there is an increased interest in 4D printing to create passive structures that respond to stimuli such as temperature, humidity and current flow. In the majority of these cases, these are composite polymer based materials which allows for ease of fabrication but limits their maximum operating temperature and transient performance due to poor thermal

stability and conductivity. In some cases, the printed objects also exhibit anisotropic mechanical properties due to the poor inter-layer adhesion [180] and some of the constructs also have poor durability due to the mechanical degradation during thermo-mechanical cycling [181]. Metals have a much higher melting temperature than polymers and thus there is potential in creating 4D structures with high operating temperatures and mechanical robustness. However, creating a low-cost multi-material metal printer has not been achieved to-date.

The previous reviewed 3D and 4D printing techniques have a revolutionary role in a wide range of applications. As an emerging advanced fabrication technology, it has drawn increasing interest in the field of electrochemical energy storage due to the advantages including high control of the structure design and the freeform construction. Section 2.6 will focus on the review of AM fabricated electrochemical energy storage devices.

2.5 Application of additive manufacturing in electrochemical energy storage devices

Electrochemical energy storage devices (EESDs), such as rechargeable batteries and electrochemical capacitors, are the most promising energy storage systems due to the high energy and power densities, reliability, cost-efficiency and pollution free operation [182-184]. The fabrication of EESDs involves three key elements, which are electrode fabrication, electrolyte addition and device assembly [185-187]. In recent years, AM technologies have drawn growing interest in the fields of EESDs because of its unique advantages:

- Freeform production and controllable prototyping of customized structures applied for electrodes [188];
- Ability to directly write specific architectures of controlled shapes, interconnectivity and materials [189];
- Allow for optimized thickness (from hundreds of nm to mm) to enhance the areal capacitance [190];
- Enable the integration of EESDs and external electronics so that the post assembly process can be neglected [190].

Electrochemical capacitors are classified in two main categories, sandwich-type and in-plane-type, according to the geometries of EESDs [191-194] (Figure 2.20). The sandwich type contains substrate, two current collectors, symmetrical/asymmetrical electrodes and one electrolyte/separator, stacked layer-by-layer to form a complete electrochemical cell (Figure 2.20a). The other type is in-plane type which includes parallel electrodes patterning on the top of the substrate in the same plane (Figure 2.20b).

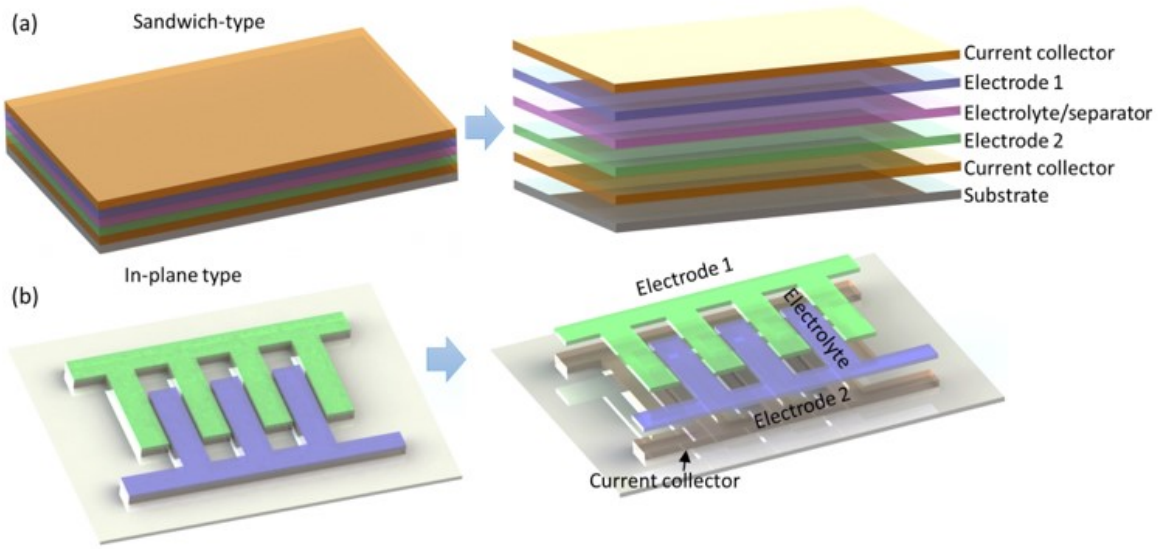

Figure 2.19 Schematic images of (a) sandwich-type and (b) in-plane type EESDs.

2.5.1 Sandwich-type configurations

For the sandwich-type batteries, AM techniques benefit printing customized arbitrary shapes. FDM has been used to print six cylindrical battery integration where the unusual 'U' shape electrodes were fabricated and applied in the sandwich–type batteries [195]. Extrusion-based AM techniques with pneumatic-assisted dispensing heads (inner diameter of nozzle tip = 330 µm) have also been used to fabricate Zn-MnO_2 micro-batteries achieving a capacity of 0.98 $mA \cdot h \cdot cm^{-2}$ over more than 70 cycles. Hu *et al.* [196] used the extrusion-based technique to print cathodes for the lithium-ion batteries. They found that the processing parameters, such as the moving speed of the print head, dispensing pressure, nozzle diameter, and a distance between the nozzle and substrate have effects on the morphology of the printed cathodes. Also, the discharge capacity of 3D printed cathodes is much higher than that of the conventional cathodes at a range of charge-discharge rates.

It has been noted that the surface area, pore distribution, architecture and electrical conductivity are the vital impact factors for the electrochemical performance of the sandwich-type capacitors [197-200]. Zhu *et al.* [201] used a micronozzle to print scaffold-like high porosity structures, known as 3D-graphene composte aerogels (3D-GCA), using mixed materials of graphene oxides (GOs), graphene nanoplatelets (GNP) and silica fillers based on the extrusion-based AM processes. The results show that the gravimetric capacitance achieved at the maximum value of 4.76 $F \cdot g^{-1}$, and the current density of 0.4 $A \cdot g^{-1}$, which are much higher than the other reported devices [201]. Another AM technique, Selective Laser Melting (SLM), has been applied to fabricate helical-shaped steel electrodes of difference sizes, which have the equivalent metal conductivity as normal steel electrodes but of more flexible shapes [202]. After coating with IrO_2, the helical-shaped electrodes

presented excellent capacitive properties, good catalytic and sensing properties. In the sandwich-shape capacitor, the morphology and properties of current collectors are also critical in the electrochemical performance of EESDs. The SLM technique has also been used by Liu *et al.* [203] to print stainless steel scaffolds as the substrate, so that the electroactive surface area can be controlled by changing the laser power and laser scanning speed . Co-electrodepsosition was then processed with the combination of MnO_x-poly (3,4-ethylenedioxythiophene): polystyrene sulfonate (PEDOT:PSS) film. The reaction efficiency was reported to be enhanced with a high areal capacitance and long cycling capability compared to conventional dense substrate.

2.5.2 In-plane type configurations

For in-plane batteries and capacitors, the architectures are of increasing importance to achieve high compatibility with miniaturized electronic devices [204, 205]. A Li-ion microbattery has been designed and fabricated by Sun *et al.* [206] by using inkjet printing on a sub-millimetre scale. The printed electrodes show the high-aspect-ratio and multi-layer structure. The electrochemical test results show an areal capacity of ~1.5 $mA \cdot h \cdot cm^{-2}$, discharge rate below 5 C, and capacity decay from 30 cycle. This type of microbattery was then modifies by Fu *et al*. [207] by including GO in the inks to produce multi-layer GO-based structures, which enables good contact, electrical conductivity and mechanical stiffness of printed electrodes. The discharge capacities were reported to be $91 mA \cdot h \cdot g^{-1}$ with high cycling stability.

AM techniques have also been applied to produce in-plane electrochemical capacitors, which feature high power density and superior cycling stability [208-210]. Sun *et al.* [211] produced an in-plane symmetrical micro-supercapacitor with the graphene-based microelectrodes printed by a microextrusion-based system. The electrochemical test results show that the areal capacitance was dependant on the thickness of the deposited layers and was up to 19.8 $mF \cdot cm^{-2}$. Similar microelectrodes were fabricated by Jiang *et al.* [212] to achieve the current density of 8.4 $mA \cdot cm^{-2}$ and areal capacitance of 41.6 $mF \cdot cm^{-2}$.

2.5.3 Electrodeposition-based 3D printing for energy storage devices

Electrodeposition-based additive manufacturing techniques use an applied electric field to create a localised deposition of a desired material from chemical solutions and colloidal suspensions [213]. This allows for accurate control over layer thickness and compositional gradients of materials to the substrate surface [214]. It has been used to create complex 3D electrodes, with recent developments in batteries, supercapacitors and fuel cells [215, 216]. This technique has advantages in terms of the high flexibility in material types. However,

the limitation lies in the geometry of the deposited electrodes. There are two main categories of electrochemically driven deposition: Electrophoretic deposition (EPD) and electrochemical deposition, where within both approaches have also looked into templating approaches to creating more complex geometries.

In the case of EPD, this deposits layers of colloidal particles onto a substrate via an electric field which carries charged particles to the oppositely-charged electrode [213]. EPD has been used to fabricate supercapacitors with the deposition accuracy in several micrometres. For instance, an ultrahigh-power micro supercapacitor was fabricated by depositing onion-like carbon (OLC) particles (Figure 2.21c) on the gold (Au) current collectors using the EPD technique [217]. The microdevice (Figure 2.21a) has two gold current collectors made of 16 interdigital electrodes with thickness of 7 μm (Figure 2.21b). The integration of these nanoparticles of OLC (diameter between 6-7 nm) results in a high surface-to-volume ratio and improved ionic accessibility, all without using binders. The achieved capacitance is four orders of magnitude higher than electrolytic capacitors (1.3 F cm^{-3}, compared to $3x10^{-4}$ F cm^{-3}, at the scan rate of 1 V s^{-1}) and the volumetric energy density is of an order of magnitude higher ($1x10^{-3}$ Wh cm^{-3}, compared to $9x10^{-5}$ Wh cm^{-3}, at the scan rate of 1 V s^{-1}). A variety of materials can be applied using EPD for fabricating supercapacitors, such as graphene quantum dots (GQDs) [218, 219], multi-wall carbon nanotubes (MWNTs) [220], which exhibit small equivalent series resistance with high specific power density. EPD can also be used in combination with inkjet maskless lithograph and CO_2 laser annealing to build interdigitated graphene electrodes with a multidimensional porous surface, improving the effective utilization of the electrochemical surface area [221]. Compared to conventional capacitors, these supercapacitors demonstrate a combination of enhanced capacitance, columbic efficiency and knee frequency.

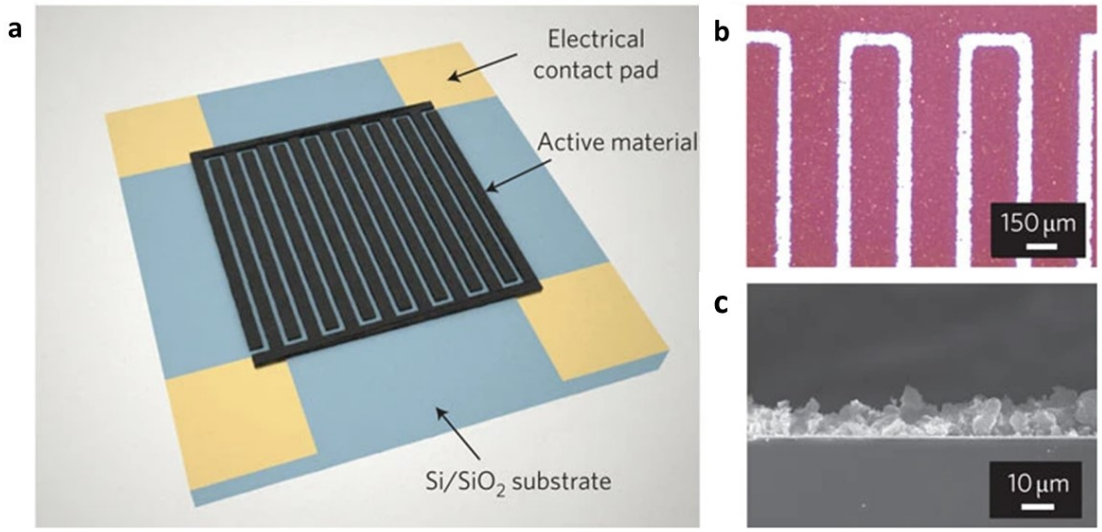

Figure 2.20 (a) schematic of the microdevice (25 mm^2) made of 16 interdigital electrodes with thickness of 7 μm; (b) optical image of the interdigital electrodes with 100 μm spacing; (c) scanning electron microscope image of the cross-section of the carbon onion electrode [217].

In template-assisted electrodeposition, pre-designed templates are used for electrodeposition to print electrodes with complex structures. 3D ultrafast graphene and silicon battery electrodes were fabricated using combined electrodeposition with the traditional templating method [222]. The fabricated electrodes are advantageous in the interconnected structure enabling rapid ion transport, and large electrode surface area. Figure 2.22 shows the Ni inverse opal during stages of the etching, able to fabricate nano-scale features. A similar method was used to fabricate nickel scaffold for the electrodes fabricated by electrodepositing Ni through a polystyrene (PS) opal self-assembled on a glass substrate, and then removing the PS [223]. The obtained electrodes were assembled for an interdigitated 3D lithium ion battery. The independent electrodeposition provides flexibility coating active materials onto the structure and improves power density.

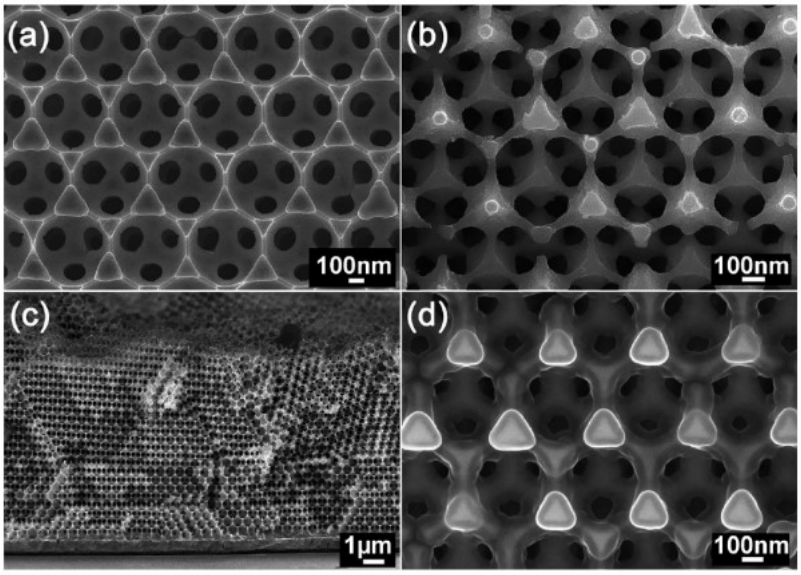

Figure 2.21 SEM images of (a) the Ni inverse opal after template removal, (b) the electropolished Ni reverse opal; (c) the cross-section of the electropolished Ni scaffold; and (d) the structure after Si chemical vaper deposition (CVD) [223].

However, the above-mentioned methods rely on high power and therefore require low resistance, resulting the challenges in reducing the electrode-current collector interfacial resistance. Hence, current collectors based on 3D architectures and nanoscale roughness has been proposed to dramatically increase the electrode-current collector surface contact areas and reduce the interfacial resistance [224]. ECAM can be used to fabricate metallic structures with fine dimensions (from nanometers to tens of micrometers) but has been limited in the complexity of the deposited structures. Large-scale ECAM is advantageous in the depositing speed, but limited in the depositing accuracy (100 μm) compared to the

above-mentioned methods. Compared to other AM techniques applied in electrochemical energy storage, ECAM shows a unique advantage in designing adhered integrated current collectors onto porous electrodes. This opens possibilities in discussing how resistance between electrode and current collector interface affects electrochemical performance of capacitors and how to enhance electronic conductivity of electrode material with metal oxides such as MnO, which have low electronic conductivities. Concurrent to this, ECAM further strengths the performance of energy storage devices in either enlarging electroactive surface area or increasing electronic conductivity of electrode. To date, there has been no research reported on the use of ECAM techniques for energy storage devices, which also indicate the novelty of this research work (Chapter 5). A further literature review about limitations for energy of how does ECAM can further has been discussed in Chapter 5. It is expected that more work will be carried out to apply the electrochemical additive manufacturing techniques for EESDs fabrication to achieve enhanced electrochemical performance.

2.5.4 Summary of AM applications in EESDs fabrication

In this section, we have reviewed the recent progress of additive manufacturing technologies for EES device fabrication. The above examples show that various additive manufacturing techniques have been applied to produce components of EESDs from electrodes to current collectors. The key features of these methods are summarized in Table 2.5. Each type of the discussed additive manufacturing techniques has its strengths and limitations. Materials for laser-based additive manufacturing are restricted to powders with high melting temperature. Stereolithography print 3D constructs by curing of photo-polymer resins layer-by-layer, having the largest flexibility in producing complex architectures. But the materials are limited to photo-curable resins. Electrodeposition-based additive manufacturing deposits either colloidal suspension or chemical solution onto pre-made 3D electrodes. This method has limited control over the size and shape of the printed structures. Using chemical solution reduces the cost compared to colloidal suspension. Extrusion-based 3D printing builds up 3D constructs by extruding ink filaments based on predesigned patterns. It is essential to obtain materials of good printability. The printed customized component structures enhanced the electrochemical performance of EESDs and are promising for producing high-efficient electrochemical energy storage.

Table 2.4 Key features of AM techniques for EESDs fabrication [225].

Categories	AM techniques	resolution	Materials	Print style	Print speed

Laser	Selective laser sintering (SLA)	200-250 µm	Polymer, metal, ceramic powders	Particles fusion	moving : 10 mm/s
Lithography	Projection micro-Stereolithography	<10 µm	UV-curable polymers	Photo-polymerization	moving : 13 µm/s
Electro-deposition	Electrophoretic deposition (EPD) Template-assisted electrodeposition	5 µm	colloidal suspension	Particles conformal coating	thickness: 1.67 µm/s
	Electrochemical deposition	100 nm	chemical solution	Electrochemical coating	moving: 400 µm/s thickness : 2 µm/s
Extrusion-based	Extrusion-based AM technique	20 µm	metal, ceramic, and polymer gels	Filament-based squeezing	moving: 0.1- 150 mm/s

2.6 Summary of literature review and motivation for work

The previous sections have detailed the current state-of–the-art regarding the traditional AM techniques, ECAM techniques, the theory and critical features in meniscus-confined ECAM process, 4D printing and applications of AM techniques in the field of energy storage. The main gaps in the current academic literatures are listed below as motivations for the work in the subsequent chapters.

2.6.1 Traditional additive manufacturing techniques

Traditional AM techniques have benefits in the freedom of design, mass customisation and complex structures fabrication with minimum waste. A comprehensive review of traditional AM methods, materials, fabrication resolution, and the current state in applications was carried out. Of the metal 3D printing techniques, DMLS is widely used and fabricates metal 3D objects on a powder bed. A laser and suitable optics are equipped to locally melt the metal particles, such as titanium, aluminium, and nickel alloys, to fuse the particles together. The main limitation of current DMLS metal AM is the high capital cost in laser optics, high residual stresses in the printed parts and products defects. Due to this, more development is required in the field of metal 3D printing because of its higher cost and lower speed, therefore ECAM is promising for metal parts fabrication WITH low cost.

2.6.2 Electrochemical additive manufacturing fabrication

The current presented ECAM methods (LCD and MCE) are used to fabricate micro- or nanoscale structures, and the resolution is assured with expensive piezo-based movement stages and nano-pipettes/ ultrafine electrodes. Therefore, the deposition speed is limited in

the range of ~100 $nm.s^{-1}$ to ~0.18 $\mu m.s^{-1}$, which is much slower compared to the conventional AM techniques. Moreover, the printed structures are geometrically simple. The architectures are often porous and rough with the limited characterization of the properties of the printed structures. Both LED and MCE electrochemical printing methods are built upon costly piezo-based moving platforms, with low deposition rates (0.008 $\mu m^3.s^{-1}$-20.4 $\mu m^3.s^{-1}$). Thus, there is a need to develop a low-cost electrochemical metal 3D printer with a newly designed print head which is able to print multiple metal materials and functional parts in large scale with improved deposition speed.

2.6.3 Multi–material structure fabrication with ECAM system

The meniscus-confined electrochemical deposition technique has been regarded as the most advanced technique among all ECAM techniques due to the fine fabrication resolution down to nano- scale and improved the fabrication ability with more complex architectures. However, the structures printed are mainly of single-material, and limited application in the connection and bridging of micro circuit boards. Therefore, multi-material multi-layer structures fabrication has not been explored. The characteristics and functionality of the printed hybrid structures will be addressed.

2.6.4 Application of AM techniques in energy storage fabrication

Currently, various AM techniques have been applied to produce components of EESDs from electrodes to current collectors. However, the applied AM techniques are limited in the extrusion-based techniques for polymeric materials, and laser-induced powder-based technique for metallic structures. Since ECAM has presented the potential to fabricate metallic structures of high purity and fine resolution, the application of ECAM in the field of energy storage fabrication is investigated in Chapter 6, of which there are currently no other publications in this area.

Chapter 3 Design and Fabrication of a Low-Cost Desktop Electrochemical 3D Printer

This chapter presents information on the design and fabrication of a low-cost desktop electrochemical 3D printer, where the work has been published in a conference paper: Chen, X, Liu, X, Childs, PRN, Brandon, NP and Wu, B. Design and Fabrication of a low-cost electrochemical 3D printer. *Proceedings of 3rd international Conference on Progress in Additive Manufacturing (Pro-AM),* Edited by C.K., Chua, W.Y., Yeong, M.J., Tan, E., Liu, S.B., Tor, Singapore, 2018. (ISSN: 2424-8967). As the first author of this publication, I led most of the tasks, including design and fabrication of the low-cost desktop electrochemical 3D printer, data collection, data analysis, drafting the article. The co-authors supervised and co-supervised the work, contributing to the critical revision of the article and final approval of the version published.

3.1 Introduction

This chapter presents the low cost electrochemical multi-metal 3D printer which was converted from a commercial fused deposition modelling 3D printer (WER Me Creator) by replacing the heated extrusion head with one or multiple 10 mL polypropylene syringes (Metcal-7100LL1NPK) with 400 μm polypropylene nozzles (Metcal-922125-DHUV), providing the 3D motion control system to maintain the stability during the fabrication process. The print head is replaced with a new meniscus-confined electrochemical deposition system. The initial proposed designs and further improvement for advanced research works are investigated and listed in the chapter as below.

- **Description and comparison of proposed print head designs**

  This section describes and compares three proposed print head designs, the gear-assisted print head, sponge-assisted print head and nanofiber-assisted print head respectively, for the developed system. The content of this chapter corresponds to the optimization

process of the printer design, and the use of sponge-assisted and nanofiber-assisted print heads allowing for higher volumetric deposition rates compared with other electrochemical manufacturing approaches. 2D CAD drawings of fabricated parts for the fixation of the print head are presented in Appendix A

- **System set up for single-material and multi-material fabrication**

  This section outlines the experiment set up and techniques used to optimize the processing parameters for the developed system validation. The influence of deposition potential and concentration are also shown for copper deposition from an aqueous copper sulphate solution. The print unit is further developed from single print head to dual-deposition heads for multi-material structures fabrication The devices selected for the system set up are included in Appendix B. The cost of the whole system is presented in Appendix C.

- **Optimization of processing parameters**

  This section presents the optimization of processing parameters such as deposition potential, deposition current and solution density. The parameters have great impacts on the quality of deposited structures and the optimized set of parameters is important to figure out through a series of experiments.

In order to facilitate the large-scale (macro-) part fabrication using a meniscus electrochemical deposition method, it is important to compare different designs for the deposition print head, and find out the best design to print high-quality structures. Also, the optimization of the processing parameters is of great importance to assure the quality.

3.2 Print head designs and comparison

A print head is an essential part of a 3D printer; fabricating complex 3D geometries through solidification of sequential layers of material [92]. In the FDM printing process, the print head consists of hot end and cold components moving in the x and y directions. The cold components consist of a hollow-lock socket screw, holder and tubing which serves the function of guiding the plastic filament and delivering this through to the hot end. A hot end typically contains a thermistor and an extrusion nozzle, and typically heats thermoplastics such as polylactic acid (PLA) [12] into a plastic state and extrudes this layer by layer to build a 3D object The advantage of this system is the low cost nature of its construction. For localized electrochemical deposition (LED) 3D printing, the print head consists of a sharp-tipped electrode submerged in an electrolyte close to a conductive substrate. Under a positive

potential between anode and cathode, metal ions deposit on the conductive substrate as the metal ions are reduced [111]. Meniscus confined electrochemical (MCE) 3D printing is another approach to build metallic structure through the formation of a stabilized liquid meniscus between dispensing nozzle and conductive substrate. The print head contains electrolyte in a micropipette and dispenses the electrolyte through the nozzle [129]. The challenge in existing ECAM approaches is that fine tipped electrodes are fragile and expensive to make with low volumetric deposition rates. The pipette designs presented so far have limited cross-sectional areas again resulting in low volumetric deposition rates. Thus, new designs are needed for high volumetric deposition rate ECAM systems.

3.2.1 Gear-assisted print head design

In order to control the electrolyte meniscus a gear-assisted print head system was considered. Here. Figure 3.1a shows the detailed design of a rack and pinion gear-assisted print head consisting of a dispensing syringe, a metal piston, a stepper motor and a deposition nozzle. The nozzle diameter has an effect on the deposition rate, according to Morsali *et al.* [141], with the deposition rate increasing when increasing the nozzle diameter. A set of smooth tapered nozzles (Nordson EFD) with different inner diameters ranging from 0.2 mm to 1.6 mm were studied in order to assess suitability for this application. Of these, the 400 µm nozzle diameter was selected as the optimal which maximized the surface area, which allows for large-scale and fast electrochemical deposition, whilst forming a stable meniscus. In contrast, the experimental results indicate that a nozzle diameter larger than 0.4 mm, including a 1.6 mm as shown in the **Figure 3.1** (largest commercially available smooth tapered nozzle from Nordson EFD), is not suitable as the surface tension of the electrolyte is not able to maintain a stable meniscus.

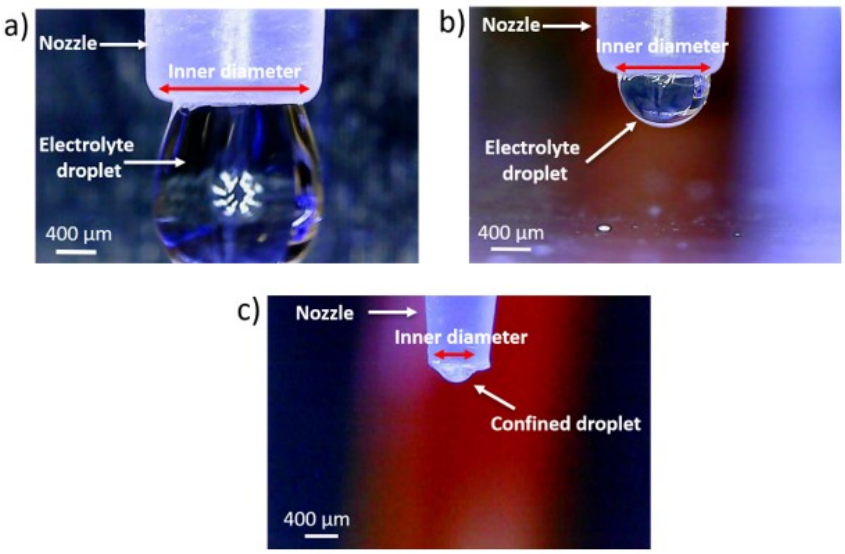

Figure 3.1 a) Detailed optical image of larger smooth tapered nozzle (ID: 1.6 mm) presenting an instable electrolyte droplet. b) Detailed optical image of smooth tapered nozzle (ID: 1 mm) showing an instable electrolyte droplet. c) Detailed image of a confined electrolyte droplet which is able to form a stable meniscus in the electrochemical deposition (ID: 400 μm).

The electrolyte in the syringe is dispensed through a 400 μm diameter plastic nozzle to form a meniscus between nozzle and conductive platform (cathode), which is driven by a stepper motor (Figure 3.2a). The piston connecting to the end of rack gear is submerged in the electrolyte, which works as anode. The print head has three movements, one vertical movement for controlling the position of the gear-assisted extruder in the Z direction, two movements for guiding the print head in direction of x and y.

3.2.2 Sponge-assisted print head design

Figure 3.2b shows a print head with a sponge inserted in the deposition nozzle to balance the hydraulic head exerted by the electrolyte in the syringe. Specifically, the inserted sponge cubes were prepared in dimensions of 20 mm (length) x 10 mm (width) x 10 mm (depth). A plastic syringe and nozzle (diameter 400 μm) with an open pore sponge is filled with copper sulphate solution (Figure 3.2c). Three single sponge cubes were compressed into the nozzle head (Metcal-922125-DHUV). The sponge used in this study is made of polyurethane. The porosity (ϕ) of the uncompressed sponge was measured to be 0.59 (where 1 is complete void and 0 is completely dense). The electrolyte is extruded through nozzle, governed by the formation of a stable meniscus and entrainment from the lateral movement of the print head.

One of the key challenges is to balance the static hydraulic head with the pressure drop through the nozzle and the surface tension effects. A porous sponge is inert to the electrolyte and serves the purpose of providing sufficient back pressure to the hydraulic head such that a stable meniscus can be formed. Without this sponge, the electrolyte readily flows through the large nozzle since the surface tension of the electrolyte cannot maintain the meniscus. The quantitative evaluation of the sponge length can be calculated by considering the static pressure head (Equation 3.1) and Darcy's law (Equation 3.2) which is listed below:

$$p_b - p_a = -\gamma(Z_b - Z_a) \tag{3.1}$$

Where, $p_b - p_a$ is the pressure drop, $Z_b - Z_a$ is the height of the fluid and γ is the specific weight of the electrolyte.

$$Q = \frac{-\kappa A}{\mu}\frac{(p_b - p_a)}{L} \tag{3.2}$$

Where, Q is the total flow rate ($m^3.s^{-1}$), κ is the product of the intrinsic permeability of the medium (m^2), A is the cross-sectional area that the flow experiences (m^2), $p_b - p_a$ is total pressure drop (Pa) and L is the length over which the pressure drop acts (m).

The reference and counter electrodes are inserted into the electrolyte at a fixed distance from each other. To maintain dimensional accuracy, an insulated plastic holder covers the counter electrode. The deposition process is a reduction reaction of Cu^{2+} from the electrolyte. Simultaneously, the copper wire replenishes the Cu^{2+} back to the electrolyte. Thus, a concentration gradient is created between counter and working electrode.

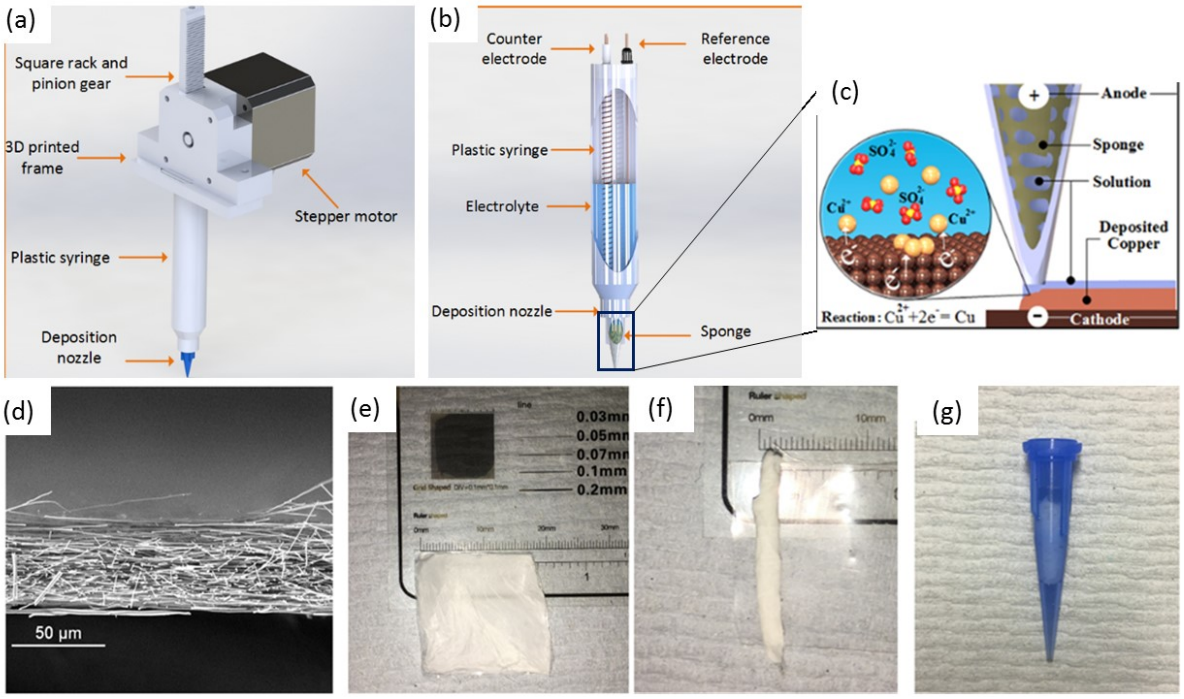

Figure 3.2 (a) Schematic illustration of piston-assisted electrochemical 3D printer [226]; (b) Schematic illustration of sponge-assisted print head [226]; c) Detailed view of the sponge-assited print nozzle filled with filled with copper sulphate solution with the sponge in the tip; d) SEM image of the electrospun nanofibre mat; e) Photo of flat electrospun mat; f) rolled nanofibre and g) nanofibre nib installed into the nozzle.

3.2.3 Nanofibre-assisted print head design

In this approach, nanofibre mats were formed through the electrospinning of polyacrylonitrile (PAN) dissolved in a dimethylformamide (DMF) solvent. Figure 3.2d shows the SEM image of the electrospun nanofibers. Figure 3.2e – Figure 3.2g show the steps to prepare the nanofibre-based nozzle: firstly, the spun mats were cut into 17 mm x 17 mm squares with a measured thickness of 50 µm; and then rolled and placed into a tapered plastic nozzle with an end diameter of 400 µm.

The porosity (ϕ) of nanofibre was controlled at value of 0.24 (1 is for completely void and 0 is for completely dense) by Equation 3.3 and Equation 3.4:

Nanofibre mat (NFM) apparent density (g/cm^3)

$$= \frac{\text{NFM Mass (mg)} \times 10}{\text{NFM thickness (μm)} \times \text{NFM area (cm}^2\text{)}} \tag{3.3}$$

And NFM porosity

$$= \left(1 - \frac{\text{NFM apparent density (g/cm}^3\text{)}}{\text{bulk density of PET (g/cm}^3\text{)}}\right) \tag{3.4}$$

Where the bulk density of PAN nanofibre is 1.3 g/cm^3.

3.2.4 Comparison among the proposed print head designs

Comparing the designs of the piston-assisted print head and material-filled (sponge-assisted and nanofiber-assisted nozzle print heads), the rack and pinion gear-assisted print head was determined to be unfeasible upon testing due to the difficulty in establishing a stable meniscus. It required accurate adaptive control in adjusting the movement of piston to maintain the meniscus shape. This makes the control of deposition process more complex than the other two methods. In addition, the moving piston acts as an anode (counter electrode) that is unable to maintain a constant distance between counter and reference electrode with a further challenge of removing all of the gas bubbles upon insertion of the electrolyte.

For micro-/nano- scale meniscus-confined electrochemical deposition processes, micro-capillary tube have been employed for maintaining a stable meniscus during the deposition process [137]. However, for large-scale meniscus-confined electrochemical deposition, maintaining a stable balance between the hydraulic head of the electrolyte and the back pressure provided by the surface tension of the electrolyte and the nozzle is crucial for forming a stable meniscus. Here we investigate the use of a foam-filled nozzle, which has previously been explored in inkjet printing systems [227], and show advantages in providing sufficient back pressure whilst not introducing excessive additional diffusion resistance. Different foam-like materials can be considered, as long as no chemical reaction with the electrolyte is observed. As polyurethane sponges are the most common and cheap choice, the sponge-filled nozzle was initially used to validate the concept, and it produced stable meniscus, and careful selection of the sponge material to balance the hydraulic head of the electrolyte was needed. To create a stable meniscus, the print head moves to touch the deposition platform and retract slightly. However, it is difficult precisely control the pore

size of the sponge used (due to the varying levels of compression), leading to inconsistent back pressures. Electrospun nanofibers were then explored as an alternative and better choice due to the reproducibility of the fibres, the smaller pore size and the capillary effect resulted from the fibre-based morphology. The nanofiber-filled nozzle is not only able to provide suitable back pressure against the hydraulic head whilst minimising diffusion resistance which thus provides a potential route to increasing the reaction current density.

3.3 System set up for single-material fabrication

Figure 3.3a shows a schematic setup of the developed electrochemical 3D printer. The nozzle/syringe assembly (print head) (Figure 3.3b) is mounted on a carriage that can be moved in the x and y direction, with the stationary platform also able to move in the z direction through the use of computer controlled stepper motors (NEMA17). In Figure 3.3c, two copper rods are suspended in the copper sulphate electrolyte and act as a counter and reference electrode. The counter electrode is held in an insulated holder to maintain dimensional accuracy with the end of the copper rod attached to a copper wire which is wrapped around the insulating holder. The reference electrode is used to correct for polarisation over potentials during the deposition process. A working and sense electrode is connected to a copper substrate plate.

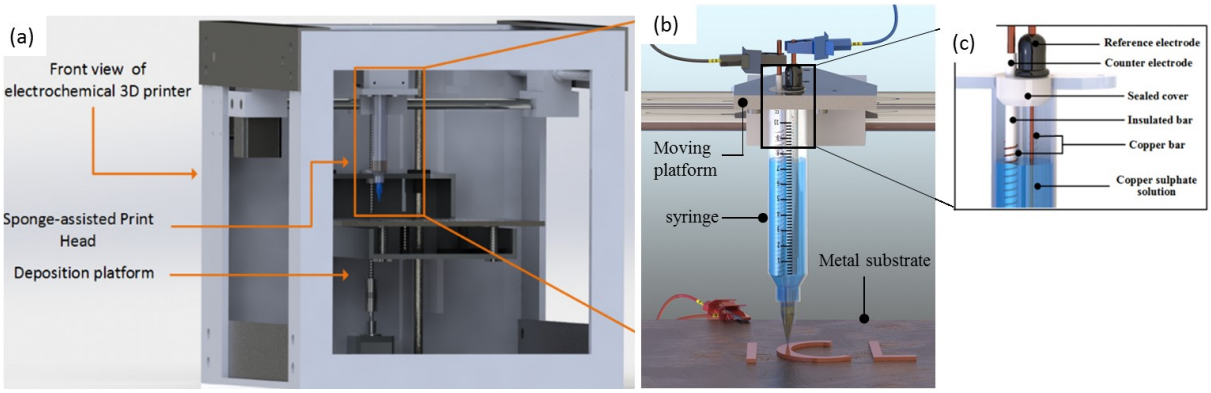

Figure 3.3 (a) Schematic illustration of the electrochemical 3D printer; b) schematic of print head set-up [226]; c) Detail view illustrating electrode arrangement [92].

To create a structure, the print head contacts the copper substrate and retracts a small amount to form a stable meniscus. A positive potential is then applied between the working and counter electrodes to deposit copper onto the substrate through the reduction of Cu^{2+} ions. A constant voltage is applied between the working and counter electrode based on the measurements between the sense and reference electrodes using an Autolab workstation (Metrohm PGSTAT302N). The Cu^{2+} ions are simultaneously replenished from the counter electrode through the accompanying oxidation reaction to form a concentration gradient

controlled through a combination of diffusion and migration. The print head is then moved in the x and y directions as defined by the tool path generated based on the 3D computer model.

3.4 System improvement for multi-material fabrication

Figure 3.4a – Figure 3.4c present the modified rig consists of a stage with two in-line plastic syringes separated by a distance of 80 mm. One syringe contains a copper sulphate electrolyte (blue solution) and one holds a nickel sulphate electrolyte solution (green solution). For the copper sulphate syringe assembly, two copper wires were inserted into the electrolyte, one as a counter electrode and one as a reference electrode. Sense and working electrode probes from a potentiostat are attached to a copper substrate platform where the deposition occurs. The setup for the syringe containing the nickel solution was similar, but the materials serving as the reference and counter electrodes were changed from copper wires to nickel foams. The deposition unit has two movements (x and y axis) and the deposition platform is able to move along z axis. The movements are computer controlled by stepper motors.

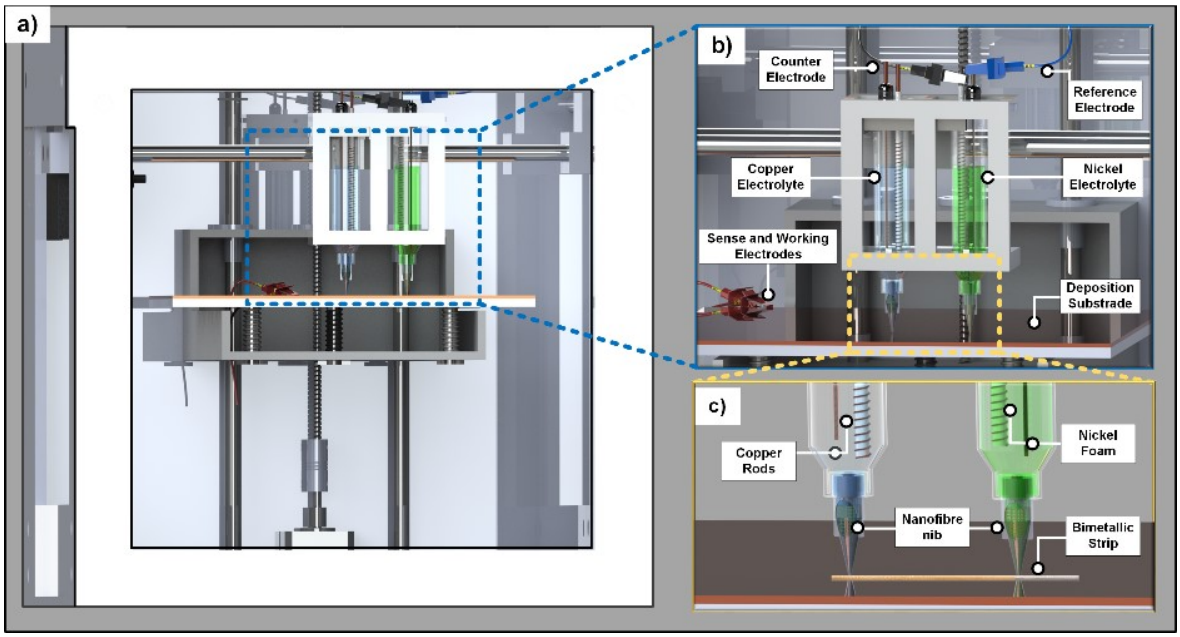

Figure 3.4 Illustration of the low cost electrochemical multi-metal 3D printer. a) Front view. b) Print head setup. c) Detailed view highlighting the deposition nozzles and the deposited bimetallic strip [228].

3.5 System cost

This system is designed for macro-scale fabrication and built up by modifying the print head of a low-cost commercial fused deposition modelling 3D printer (WER Me Creator, £300).

The FDM print head is replaced with a 3D printed holder and 10 mL polypropylene syringe (Metcal-7100LL1NPK) with a 400 μm polypropylene nozzle (Metcal-922125-DHUV). The total cost of the system modification is £564 with a detailed breakdown listed in Appendix C. Whilst a potentiostat was used in this work to control the potential/current applied to the working electrode, this could easily be modified with lower cost power supply due to the low current demand of the unit. However, in the case of this PhD study, the accuracy and controllability of a potentiostat was ideal.

Other ECAM approaches, as reviewed in Section 2.2, are designed to achieve micro- and nano-scale fabrication which requires expensive piezo-based movement stages and nano-pipettes can often be very costly. For example, a commonly used nanopositioning piezo stage (nPoint, NPXY80-2) is £15,000. In terms of DMLS systems, these can cost upward of £150,000 due to the high cost of the laser optics, gas handling system and other supporting systems. With these considerations, the authors believe it is fair to call the proposed system 'low-cost', albeit with the acknowledged compromises in the fine position control.

3.6 Formation of a stable meniscus

The stability of stabilised meniscus is of great importance for the continuity of the printing process and high quality of printed structures. The meniscus has been monitored by a USB digital microscope (Aomekie A01014). The test was carried out for a 400 μm diameter nozzle with a 1 M copper sulphate solution, 6 cm^3 of polyurethane sponge was used.

Figure 3.5 shows the static and dynamic morphology of the meniscus under different conditions to highlight stable and unstable regions of operation. Figure 3.5a shows the image of the nozzle approaching the build plate. Figure 3.5a shows a stable static meniscus with a height of 400 μm ± 10 μm and Figure 3.5b illustrates the same meniscus under a dynamic x-direction translation of 0.4 $mm.s^{-1}$ and deposition potential of 2 V. Above 500 μm it was not possible to form a stable nozzle-substrate meniscus due to the large distance between the nozzle and the substrate. During operation bubble formation across all working potentials did not cause observed stability issues for the meniscus due to the lateral motion of the print head preventing gas accumulation.

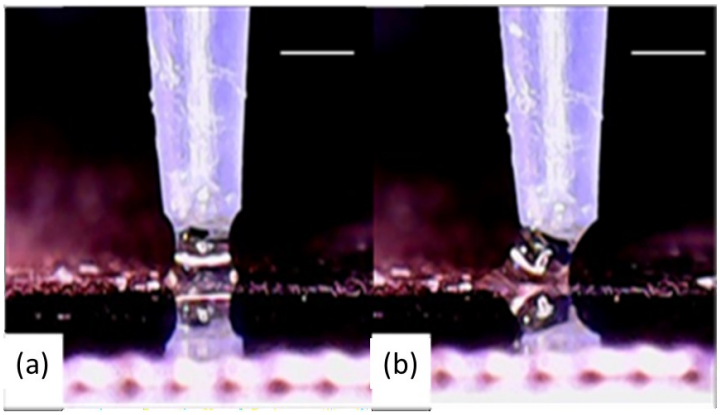

Figure 3.5 a) a stable static meniscus with the diameter of 400 µm and height of 400 µm ± 10 µm. b) the dynamic meniscus generated at a lateral speed of 0.4 mm.s^{-1} and deposition potential of 2 V. The scale bar in image is 400 µm length [92].

It should also be noted that during the printing process, as the aqueous electrolyte is exposed to ambient conditions, there is a degree of evaporation of the water, especially in the meniscus trails. Since a 1M copper sulphate solution is used this results in the formation of salt precipitates on the surface of the printed components. This problem manifests itself in other ECAM systems also, with notable examples being the micro-pipette based ECAM [14] where this can lead to blockages in the nozzle. In the case of this work, since a relatively large 400 µm nozzle is used, blockage issues are less of a problem and salt crystal formation can be addressed with water to wash this away. However, this is a problem as the system is to be scaled, which might be overcome by the use of approaches such as hydrogel-based tips, to minimise the amount of electrolyte evaporation.

3.7 Optimization of process parameters

Electrochemical characterization methods, such as cyclic voltammetry and chronoamperometry, have been used to understand how scan rate, current density and polarization potential affects deposition performance. Concurrent to this, a sponge-assisted print head was used for optimizing the processing parameters. The effect of these parameters is investigated by depositing a plane copper strip from copper sulphate using varying parameters.

3.7.1 Cyclic voltammetry

The cyclic voltammetry investigation of Cu^{2+} in copper sulphate of different molar concentrations (0.05 M, 0.1 M and 0.25 M), was carried out to understand the influence of concentration. Specifically, the electrochemical reduction with varying concentrations from 0.05 M to 0.25 M Cu^{2+} was investigated with a copper reference electrode within the potential range of ±5 V, ±2.5 V, ±2 V, ±1.5 V, ±1 V, ±0.8 V, ±0.6 V, ±0.4 V, ±0.2 V.

A typical half-cell cyclic voltammogram recorded for 0.05 M Cu^{2+} with a scan rate of 50 mV s^{-1} in a scanning window of +0.8 V to -0.8 V is shown in Figure 3.6.

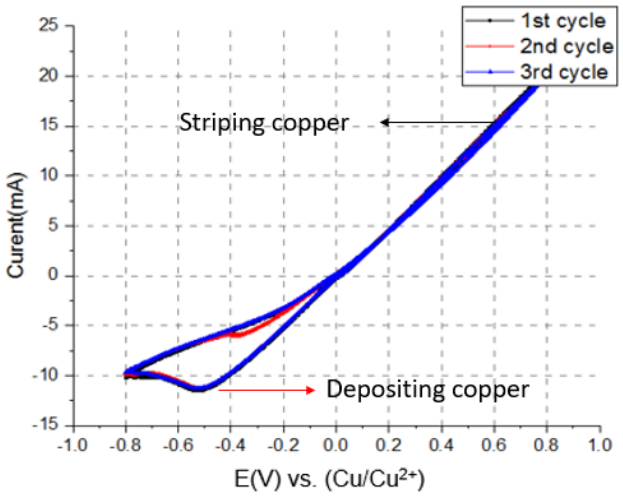

Figure 3.6 Cyclic voltammetry of 0.05 M Cu^{2+} in copper sulphate at 0.8 V with scan rate of 50 mV/s.

From the above CV plot, there are three cycles in total with overlap each other indicating good reversibility. The voltage measured against reference electrode (Cu/Cu^{2+}). Each cycle commenced at 0 V, reversed at +0.8 V, and terminated at 0 V. In a half-cell reaction, there is oxidation along with the forward scan, which strips the working electrodes. Due to "infinite" copper ions supplied from the copper bar, the schematic graph presents as a straight line in forward scan [229]. Furthermore, in reverse scan, cathodic current starts to increase and a cathodic peak i_{pc} at about 0.5V is observed.

In the reduction of Cu^{2+}/Cu, the cathodic peak (i_{pc}) results from the reduction of Cu^{2+} to Cu. For this half-cell reaction, the Nernst equation can be presented as (3.5):

$$E_{cathode} = E^0 + \frac{RT}{nF} \ln[Cu^{2+}] \quad (3.5)$$

Where, E^0 is standard reduction cell potential, n is the number of moles of electrons transferred in the half-reaction, R is gas constant, T is temperature in kelvin. Rearrange the Nernst equation in form of (3.6):

$$E_{cell} = E_{cathode} - E_{anode} = (0.34V - 0.34V) + \frac{RT}{nF} \ln[\frac{0.5\text{M}\ (Cu^{2+})}{0.5M\ (Cu^{2+})}] = 0 \quad (3.6)$$

According to Equation (3.6), the open circuit cell potential is zero. That means the reduction of copper ions cannot actually occur spontaneously and an electrical bias needs to be added. According to the Bulter-Volmer equation, an overpotential (difference between electrode

potential and equilibrium potential) is needed to activate the redox reaction. In this case, the equilibrium potential is zero. Thereby, as long as applying an external potential in system, the redox reaction will occur.

The decaying cathodic current passes the peak i_{pc} because the electrolyte has been depleted in a diffusion layer near the electrode. The mechanism of this phenomenon can be explained by Fick's Law (3.7):

$$\text{Diffusion flux} = -D\times\frac{\Delta C}{\Delta X} = -D\times\frac{C_{surface}-C_{bulk}}{x_{surface}-x_{bulk}} \quad (3.7)$$

In the equation, D refers to the diffusion coefficient, ΔC is the concentration difference, and ΔX is the changing distance of the diffusion layer. As soon as a reduction potential applied, the copper ions are consumed nearby the reduction electrode. That leads to a copper ions diffusion zone ΔX. The concentration difference of Cu^{2+} will change dramatically during the reduction reaction. The current in the deposition reaction is a function of the concentration of the copper ions. As a potential is applied. The surface concentration of copper ions decreases due to the surface flux of ions. This decrease in surface concentration thus leads to a decrease in current. Therefore, the reduction current commences a decrease once it passes the peak.

3.7.2 Effect of concentration on voltammograms

The cyclic voltammograms for 0.025 M, 0.05 M, 0.1 M, 0.2 M and 0.25 M copper (II) in copper sulphate at a scan rate of 50 mVs^{-1} are recorded. The cathodic peaks increase when the concentration of electrolytes increase. The mechanism of the phenomena can also be explained by the Randles–Sevcik equation. It indicates that the rate of diffusion of Cu (II), along with the electrode surface, increases as the concentration of Cu (II) increases. Therefore, a high concentration of solution leads to a high peak current.

Chronoamperometry is an electrochemical technique that is used for copper deposition. The cyclic voltammograms were produced and consulted for the selection of deposition potentials for use in constant potential chronoamperometry. The efficiency of deposition current was studied under three different concentrations: 0.05 M, 0.1 M, and 0.25 M. All of the experiments were terminated at a fixed time rather than a fixed amount of copper deposited. For 0.1 M Cu^{2+} with varied deposition potentials, the results are presented in Figure 3.7.

In Figure 3.7, the potentiostatic transient can be divided into three-time intervals. The first-time interval presents a short beginning period when double layer charging occurs. That leads to a decaying of current during the process of nucleation and growth. In second time interval the current increase. This is due to the growth number of independent nuclei. In the third time interval, growth of nuclei and overlap of nuclei occur at the same time. That effects lead to an increase of current (maximum current) [11]. It can also be observed from Figure 3.7 that the average current increases with the increase of applied potential.

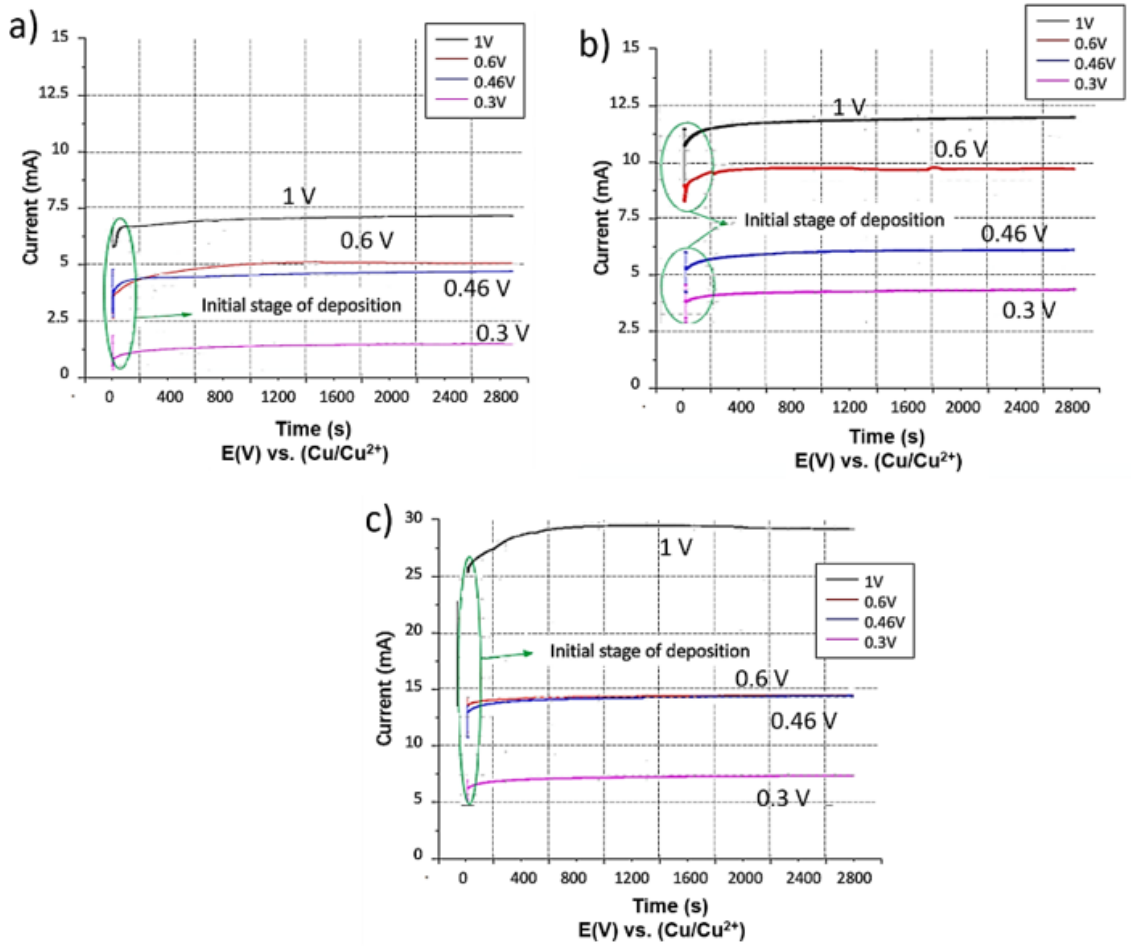

Figure 3.7 Chronoamperometry of copper during electrodeposition on copper electrode. Deposition voltage range: 1V, 0.6V, 0.46V, 0.3V; a) Concentration of 0.05M E(V) vs. (Cu/ Cu^{2+}), b) Concentration of 0.1M E(V) vs. (Cu/ Cu^{2+}), c) Concentration of 0.25M E(V) vs. (Cu/ Cu^{2+}).

In addition, Figure 3.7 shows the total current that passed. If integrating the area of time and current, the overall number of coulombs can be calculated. However, during deposition of copper ions from copper sulphate, two cathodic reactions occur: deposition of Cu^{2+} and decomposition of water. Thus, not all of the charge is used for depositing the copper ions. The current efficiency needs to be calculated. Before the experiment, all of the copper bars were insulted but a small deposition area of 50 mm^2. Then, these copper bars were weighted

before and after the experiments. According to Faraday's Law, the theoretical weight of deposited copper can be calculated as:

$$W = ZQ = \frac{A_{wt}}{nF} \times I \times t \tag{3.8}$$

Current efficiency can be calculated as:

$$CE = \frac{W_{ac}}{W_t} \tag{3.9}$$

Where W is the theoretical weight of copper, Z is the constant of proportionality, Q is the quantity of electric charge, A_{wt} is the atomic weight of copper, n is the number of electrons, I is the current, t is deposition time, F is the Faraday constant, W_t is the theoretical weight, and W_{ac} is the actual weight. Table 3.1 presents current efficiency, corresponding to the theoretical weight (W_t) of copper divided by the actual weight (W_{ac}) of copper at varied deposition potentials with a fixed time (3600 s).

Table 3.1 Current efficiency corresponding to the measured and calculated weight of copper.

Solution concentration		W_b (Before)	W_a (After)	W_{ac} ($W_a - W_b$)	W_t (Theoretical)	CE (Current efficiency)
0.05M	1V	3.0209g	3.0239g	0.0030g	0.0066g	44%
	0.6V	2.9475g	2.9801g	0.0029g	0.0050g	58%
	0.46V	2.7933g	2.7958g	0.0025g	0.0046g	54%
	0.3V	3.1071g	3.1083g	0.0012g	0.0023g	52%
0.1M	1V	2.8988g	2.9077g	0.0089g	0.0143g	62%
	0.6V	3.0886g	3.0974g	0.0088g	0.0139g	63%
	0.46V	2.8487g	2.8527g	0.0040g	0.0071g	56%
	0.3V	2.8991g	2.9018g	0.0027g	0.0052g	51%
0.25M	1V	3.0905g	3.1169g	0.0219g	0.0331g	66%
	0.6V	3.1067g	3.1170g	0.0103g	0.0159g	64%
	0.46V	3.0122g	3.0269g	0.0065g	0.0114g	57%
	0.3V	2.9425g	2.9503g	0.0038g	0.0091g	42%

According to Table 3.1, the highest current efficiency is 66% at 0.25 M with 1 V. The lowest efficiency is 48%, which is under the conditions of 0.25 M concentration and a deposition potential of 0.3 V. Generally, the average current efficiency is around 50%. This relatively low efficient might due to a large ohmic resistance from setup and charge transfer resistance (10 cm distance between two electrodes). The highest current efficiency of 0.1 M is 58%.

The potential between 1V and 0.6V is able to generate a much higher current efficiency than other potentials. To sum up, it shows a better current efficiency at a relatively higher electrolyte concentration and but lower deposition potential. A plot of log (CE) vs log potential (Figure 3.8) describes the abovementioned phenomena.

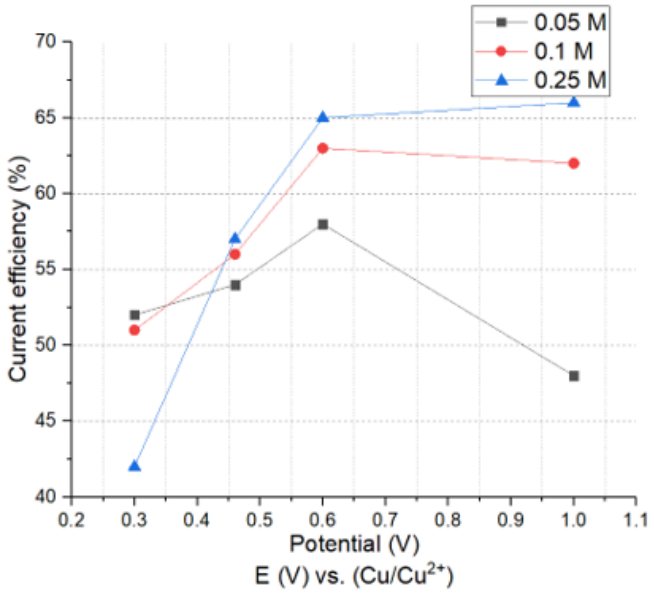

Figure 3.8 A plot of current efficiency (CE) vs. potential (V) for the copper depositions.

3.7.3 Effect of solution concentration on morphology

Figure 3.9 shows the morphology and surface topography of the front and back sides of the copper lines deposited on conductive copper substrate with varying concentrations (1 M, 0.75 M, 0.5 M, 0.2 M, 0.1 M and 0.05 M) of aqueous copper sulphate electrolyte under constant potential of 1 V vs. Cu at a constant deposition time of 1800 s.

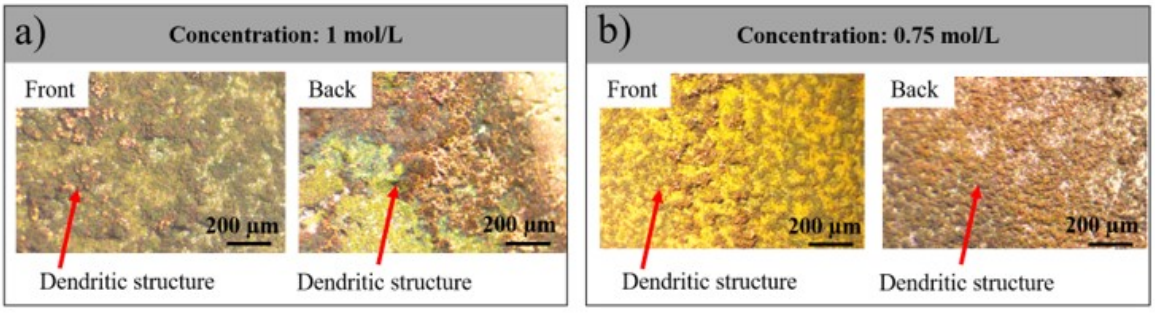

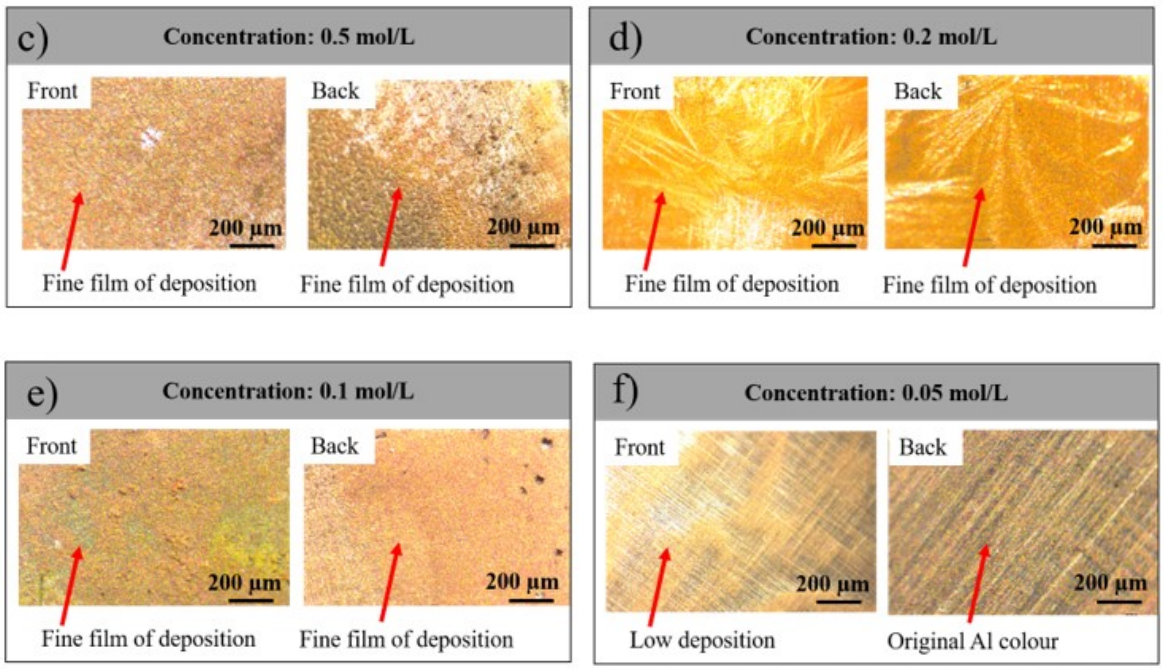

Figure 3.7 Effect of deposition concentration on the morphology of copper deposited under 1V potential [226]. a) - b) high concentration of copper sulphate electrolyte, c) - e) medium concentration of copper sulphate electrolyte, f) low concentration of copper sulphate electrolyte.

As shown in the Figure 3.9 a)-b), a higher deposition potential leads an uneven deposition morphology. This is likely due to the higher concentration leading to higher deposition current density, which in-turn, leads to more aggressive concentration gradients being generated which can lead to the dendritic structures observed. Particularly in Figure 3.9 a), a poor surface finish can be observed in both front and back side of electrode from an optical microscope. Local concentrations mostly affect the density of copper deposition. Higher concentration could lead to a much higher density [230]. However, the surface morphology may become more porous and not uniform as a result of fast deposition and high current flow.

As a comparison, lowering the concentration results in a lower number of ions available for discharge and hence creates a depletion layer just beneath the deposition needle. The optical images shown in Figure 3.9 f) demonstrated that concentrations lower than 0.1 M result in smooth surface deposition. This is likely due to the lower reaction current density allowing time for the diffusion of copper ions to the electrode surface. A lower reaction current density at low concentrations is due to the higher charge transfer resistance which can be inferred from the Butler-Volmer equation. Here, the exchange current density is a function of the reductant and oxidant, with lower concentrations of copper ions leading to a lower exchange current density. At moderate high concentrations (from 0.75 M to 0.1 M), Figure 3.9 b)-e)

show the irregular crystal shapes and relatively small crystalline (~1 μm), which is a typical result of irregular growth. The increasing concentrations resulted in the availability of a large number of ions and hence, favors the formation of spongy, high porous and protruding crystals, resulting in larger surface roughness. This rapid position is most favourable at the tip of a deposition leading to the formation of mossy metallic growth. As this structure grows, the diffusion of copper ions into deeper regions of the porous deposition creates unfavorable deposition conditions in the porous regions.

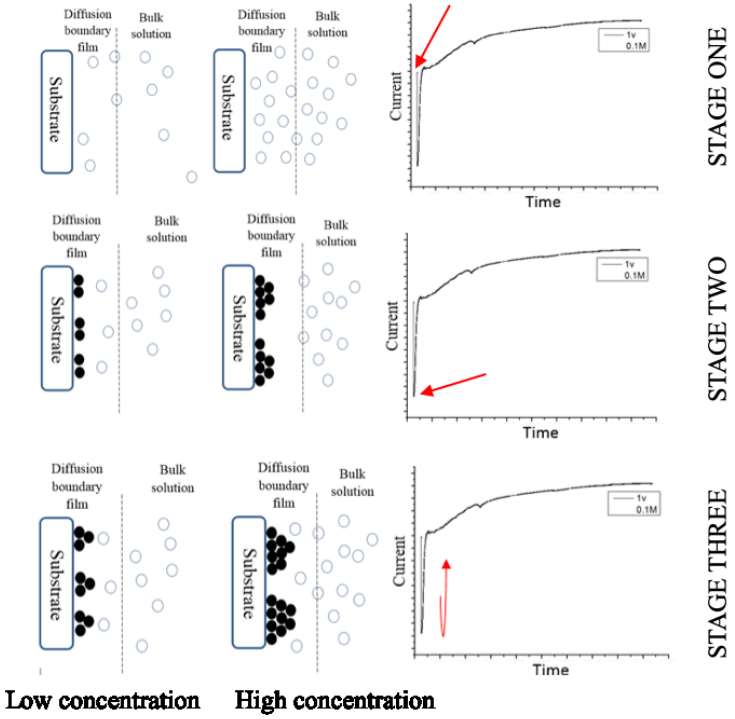

Figure 3.10 Schematic illustration of copper deposition under lower and higher concentrations at three stages of constant potential experiments. Stage one is prior to electrodeposition, stage two is ongoing deposition, and stage three is steady deposition [230].

Under the lower concentration conditions, copper ions are spaced farther apart compared with those of the higher concentration in Figure 3.10. The copper ions have to bond together to minimise the surface energy once deposition begins. For lower concentration, ions are distributed farther apart, which increases the travel distance for ions to group together. That results in a small ion-composited group but in a large number of groups. In contrast, higher concentration will result in more ions forming a large group with small quantities. Therefore, the morphology at lower concentration shows a dense distribution but a small size. The higher concentration shows the opposite phenomenon [230].

3.7.4 Effect of deposition potential on morphology

The electrochemical side reaction that takes place at the needle is the decomposition of water,

$$H_2O \rightleftharpoons 1/2\ O_2 + H_2 \quad (3.10)$$

While at the substrate, Cu^{2+} ions are reduced via the deposition reaction.

$$Cu^{2+} + 2e^- \rightleftharpoons Cu \quad (3.11)$$

From the above processes, copper deposits at the substrate and at sufficiently high potentials, and gas is generated from the decomposition of the aqueous electrolyte. Figure 3.11 shows the measured current (passing between the counter electrode and the substrate) upon varying the applied potential from 1.0 to 5.0 V at constant $CuSO_4$ concentration of 1 M. The figure shows that up to 3 V, the current is very low (less than 0.36 mA). Figure 3.11c shows the deposition process under low potential where Cu^{2+} directly reduced via reaction (3.12) forming smooth Cu on the substrate. The micrograph of the smooth surface morphology formed at potential 1V is shown in Figure 3.11.

As the potential increases, both the current and deposition rate increases, and the rate of deposition reaches a maximum of about 850 μm/min at 5V. The micrograph of the surface morphology formed at 5V can be seen from Figure 3.11 showing the deposited Cu as rough, spongy and porous. This can be explained as follows: i) during electrodeposition, diffusion is the rate-determined process [231]. At higher potential, the solution beneath the needle become depleted in the ions required for discharge and gas can be evolved if the decomposition potential of water is exceeded (Figure 3.12); ii) bubble formation often generated by water splitting and can block the copper deposition, interfere with crystal growth, and result in surface morphology with a high roughness. Also, at potentials above 4 V the resulting current also becomes unstable which is likely due to the formation and detachment of gas bubbles on the surface of the electrodes. This can be minimized by either increasing the diffusion rate or lowering the current density by lowering the potential so the diffusion of ions will occur slowly [118].

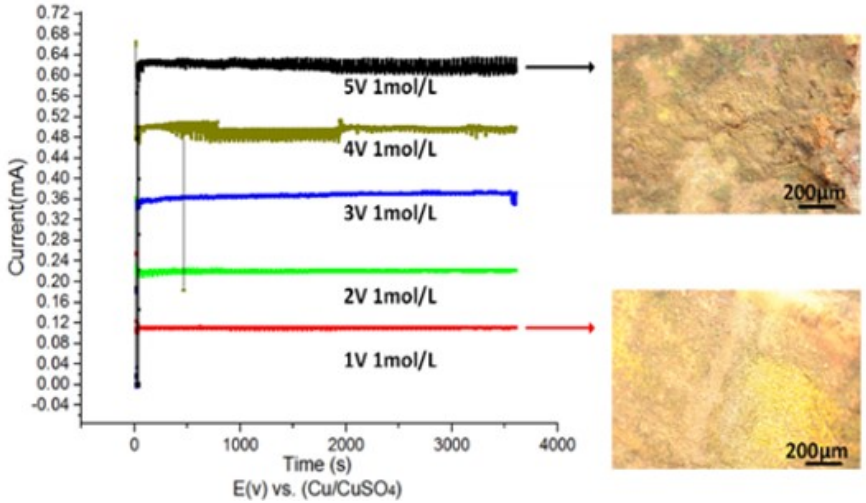

Figure 3.8 a) Effect of deposition potentials on the morphology of copper deposited under 1M concentration; illustration of surface.

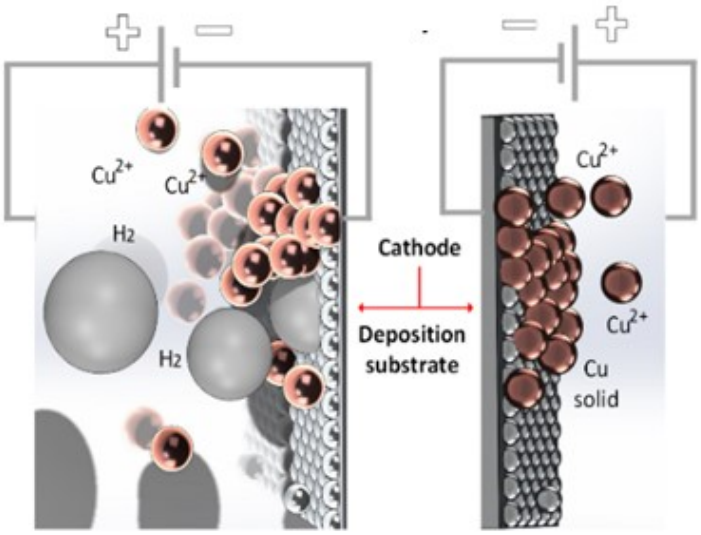

Figure 3.9 Illustration of surface morphology of Cu^{2+} electrodeposition under b) high potential (left) and c) low potential (right) [226].

3.7.5 Mass transport and current distribution

Mass transport and current distribution are crucial for successful electrochemical deposition processes. Mass transport is one of the major rate limitations in an electrochemical fabrication process. The mass transport conditions affect the microstructure of deposited copper and the surface topography resulting from anodic dissolution. The current distribution determines the uniformity of the thickness of an electrodeposit. During the electrochemical process, a non-homogeneous distribution of partial currents can lead to local variations in composition.

3.8 Conclusions

The design of a meniscus confined ECAM metal 3D printer is presented, with the focus covering the investigation of several designs of the meniscus-confined print heads. The novelty of this work focuses on the material-filled (sponge-assisted and nanofiber-assisted) nozzles in the print head, which is significantly larger than other designs due to the use of the porous sponge or electro-spun nanofiber mat to create a back pressure for the hydraulic head created by the electrolyte. This larger print head allows printing of polycrystalline copper structures, at a volumetric deposition rate, 3 order of magnitude higher than other reported systems. The results verified the printability of the system with a fast deposition speed (19,677 $\mu m^3.s^{-1}$), especially for large-scale single metallic (copper) structure fabrication. Some limitations were however, also observed: i) the simple mechanical sample removal process from the substrate can easily break the deposited structure, which could be a barrier to scale up for manufacturing complex structures. Sacrificial support materials could be considered for sample removal, however, could increase the complexity of the manufacturing process; ii) crystal deposits on the substrate from the residual liquid left behind from meniscus trail, affects the printing process and will result in low print quality. Solutions such as regular washing or alternative hydrogel nib designs could be considered to optimize the design in the future.

Chapter 4 3D Printing and Characterization of Single Dots and Lines

This chapter presents the characterization of the printed product from the electrochemical 3D printer where some of the content has been published in a journal paper: Chen, X., Liu, X., Childs, P., Brandon, N.P., Wu, B., 2017. A Low Cost Desktop Electrochemical Metal 3D Printer. Advanced Materials Technologies, 2(10), p.1700148. As the first author of this publication, I led most of the tasks, including design and modification of the device, data collection, data analysis, drafting the article. The co-authors supervised and co-supervised the work, contributing to the critical revision of the article and final approval of the version published.

4.1 Introduction

This chapter describes and discusses the initial assessment of the low cost electrochemical metal 3D printer by printing copper dots, lines and letters. Experimental work and assessment tests are conducted to identify the properties of the printed structures. This will form the foundation of later multi-materials analysis work. The below therefore summarised the contents in this chapter.

- **Printing strategy for single dot, single line and letter fabrication**
  The single dot, line and letter are fabricated with the Desktop Electrochemical Metal 3D printer using the sponge-assisted print head. The material preparation, operation parameters and fabrication steps for printing these structures are detailed in this section.
- **Assessment methods**
  This section outlines the assessment methods for the printed structures as the initial validation for the 3D printer. Scanning Electron Microscopy (SEM). Vickers Hardness test, Eelectrical conductivity test, Indentation test and Resistivity test are conducted.
- **Assessment results and discussion**

Morphological, mechanical and electrical properties of the printed structures are assessed and presented in this section. The results will verify the printability of the system, such as the deposition speed and fabrication resolution, as well as the quality of the printed structures.

4.2 Printing strategy for single dot, single line and letter

In the singe dots experiments, a 1 M $CuSO_4$ electrolyte was prepared by combining 12.5 g of $CuSO_4 \cdot 5H_2O$ (Sigma Aldrich) and 50 mL of deionized water. The copper substrate was prepared by cutting a 30 mm x 30 mm x 0.3 mm pure copper sheet. The substrate was cleaned with acetone and deionized water before use to remove any dirt and oils which might affect the deposition. Deposition duration was fixed at 3,600 s for all experiments. Temperature and relative humidity was at room conditions which were 20 °C and 30%-45% respectively. The nozzle was placed firmly to substrate without electrolyte leaking. For single lines and letters, the deposition conditions and electrolyte were prepared in the same manner as the single dots. The nozzle was controlled to move along x axis by a distance of 10 mm and 3,600 s duration with a speed of 0.4 $mm.s^{-1}$, with144 passes being made.

4.3 Material preparation and assessment methods

4.3.1 Copper sulphate preparation

Copper sulphate electrolytes were prepared by mixing anhydrous copper (II) sulphate (≥99.99% pure – Sigma Aldrich) with deionized water.

4.3.2 Scanning Electron Microscope

SEM images were taken with a Phenom ProX in backscattered mode with an acceleration voltage of 5 kV with no sample sputtering. Samples were mounted onto SEM sample stubs and adhered to using carbon tape. No sputtering of the samples was performed.

4.3.3 Conductivity test

Deposition and electrical conductivity measurements were conducted using a Metrohm Autolab PGSTA302N in a 4-electrode configuration.

4.3.4 Hardness test

Hardness measurements were conducted using a Zwick-ZHV1 micro Vickers hardness machine. Silicon carbide paper with a grade of 1500 was used to polish all samples before epoxy mounting. During the experiments, a minimum load of 10 gmf was applied to all samples with creep time of 10 seconds.

For the Vickers-indentation test, the tip angle was 136°. The diagonal length of the contact area can be used to calculate the HV value using the below formula:

$$\mathrm{HV} = \left(\frac{0.1891F}{d^2}\right) \tag{4.1}$$

Where, F is the applied load (mN), d is the diagonal length of contact area (mm).

4.3.6 Resistivity test

To test the resistivity of very thin single lines formula below was used:

$$\rho = \frac{VA}{Il} \tag{4.2}$$

Where, V is the applied voltage, I is the current according to the applied potential, A is the cross-sectional area and l is the length of the sample between the measurement points. Measurements were taken in 4 electrode mode at a current of 2 mA to ensure contact resistance between the sample and the probes did not affect the measurements.

4.4 Assessment results and discussion

4.4.1 Morphological results of single dots

Fabrication of dots were performed using a copper sulphate concentration of 1 M with deposition voltages ranging from 1 V - 6 V vs. Cu under ambient conditions. Figure 4.1 shows the SEM micrographs of the printed dots with a deposition time of 1 hour. Further SEM micrographs (top and bottom view) of Cu single dot vs. 1V-6V potentials, deposited in a 1M $CuSO_4$ solution after 1 hour, are shown in Figure 4.2 (a)-(i). Of the samples, the 1 V deposition exhibited the most ideal morphology, with a dense structure and high degree of concentricity due to the meniscus confinement approach. The 2 V vs. Cu sample showed a faster rate of growth with a dense structure, however exhibited a convex shape due to preferential deposition at the center. At 3 V vs. Cu, the formation of copper dendrites becomes apparent due to mass transport limitations with the severity and porosity continuing to increase with increasing deposition potential. At 4 V vs. Cu, the base of the deposition becomes dendritic also but with a finer morphology compared to higher regions. The switch between fine and course dendritic structures between the base and upper regions of the dots suggest that there is a shift in the deposition conditions which may arise due to the interplay between diffusion and migration, as well as different nucleation kinetics on the neat copper substrate vs. a copper dendrite.

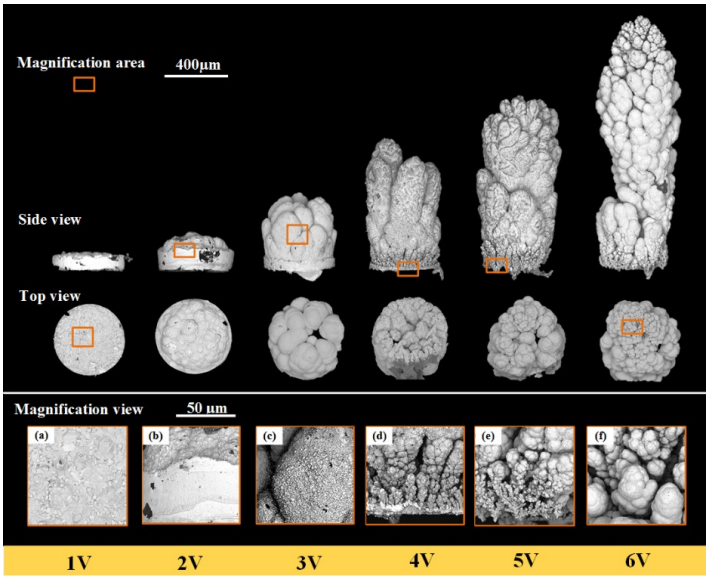

Figure 4.1 SEM images of single dot copper depositions at different potentials: a) top view of single dot at 1V; side views of single dot at b) 2V; c) 3V; d) 4V; e) 5V; f) top view of single dot at 6V [92].

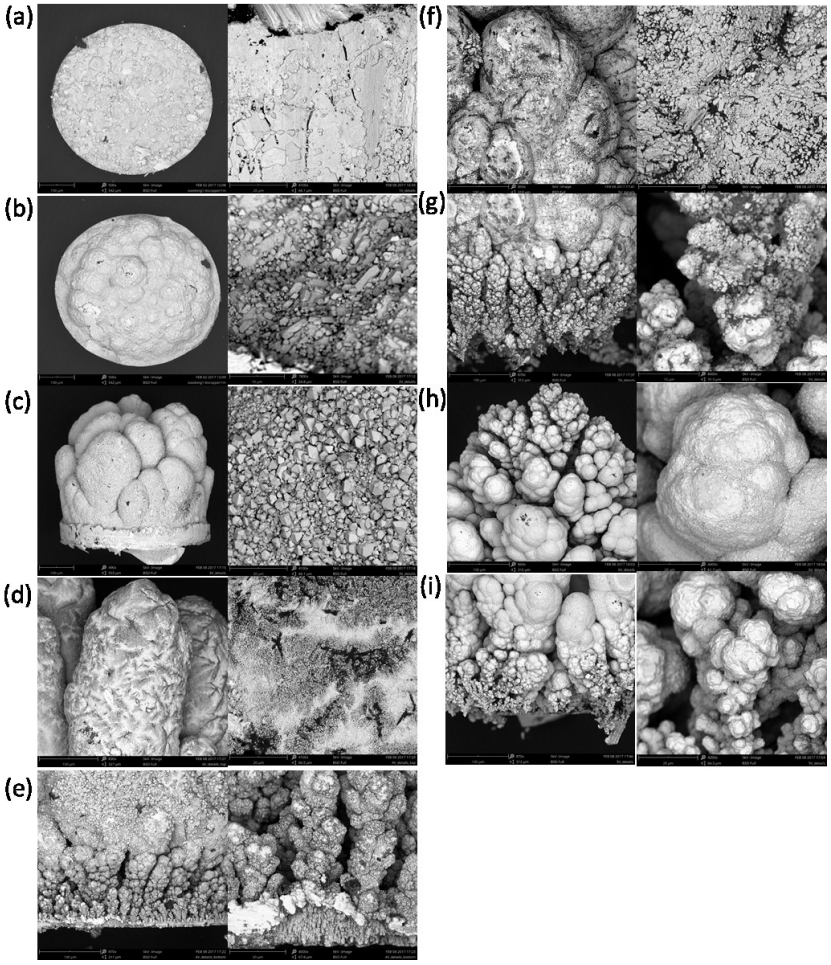

Figure 4.2 SEM micrographs of deposits at (a) 1V; (b) 2V and (c) 3V; (d) top view and (e) bottom view of 4V; (f) top view and (g) bottom view of 5V; (h) top view and (i) bottom view of 6V vs Cu single dot deposition from a 1M $CuSO_4$ solution for an hour.

The SEM images suggest all samples are polycrystalline with a decreasing grain size with increasing deposition potential suggesting there is a shift in the physical properties. A similar phenomenon was also observed by Molares *et al.* [232], who produced copper nanowires using electrochemical deposition. During electrochemical growth of copper, two mechanisms occur simultaneously: i) growth of existing nuclei and ii) nucleation followed by formation of new grains. The two processes complete with each other and was influenced by parameters such as current density (applied potential) and temperature. They observed that deposition of large crystals is favored in the case of decreased current density. The decreased current density and increased temperature both lead to a decrease of the cathode polarization, to promote a more efficient transport of the ions towards the electrode. Zhang *et al.* [233] conducted *in-situ* optical microscopy to observe the growth process of the deposits during the electrochemical deposition of copper with a 0.05 M $CuSO_4$ electrolyte. The results further verified the conclusions addressed by Molares *et al.* [232] that when the cell voltage increases, the cathode over-potential reaches the deposition potential for Cu, and this promotes the nucleation and growth process, resulting in the formation of crystals of smaller sizes. Whilst deposition speed naturally increases with a higher potential, the morphology due to mass transport limitations beyond 2 V vs. Cu needs to be addressed in order to achieve dimensionally accurate structures.

4.4.2 Morphological results of single lines

The single lines are also fabricated using a copper sulphate concentration of 1 M with deposition voltages ranging from 1 V-6 V vs. Cu under ambient conditions. Figure 4.3 shows the SEM micrographs ((a)-(f)) of the printed single lines now with a lateral print head velocity of 0.4 $mm \cdot s^{-1}$ and the same deposition conditions of 1 M $CuSO_4$ and ambient conditions over a potential range of 1 V- 6 V vs. Cu. The trends of the morphology vs. supplied potential are the same as the investigations of single dots. The formation of pure elemental copper was confirmed through energy dispersive x-ray spectroscopy (EDS) measurements (Figure 4.4).

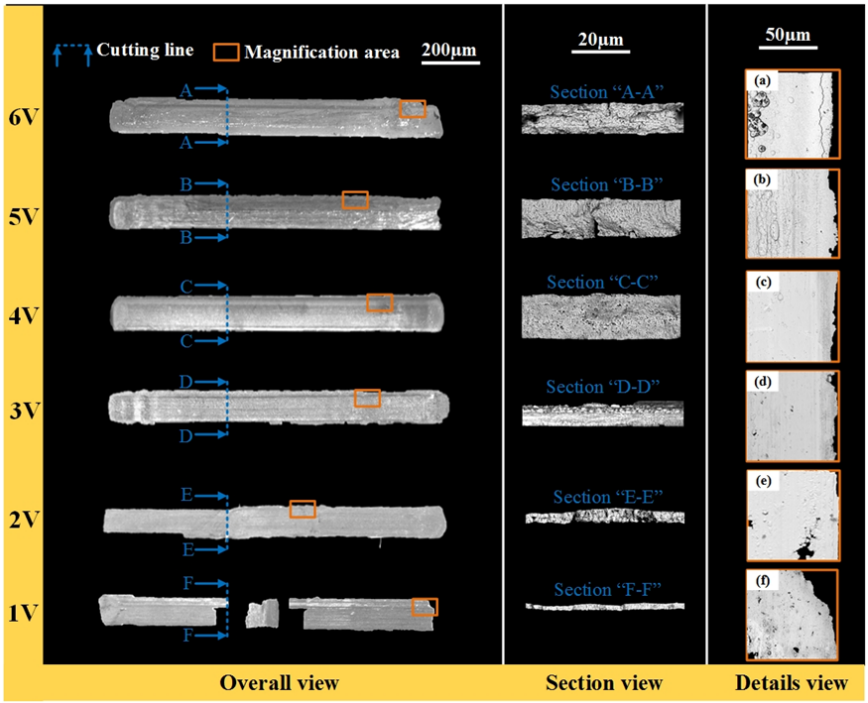

Figure 4.3 Optical and SEM micrographs of the morphology of the printed lines under printing potentials 1-6V ((a)-(f)) for a 1 M $CuSO_4$ solution after 1 hour with a lateral speed of 0.4 $mm.s^{-1}$ [92].

Of note is the fact that the deposition morphology is no longer dendritic suggesting that the relative motion of the print head aids with mass transport of copper ions or mechanical removal of the dendrites. For a 1 hour deposition it can be observed that the line thickness increases from 3 μm at 1 V vs. Cu to a peak of 15 μm at 4 V vs. Cu after which there is a decrease in deposited material, due to falling deposition efficiency. Given the lateral speed at 0.4 $mm.s^{-1}$ over a distance of 10 mm and time of 3600 s, this suggests that 144 passes were made. From Figure 4.3, the line thicknesses ranged from 3-15 μm, which suggests a layer thickness of 14-104 nm. This is confirmed from the striations observed in the magnified view of the 5 V vs. Cu deposition. This suggests that the z-height resolution of this process is exceptionally high and opens the possibility of this technique in the fabrication of functional electronics such as sensors.

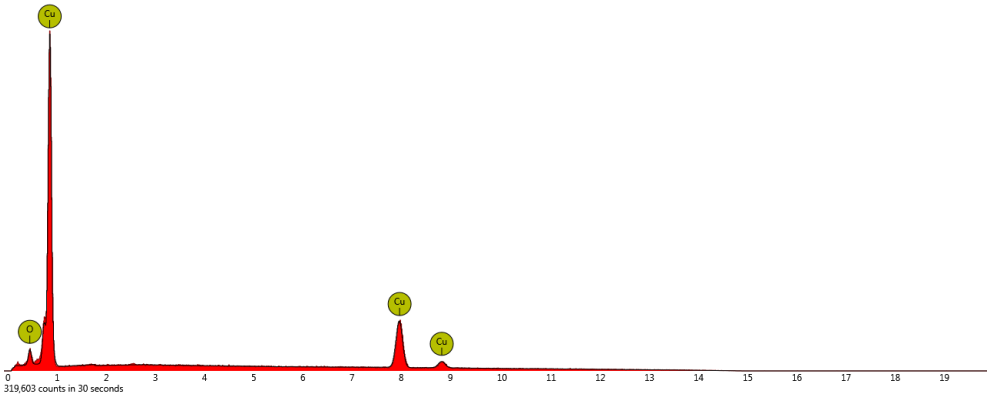

Figure 4.4 EDS spectra of 5 V vs. Cu printed line from a 1 M $CuSO_4$ solution after 1 hour.

4.4.3 Morphological results of letters

The optical and SEM images of the printed letters 'ICL' are presented in Figure 4.5, which uses a deposition potential of 4 V vs. Cu, with a 1 M $CuSO_4$ concentration and print head speed of 0.4 $mm \cdot s^{-1}$.

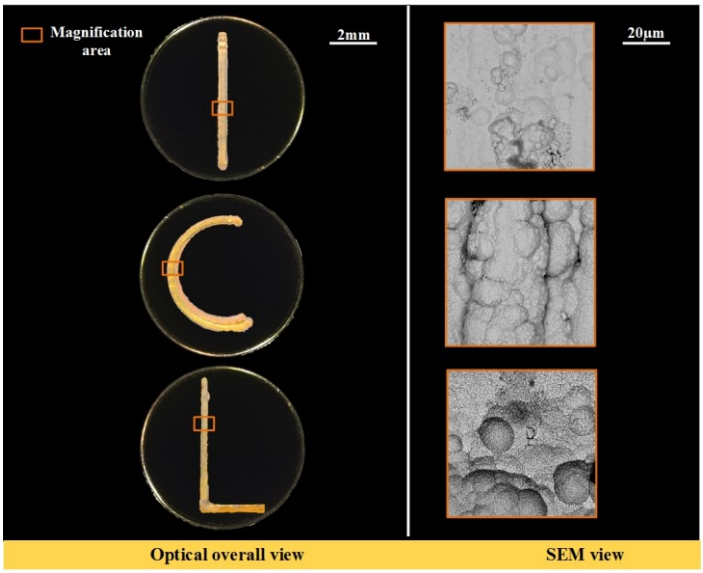

Figure 4.5 Optical and SEM images of the printed "ICL" letters with a potential of 4 V vs. Cu.

4.4.4 Hardness and electrical conductivity of printed dots and lines

The highly polycrystalline nature of the printed structures suggest that the mechanical properties of the printed structures deviate from conventional cold worked cast copper. Figure 4.6a shows the Vickers hardness of the copper dots and lines. For a single dot, the hardness ranges from 184-196 MPa with values increasing with deposition potential most likely due to the decreasing grain size. The Vickers hardness of the printed line exhibited even higher values ranging from 211-228 MPa, likely due to even further smaller grains due to the mechanical agitation increasing the rate of deposition. As a reference, the hardness of copper used in circuit bonding wires can range from 50 to 176 MPa [234].

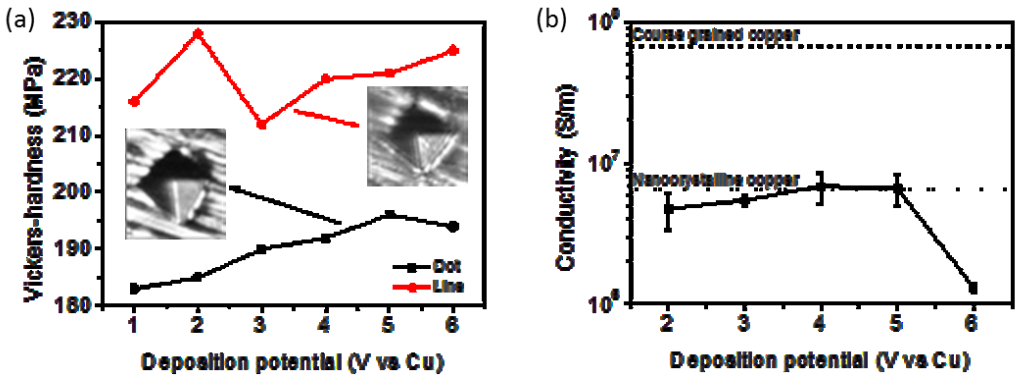

Figure 4.6 (a) Vickers-hardness measurements of the printed lines and dots; (b) Electrical conductivity measurements of the printed lines [92].

Figure 4.6b demonstrates the result of the conductivity measurements of single lines via a four-probe apparatus. Here the electrical conductivity of samples was found to range between 1.31×10^6 S/m and 6.86×10^6 S/m. This is broadly 1 order of magnitude below the conductivity of course grained copper (5.92×10^7 S/m) reported by Lu *et al*. [235] but agrees well for nano-crystalline copper (5.41×10^6 S/m) measurements supporting the observation that the electrodeposition of copper results in highly nano-crystalline structures. The current density for the various depositions are shown in Figure 4.7. Whilst deposition speed naturally increases with a higher potential, the morphology due to mass transport limitations beyond 2 V vs. Cu needs to be addressed in order to achieve dimensionally accurate structures.

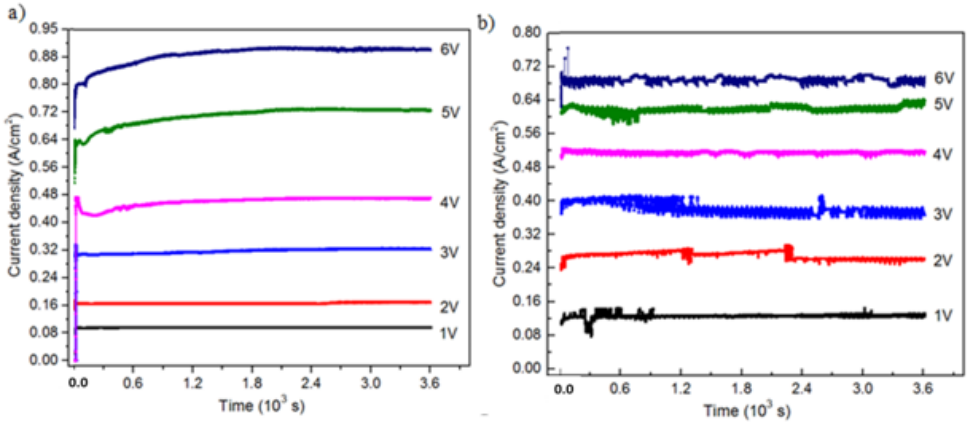

Figure 4.7 a) single dot current density and b) single line current density from a 1 M $CuSO_4$ solution

4.4.5 Limiting current from E/I against 1/I plot

The current density of electrochemical additive manufacturing is usually related to the biased potential, inter-electrode gap, and bulk concentration of electroactive ions. In our system, the inter-electrode gap has been fixed. The electrolyte flow was controlled by a porous sponge to balance the hydraulic head and to maintain a stable meniscus. The mass transfer of copper ions is governed by diffusion, migration and natural convention during the ECAM process. Therefore, the limiting current is affected by the applied voltage and the concentration of ions. The modelling work done by Morsali et al. [236] decouples the various contributions to ionic flux and shows that the relative contributions of convection, diffusion and migration are of the same order of magnitude. In the case of the applied voltage, this will affect the local electric field and thus the relative amount of migration, and thus the limiting current density, which is a function of the mass transport characteristics of the system. It can be determined by the experimental current - voltage curve. It can be estimated from the cyclic voltammetry (CV) by plotting E/I against 1/I based on the work by Leon and Field [236]. Of which Equation (4.4) and (4.5) show the relationships between these metrics of interest.

$$\frac{d\,(E/I)}{d(1/I)} = \frac{d(E/I)}{d(I)} \times \frac{d(I)}{d(1/I)} \tag{4.4}$$

$$= -I\left[\left(\frac{d(I)}{d(E)}\right)^{-1} - \frac{E}{I}\right] \tag{4.5}$$

Where, E is applied potential (V), I is current (A).

The author suggests that the limiting current is approached when $\frac{E}{I}$ decreases. There are two turning points in the suggested plot. The first turning point corresponds to when the term in the square bracket in Equation (4.5) to be zero, and d(I)/d(E) is sufficiently low. The second turning point occurs when d(I)/d(E) increases resulting the term in square brackets to become negative again. The mid-point between the two turning points corresponds to be the mass transfer limitation [237].

Figure 4.8a shows CVs of 0.1 M, 0.25 M and 0.5 M Cu2+ in copper sulphate between ± 1 V at a scan rate of 10 mV s-1. This scan rate was chosen for the calculation of limiting current since it is slow enough to allow ECAM system to get equilibrium status. Figure 4.8b is the corresponding E/I against 1/I from Figure 4.8a for a forward linear sweep. The calculated limiting current density are presented in Table 4.1, which is - 0.048 A/cm^2 at 0.1M, - 0.094 mA at 0.25 M and - 0.168 mA at 0.5M. A 400 µm pipette was used for a single line printing with the print head moving speed of 0.1 mm s^{-1}.

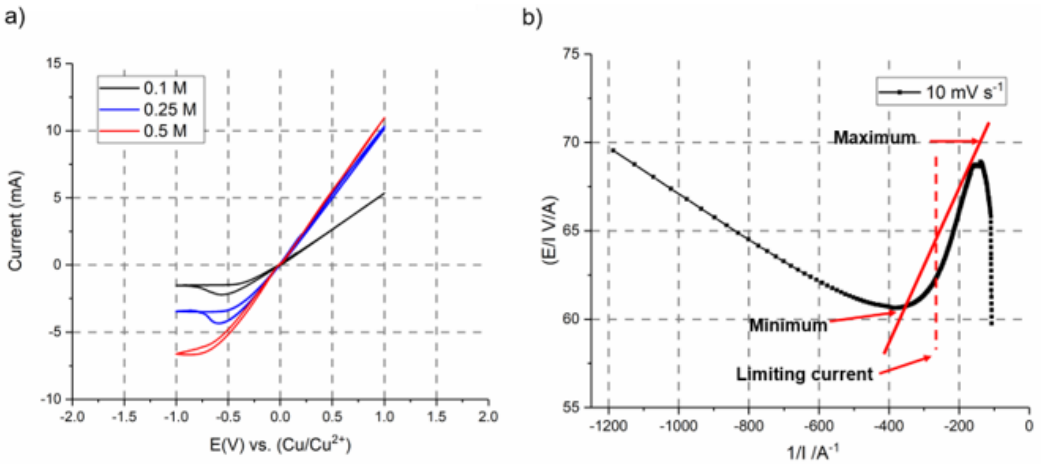

Figure 4.8 (a) the cyclic voltammetry of 0.1 M, 0.25 M and 0.5 M Cu^{2+} in copper sulphate at 1 V with scan rates of 10 mV s^{-1}. (b) Illustration of procedures for determining the limiting current of 0.25 M Cu^{2+} in copper sulphate at 10 mV s^{-1}

Table 4. 1 The limiting current density for the reduction of Cu^{2+} at a scan rate of 10 mV s^{-1}

Concentration (M)	**Current (mA)**			**Area (cm^2)**	**Limiting current (A/cm^2)**
	Minimum	Maximum	Mid-point		

0.1	-1.38	-2.46	-1.92	0.04	- 0.048
0.25	-2.63	-4.87	-3.75	0.04	- 0.094
0.5	-6.42	-7.03	-6.73	0.04	- 0.168

Figure 4.9a shows the morphology of printed copper line at the limiting current density of -0.048 A cm^{-2} in the concentration of 0.1 M Cu^{2+} in copper sulphate. From the optical image, it presents a discontinuous formation of copper. This is then likely due to the growth rate of copper is much slower than the print head moving speed. A detailed SEM image reveals that a nano-crystalline structure was formed during the deposition. Increasing limiting current density to -0.094 A cm^{-2} in the concentration of 0.25 M, Figure 4.9b shows a denser deposition morphology suggesting deposition growth rate increase with limiting current density. A fine grain size of deposited copper can be observed from enlarged SEM image. By further increasing limiting current density to -0.168 A cm^{-2} in the concentration of 0.5M, Figure 4.9c shows an optical image with an even denser structure which off stand from substrate. However, this copper line presented a rough surface morphology in convex shape in SEM. The trend of surface morphology against limiting current density shows a switch between find and rough copper structure indicating that the optimum limiting current density is -0.094 A cm^{-2} in the concentration of 0.25 M at a print head moving speed of 0.1 mm s^{-1}.

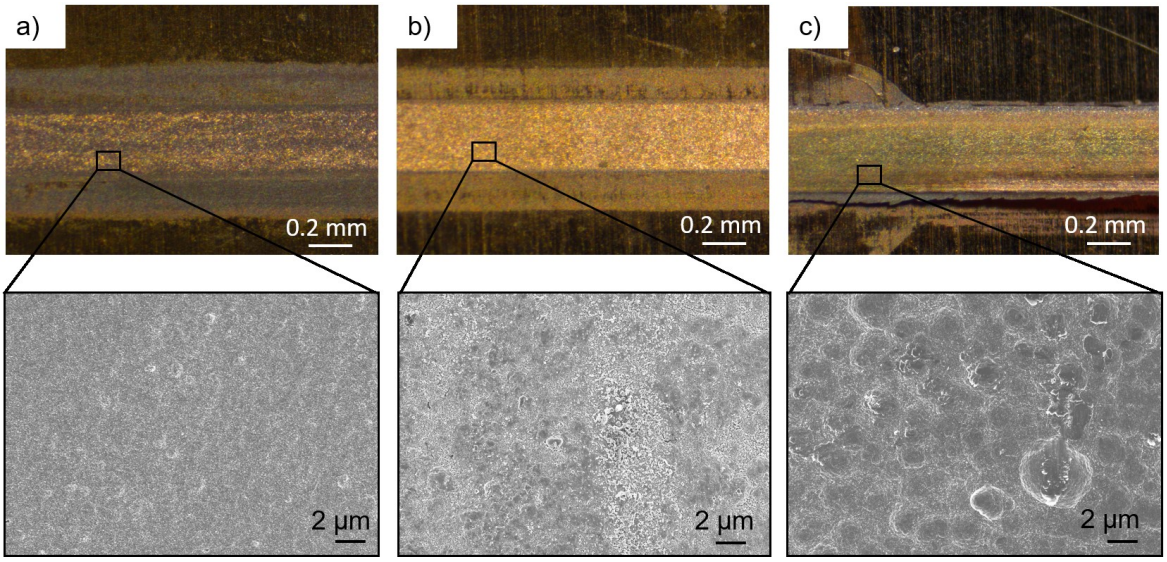

Figure 4.9 Illustration of surface morphology of printed copper line (a) Optical image of printed copper line at the limiting current of -0.048 A cm^{-2} with an enlarged SEM image, (b) Optical image of printed copper line at the limiting current of -0.094 A cm^{-2} with an enlarged SEM image, (c) Optical image of printed copper line at the limiting current of -0.168 A cm^{-2} with an enlarged SEM image

4.5 Conclusions

The work presented demonstrates that large scale (400 µm nozzle) meniscus confined electrochemical printing is possible through the novel printer design proposed. This concept balances the hydraulic head of a static electrolyte with the back pressure of a sponge filled

nozzle to form a stable meniscus. Static printing of copper dots from a 1 M $CuSO_4$ solution gives dense prints at low voltages of 1 V vs. Cu however at increasing voltages >3 V vs. $CuSO_4$ there is an evident evolution of dendritic structures due to the diffusion limitations of the Cu^{2+} ions. The novel concept of print head movement has been shown to suppress dendrite formation, likely due to the mechanical agitation of the electrolyte through entrainment effects. This thus, enables a faster rate of deposition of up to 19,667 $\mu m^3.s^{-1}$ without noticeable dendritic formations. Whilst static retraction rates for the single dot ranged from 0.03 μm/s – 0.6 μm/s the volumetric deposition speed is 3 orders of magnitude faster than previously reported copper deposition studies (20.4 $\mu m^3.s^{-1}$) opening the possibility for the printing of larger structures. Printed structures had a noticeable polycrystalline grain structure, with decreasing grain size with increasing deposition potential. Mechanical and electrical characterization show that the Vickers hardness and electrical resistivity are higher than cold worked cast copper due to the fine grain structure. This work therefore builds a foundation for future work on high speed and low cost ECAM with expanding research areas such as multi-material functional structures.

Chapter 5 Metal 4D printing of multi-material structures with a desktop electrochemical 3D printer

This chapter presents results on extending the electrochemical printer to multiple materials. Some of the content has been published in a journal paper: Chen, X., Liu, X., Ouyang, M., Chen, J., Taiwo, O., Xia Y., Childs, P., Brandon, N. P., Wu, B., 2019. Multi-metal 4D printing with a desktop electrochemical 3D printer. *Scientific Report.* 9 (1), pp. 1-9. As the first author of this publication, I led most of the tasks, including design and fabrication of multi-material structures, data collection, data analysis, drafting the article. The co-authors supervised and co-supervised the work, contributing to the FEA simulation, critical revision of the article and final approval of the version published.

5.1 Introduction

4D printing has the potential to create complex 3D geometries which are able to react to environmental stimuli opening new design possibilities. However, the vast majority of 4D printing approaches use polymer based materials, which limits the operational temperature. Here, we present a novel multi-metal electrochemical 3D printer which is able to fabricate bimetallic geometries. The concept is demonstrated through a meniscus confined electrochemical 3D printing approach with nickel and copper as exemplar systems but this is transferable to other deposition solutions. Here, we demonstrate a novel approach to achieve 4D metal structures through multi-metal ECAM using a meniscus confined approach with multiple syringes.

This Chapter presents the fabrication of Cu-Ni bilayer strip and Cu-Ni-Cu trilayer strip fabrication with the further development of the electrochemical 3D printer with two deposition nozzles for multi-material 4D printing (described in Section 3.4), where an improved version of nanofiber-assisted print nozzle was used (described in Section 3.2.3). This work will explore basic research of in multiple metals shape morphing with expanding

research in complex metal 4D printing. This chapter therefore contains the following sections:

- **Printing strategy for multi-material multi-layer strips fabrication**

  Cu-Ni bilayer strips and Cu-Ni-Cu trilayer strips are fabricated with the desktop electrochemical metal 3D printer equipped with dual nanofibre-assisted print heads. The material preparation, operation parameters and fabrication steps for printing these structures are detailed in this section.

- **Assessment methods**

  This section outlines the assessment methods for the printed structures as the further validation for the 3D printer. A systematic assessment of impact factors, such as layer thickness, temperature, deposition position, metallic conductivity and metallic surface morphology has been investigated.

- **Assessment results and discussion**

  This section present the assessment results to explore the possibility shaping the multi-material multi-layer strips by changing temperature and altering the layer thickness, allowing for fabricating functional and customized thermal meter or thermal electronics.

5.2 Multi-metal 3D printing

There are current research efforts to expand metal 3D printing to include multi-metal capabilities. For example, Li *et al.* [238] demonstrated the deposition of various metal carbides, such as titanium carbide, tungsten carbide, and silicon carbide into a titanium alloy matrix via a process whereby titanium wires and the metal carbide powder are fed into a melt pool formed by a laser. The wire and powder fed process makes metal composite printing feasible however, the printed part has limited dimensional accuracy and high surface roughness. Onuike *et al.* [239] demonstrated the fabrication of a copper and nickel alloy bimetallic structure using laser engineering net shaping (LENS), whereby a metallic powder is fed into a melt pool formed with a laser. Here they explored bimetallic structures through a sequential deposition and a functional grading of the two alloys with both approaches showing improvements in the thermal conductivity relative to a baseline Inconel 718 alloy. However, due to the powder spraying based approach the dimensional accuracy of the printed parts were limited and also the aggressive thermal conditions resulted in significant thermal stresses which can lead to layer delamination in multi-metal systems [240].

In addition to additive manufacturing of multilayer metals, cast surfacing is a convention method in producing corrosion-resistance and wear-resistance bimetallic sheets. A blank mould is equipped with multiple plates where liquid metal is then drop casted. A subsequent high-pressure treatment is needed to produce the final bimetal sheet. The number of metal layers corresponds to the number of plates [241]. Although this method is straight forward and inexpensive, it limits the control over the bimetallic layer thickness. A high melting point plate is also often needed to contain and separate the liquid metals, which limits the choices of metal. This method is also not suitable to produce thin layer bimetallic sheets since a gate plate with high thickness is applied between the metal layers. Continuous casting was invented to introduce a plate free process in producing bimetallic sheets [242]. However, a large blank mould with length varying from 4 to 10 metres is normally needed which limits its widely application [241]. In addition, control of the bimetallic layer thickness is still lacking. The boundary of the two layers is often loosely bonded. Welding was then applied to produce bimetallic products with sufficiently formed bond at the bilayer [243]. A significant benefit of this method is the ability to bind any type of metal, with controllable thickness ratios of layers. However, poor flatness in welded bimetallic products is observed due to the air trapped during the welding process. For example, the primary surface profile height ranged from approximately -10 mm - 25 mm for friction-welded bimetal (Al-Ti) specimen [244].

This casting methods are also considered very hazardous. Cold surfacing, in contast, is regarded as a widely applied method in producing thin bimetallic strip at an industry level [245]. It consists of fabrication steps including: material loading, cold surfacing, heat rolling, cold rolling and trimming. It is employed a wide range of materials, such as steel, aluminium, copper, nickel, and titanium. However, the curvature of the fabricated bimetallic part is observed due to the nonuniformity of the strips during rolling [246]. Therefore, multiple metal 3D printing is proposed as a new method for producing bimetallic strips in a safe manner, relatively low cost, and broad choice of materials with fine control over the location of the metals.

5.3 Printing strategies

The fabrication process for a copper-nickel bimetallic strip is schematically demonstrated in Figure 5.1**.** Here one syringe is filled with electrolyte for deposition while the other one remains empty to avoid undesirable electrolyte mixing solutions. In the first stage, (Figure 5.1a) a copper layer is deposited from an aqueous copper sulphate electrolyte. Here, a stable

electrolyte meniscus is formed between the nozzle and the substrate by balancing the hydraulic head of the electrolyte with the surface tension of the electrolyte and back pressure of a porous media in the print nozzle. A potentiostat then applies a constant potential to reduce the Cu^{2+} ions in the electrolyte to metallic copper on the substrate. Simultaneously, the consumed Cu^{2+} ions are replenished from counter electrode through the oxidation of the electrode, maintaining the overall concentration but forming a concentration gradient in the solution. This concentration gradient can affect the current density and morphology of the printed copper. Earlier sections used sponges with a random open pore structure to provide suitable back pressure to form a stable meniscus, however, in this work an electrospun nanofibre nib was used. This has the advantage of providing suitable back pressure against the hydraulic head whilst minimising diffusion resistance. This is exemplified by a 34% increase in the current density (from 480 $mA.cm^{-2}$ to 640 $mA.cm^{-2}$) when depositing copper at 5 V vs Cu with a 1 M copper sulphate solution. The position of the deposition is controlled by the movement of the printing head.

After the copper layer was deposited, the copper electrolyte was removed and a nickel layer was deposited on top of this as illustrated in Figure 5.1b. Here the set-up was the same but with nickel counter and reference electrodes, as well as a nickel-based electrolyte. A potentiostat then applied a constant potential again to reduce the Ni^{2+} ions in the electrolyte to metallic nickel on top of the deposited copper layer. The print head then moves on the path defined, depositing nickel where the meniscus bridge and potential is applied, with repeated passes increasing the layer thickness. The use of the nanofibre nib over the sponge approach was highlighted by a current density increase of 85% (from 100 $mA.cm^{-2}$ to 190 $mA.cm^{-2}$) at a deposition potential of 2 V vs Ni.

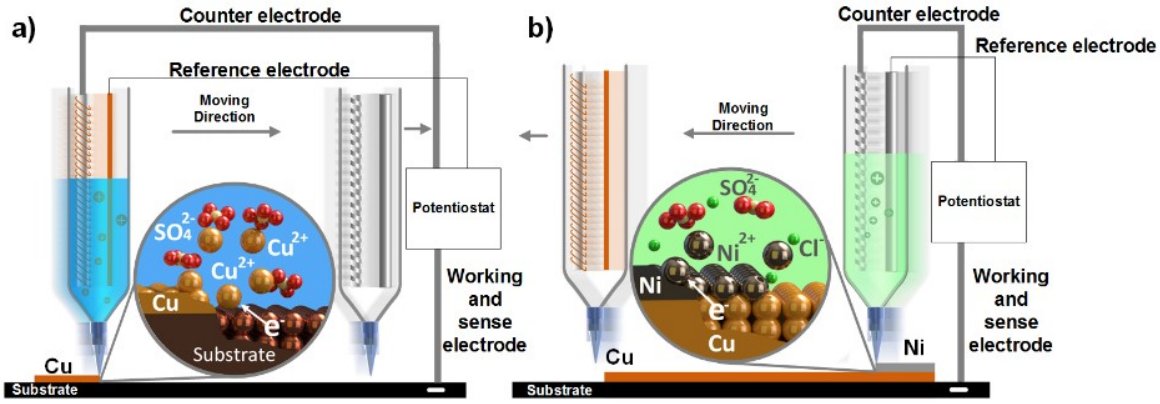

Figure 5.1 Schematic illustration of the multi-material 3D printing process. a) The meniscus confined copper electrodeposition process. b) The meniscus confined nickel electrodeposition process [228].

5.4 Material preparation and assessment methods

5.4.1 Nickel and copper electrolyte preparation

Nickel deposition electrolytes were made through a mixture of $NiSO_4 \cdot 6H_2O$ 113 $g.L^{-1}$, $NiCl_2 \cdot 6H_2O$ 30 $g.L^{-1}$ and H_3BO_3 23 $g.L^{-1}$. 1M copper sulphate electrolytes were prepared by mixing anhydrous copper (II) sulphate (12.5 g of $CuSO_4 \cdot 5H_2O$ (≥ 99.99% pure – Sigma Aldrich)) with 50 ml deionized water.

5.4.2 Scanning electron microscope

SEM imaging was performed using a Zeiss Auriga Crossbeam in backscattered mode with an acceleration voltage of 5 kV. Samples were mounted onto SEM sample stubs. No sputtering of the samples was performed. The Focussed ion beam was carried out to test the printed Cu-Ni bilayer strip surface morphology.

5.4.3 Conductivity test

All deposition experiments and electrical conductivity measurements used a Metrohm Autolab PGSTA302N with a 4-electrode configuration. Electrical conductivity measurements were made on the same potentiostat with a 4-electrode configuration to isolate contact resistances under potentiostatic conditions.

5.4.4 Energy-dispersive X-ray spectroscopy

EDS line scans and maps was carried out on a Zeiss of Auriga Cross Beam at 20 kV.

5.4.5 X-ray computed tomography

A nanotom® s (GE Sensing and Inspection Technologies GmbH, Wunstorf, Germany) was used for the XCT measurement. This was operated at an X-ray tube voltage and current of 80 kV and 225 µA respectively, with a tungsten-on-diamond target. The analysed samples were positioned between the X-ray source and detector to provide an effective pixel size of 0.9 µm. The 3D structures were reconstructed using 2,400 projection images captured over a 360° sample rotation and a cone-beam filtered back projection algorithm based on the Feldkamp-Davis-Kress (FDK) algorithm. Each projection image was acquired with an X-ray detector integration time of 2 s, with averaging and skip settings of 3 and 1 respectively, and an activated detector shift to minimise ring artefacts.

5.5 Assessment Results and Discussion

5.5.1 Morphological properties of Cu-Ni bimetallic and Cu-Ni-Cu trimetallic strips

Figure 5.2 shows optical images and SEM micrographs of the printed copper-nickel bimetallic strips at different deposition times as well as energy dispersive X-ray spectroscopy (EDS) line scans of the samples. In all cases, a lateral print head velocity of 0.4 $mm \cdot s^{-1}$ was used over a distance of 20 mm, with a 5 V vs Cu and 2 V vs Ni deposition potential for copper and nickel respectively. A base layer of copper was used in all cases with a 3-hour deposition time which produced samples with a thickness of approximately 45 μm after 216 passes which suggests a copper deposition layer resolution of approximately 200 nm. Figure 5.2 a)-c) shows the morphological changes of the bimetallic strip with a nickel deposition time of 1 hour, 3 hours and 5 hours with the same print head velocity. This therefore represents 72, 216 and 360 passes respectively with a nickel layer thickness of approximately 600 nm, 1 μm and 2 μm and thus a layer resolution of approximately 5-8 nm. The finer layer height resolution of the nickel compared to the copper is due to the lower reaction current density due to the lower deposition potential and also slower deposition kinetics of nickel relative to copper. In all cases it can be seen from the SEM and the EDS line scans that a tightly bound and clear interface between the nickel and copper is formed, with the both metallic layers showing a polycrystalline, often nanocrystalline and morphology. The lower magnification images also highlight that in all cases the printed strips exhibit a convex shape, which is consistent with the single copper dot results at higher potentials showing convex geometries, due to the higher reaction current density in the centre of the deposition nozzle. Figure 5.3 shows detailed SEM micrographic of trilayer strip, which grain size of copper is larger than nickel result in a finer nickel morphology. The elemental information of copper and nickel was confirmed through EDS mapping.

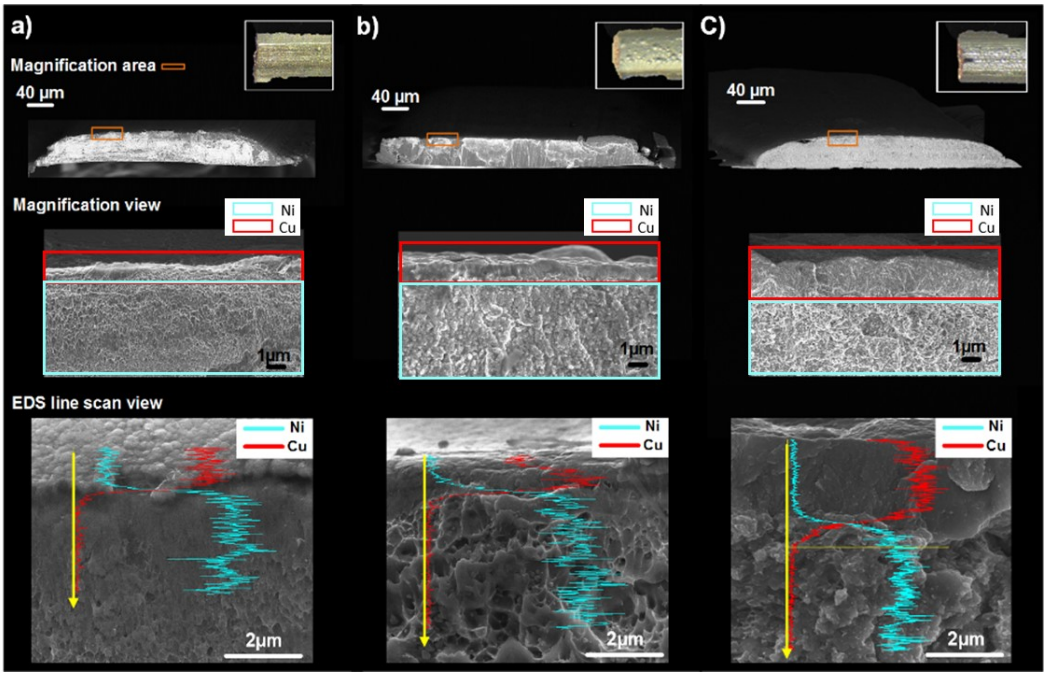

Figure 5.2 SEM cross-section and magnification view of bimetallic strip and optical top view of the bimetallic strip with the same 3hours copper deposition duration and different nickel deposition duration with a) 1 hour, b) 3 hours and c) 5 hours separately [228].

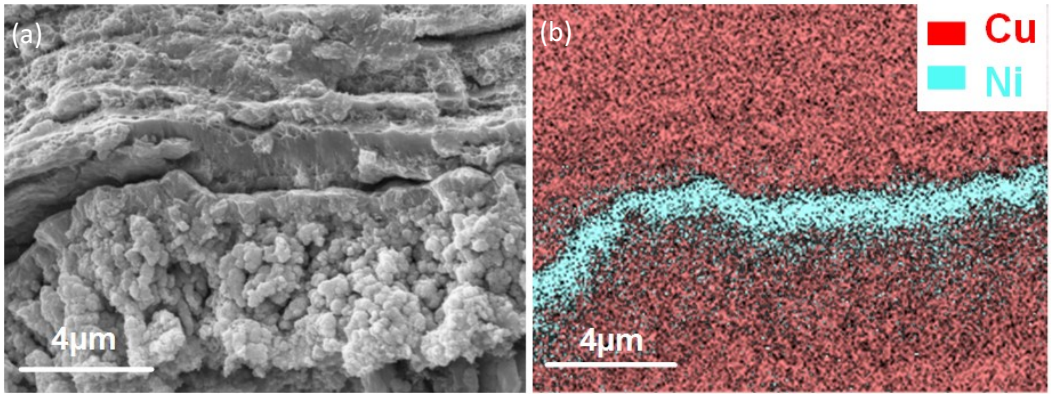

Figure 5.3 (a) SEM micrographs and b) EDS element mapping of Cu-Ni-Cu trilayer strips.

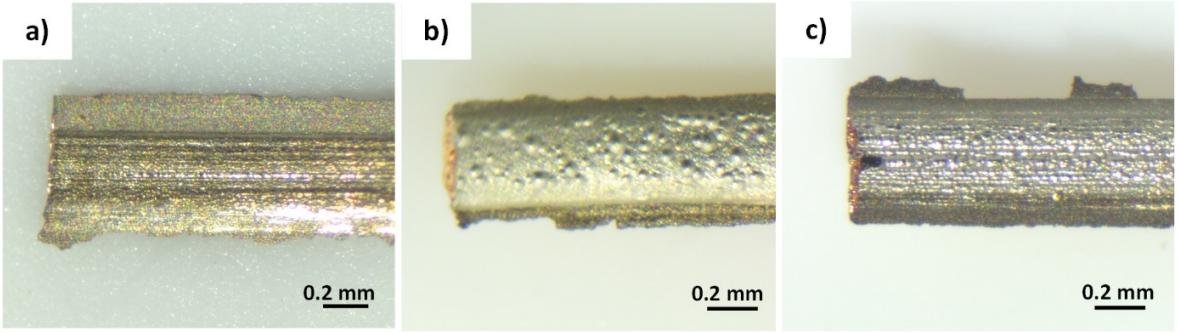

Figure 5.4 Optical images of the printed bimetallic strips with a 5 hours copper deposition and a) 1 hour, b) 3 hours and c) 5 hours nickel deposition.

5.5.2 Thermo-mechanical properties of Cu-Ni bimetallic strips

In order to investigate the thermo-mechanical properties of the printed bimetallic strips, samples were placed onto a heated bed with one end fixed and the other free to move. An

optical camera was placed over the samples to visualise the displacement as the temperature was increased from room temperature to 50 ˚C increments to 300 ˚C with images taken at each temperature once steady state conditions had been achieved. Figure 5.5 shows the deformation of the samples at different temperatures as well as with different copper-nickel layer configurations. It can be seen in all cases that as temperature is increased there is an observed mechanical deformation which is due to the difference in thermal expansion coefficient of copper (16×10^{-6} $^{\circ}C^{-1}$) and nickel (13×10^{-6} $^{\circ}C^{-1}$) [247]. Since the 2 metallic layers are tightly bound, a zero-displacement boundary condition at the interface is assumed and thus internal stresses are generated in the layers. In this system, since the copper thermal expansion coefficient is higher than that of the nickel there is an observed curvature with a tensile stress is generated on the copper side and a compressive stress on the nickel side. For a bimetallic strip consisting of 3 hours (~ 45 μm) copper and 5 hours (~2 μm) nickel deposition (Figure 5.5a), a maximum deformation of 40 ° was measured at 300 °C. Here the bimetallic strip was positioned perpendicular to the heating bed.

In Figure 5.5b, the nickel region was limited to a central region of 6 mm with the same deposition conditions. When heating the sample with the nickel side down, it can be seen that a curvature in the copper-nickel region can be observed. In the pure copper regions at the ends of the strips this remains parallel to the heating bed, due to the lack of bending stresses and the force of the nickel-copper region applying a slight pressure on the copper region against the heated bed.

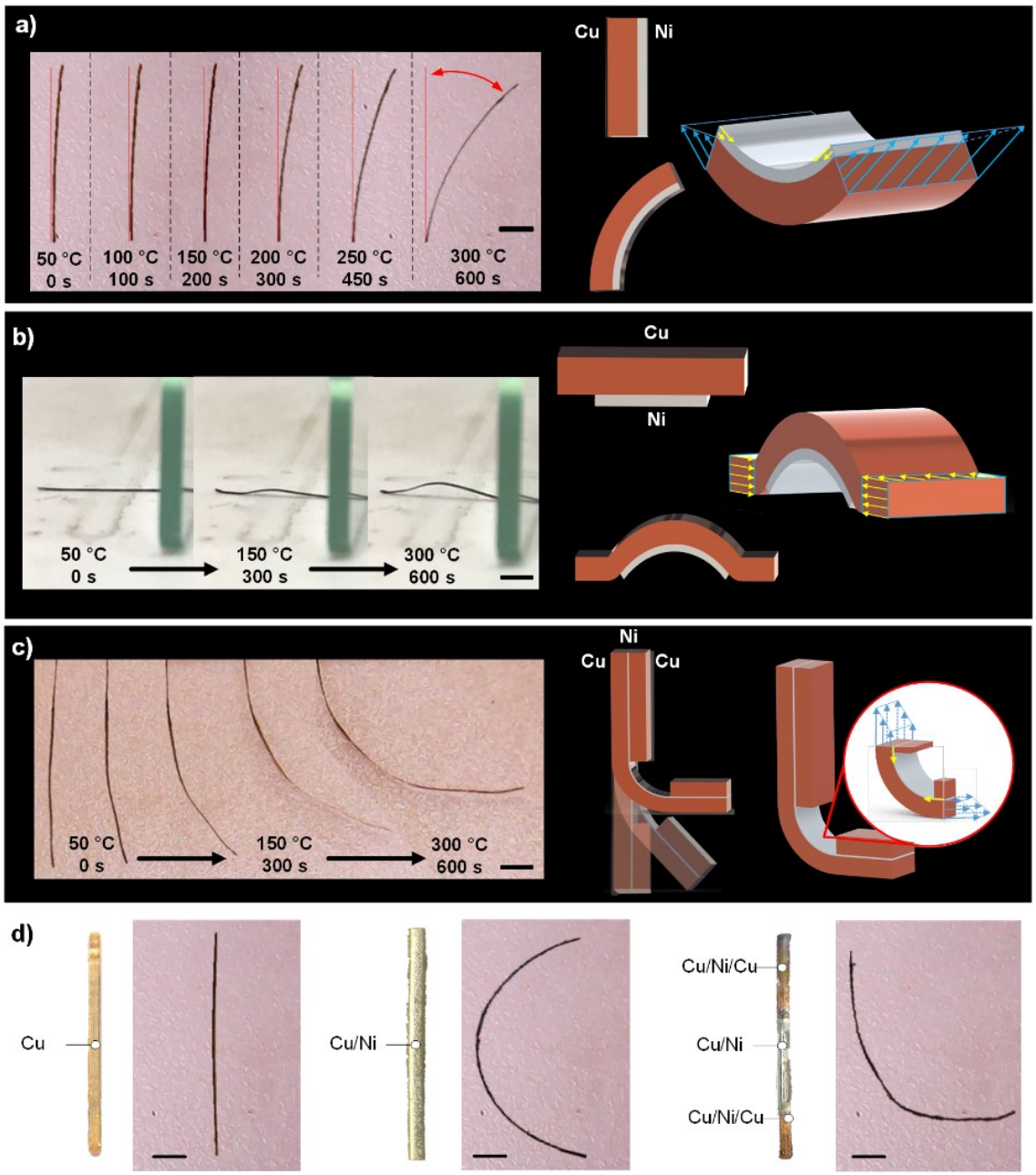

Figure 5.5 Thermo-mechanical response of Cu-Ni bilayer structures with a) perpendicular heating and b) selective nickel deposition in the centre of the strip and heating with the strip flat against the heating bed; c) Deformation of a Cu-Ni-Cu trilayer strip. d) Optical images of samples programmed to letters "ICL" at 300 °C. Scale bar: 2 mm [228].

In Figure 5.5c, a trilayer (Cu-Ni-Cu) configuration is shown which is similar to the configuration in Figure 5.4a but with an additional copper layer printed on top of the nickel layer with an 8 mm gap in the centre. In this configuration it can be seen that the addition of the top copper layer balances the thermal stresses in the Cu-Ni bilayer region and thus prevents bending which enables "L-shaped" geometries to be achieved and thus programmable combinations of linear and curved structures. Using a combination of these

designed structures, the letters “ICL” can be achieved after heating linear bimetallic sample to 300 °C (Figure 5.5d).

5.5.3 Bending angle and bending distance calculation

The deformation angle of the bended bilayer strips was measured by binarizing and fitting the acquired images to a circle to find the radius of curvature in MATLAB. The RGB images (Figure 5.6 a–d) of the bended bilayer strip were converted to a binary image in MATLAB. Each pixel in back colour of binary image is located by x and y coordinate. Then, the bilayer strip can be defined as a set of points with x and y coordinates. By using least squares method, the best fit circle and degrees of the curvature can be found according to the bilayer strip coordinates as shown in Figure 5.6e.

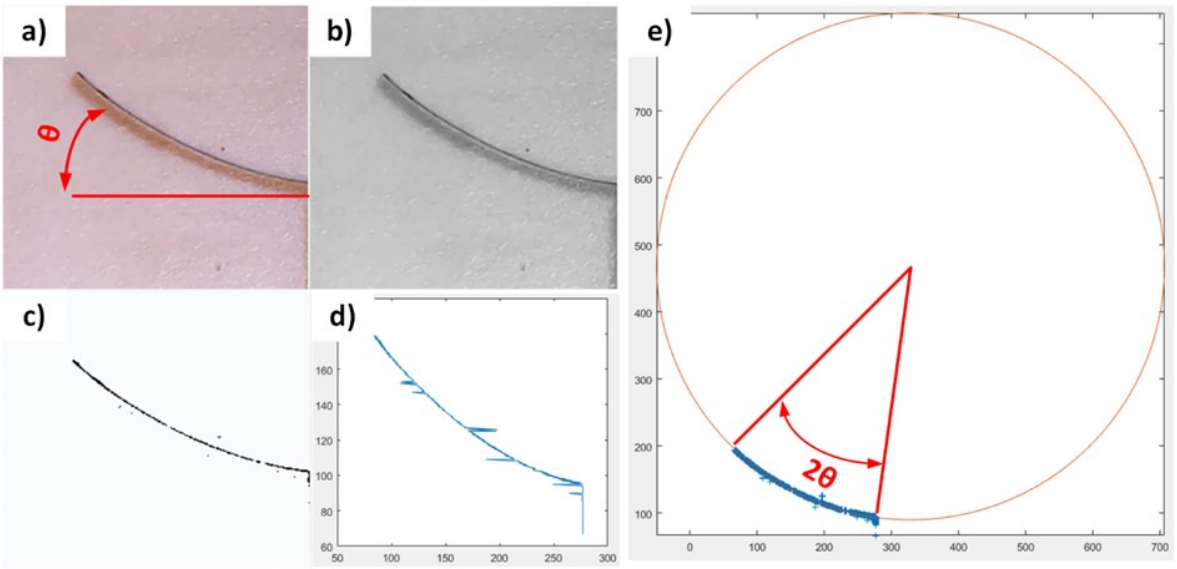

Figure 5.6 Calculation the bending angle of bilayer strip under MATLAB environment a) RGB image of Cu-Ni bilayer strip; b)-c) Binary images of Cu-Ni bilayer strip; d) Reversed Cu-Ni strip under MATLAB environment; e) Curve fitting of Cu-Ni strip

Figure 5.7 shows the Curve fitting of Cu-Ni bilayer strip under MATLAB environment at different activation temperatures from 50 °C, 150 °C and 300 °C. The maximum bending angle of figure 5.7a presents nickel layer deposition time of 1h is 26° at the temperature of 300 °C. The maximum bending angle of figure 5.7b presents nickel layer deposition time of 3h is 39° at the temperature of 300 ^{0}C. The maximum bending angle of figure 5.7c presents nickel layer deposition time of 5h is 41° at the temperature of 300 °C.

The bending angle of the trilayer strip can be calculated using least square programming, as well as the radius of best circle. And the bending distance can be deduced from the geometry calculations of best circle (Equation 5.1):

$$D = 2r \times (\sin\theta)^2 \quad (5.1)$$

Where D represents bending displacement (mm), r is the radius of best circle (mm), θ is the bending angle.

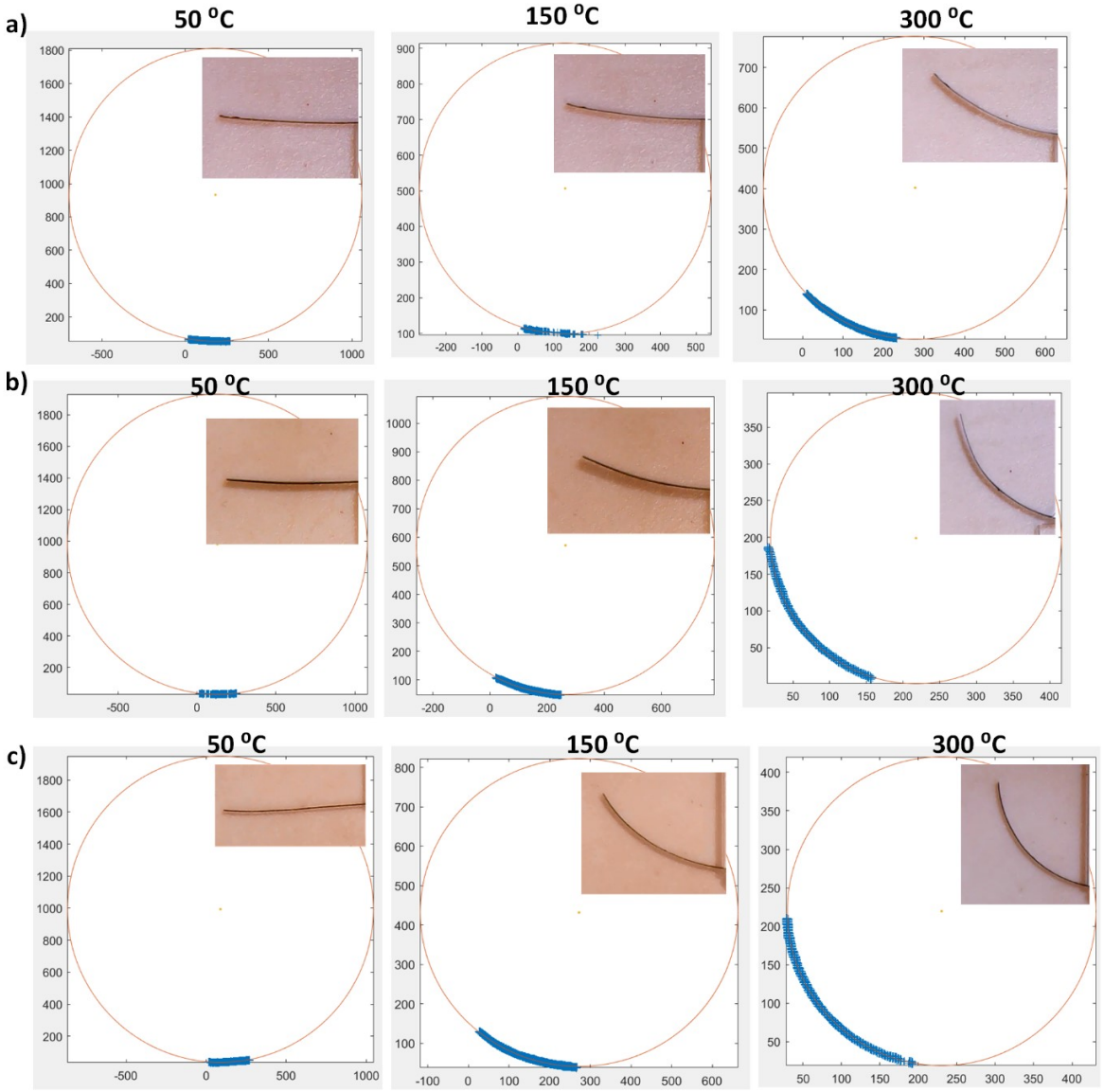

Figure 5.7 Curve fitting of Cu-Ni bilayer strips with 5 hours deposition of Cu and a)1 hour deposition of Ni; b) 3 hours deposition of Ni and c) 5 hours deposition of Ni under MATLAB environment at different activation temperatures of 50 ºC, 150 ºC and 300 ºC

5.5.4 Effects of design variables on the radius of curvature of the strips

Key design variables that affect the radius of curvature (κ) of the bimetallic strips include: the layer thicknesses, Young's modulus and thermal expansion coefficient of the 2 layers as highlighted in Equation 5.2 by Clyne and Gill [248]. Here E_x, h_x and α_x are the Young's modulus, thickness and thermal expansion coefficients of material x respectively, and ΔT

represents the temperature difference between the reference temperature at zero strain and the operating temperature.

$$\kappa = \frac{6E_1E_2(h_1+h_2)h_1h_2(\alpha_1-\alpha_2)\Delta T}{E_1^2h_1^4+4E_1E_2h_1^3h_2+6E_1E_2h_1^2h_2^2+4E_1E_2h_2^3h_1+E_2^2h_2^4} \quad (5.2)$$

Figure 5.8a, shows the bending angle of 20 mm Cu-Ni bimetallic strips with a base copper layer (5 V vs Cu, 3 hours) and nickel layers with different thicknesses (2 V vs Ni for 1 hour, 3 hours and 5 hours) over a temperature range from room temperature to 300 °C. It can be seen that as the thickness of the nickel layer and temperature difference increases, the bending angle also increases non-linearly. When comparing this with the theoretical deflections based on Equation (5.2) (Figure 5.8b), it can be seen that the same trend is observed, however the trend is linear and the absolute deflection angles are less. This can be explained by the fact that the deflection angles are highly sensitive to the layer thicknesses which from the SEM images in Figure 5.2 is shown to vary due to the uneven current density in the deposition nozzle during printing causing the convex line cross section.

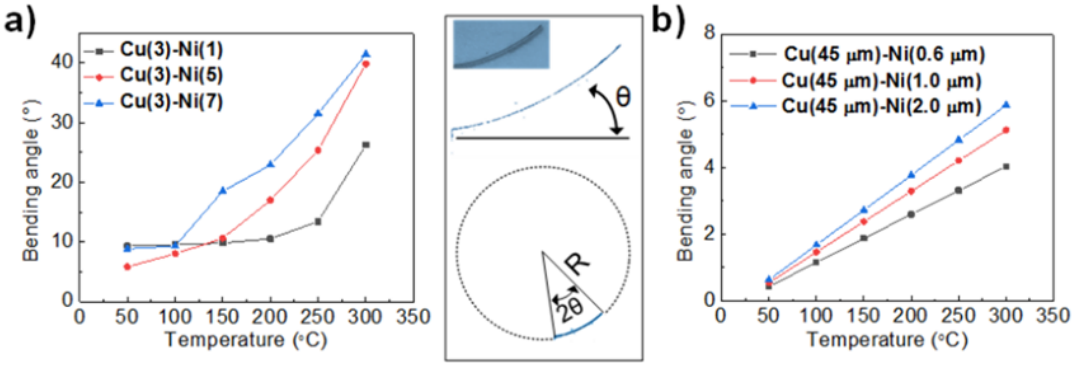

Figure 5.8 a) Measured bending angles for different Cu-Ni bimetallic strips at different temperatures. b) Theoretical bending angles of Cu-Ni bimetallic strips with idealised geometries [228].

To investigate the 3D morphology of the printed structures, XCT was used (Figure 5.9). Here it can be seen that the convex cross section is reasonably maintained along the length of the sample in the copper phase with slight plating at the edges of the sample. When increasing the nickel plating duration, it can be seen that nodules of nickel are formed on the surface and that the coating is not even over the copper. This likely leads to the non-linear temperature-deflection behaviour observed in Figure 5.8a.

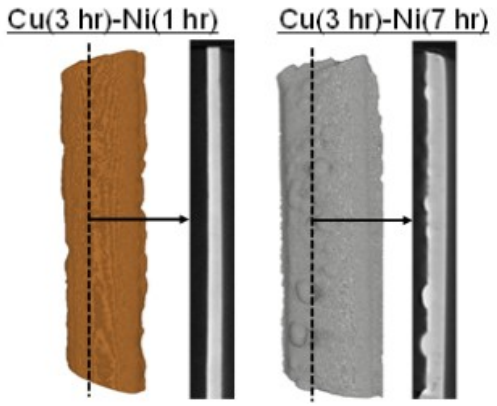

Figure 5.9 XCT reconstructions of Cu (3 hours)-Ni (1 hour) and Cu (3 hours)-Ni (7 hour) samples with reconstructed cross-section images [228].

As shown in Figure 5.5c, an "L-shaped" deflection can be achieved. The stress and bending displacement of the trilayer confirmation is analysed by finite element analysis (FEA) using Abaqus. The metallic beams are pinned at one end, where both displacement and rotation are set to zero. Figure 5.10 shows the simplified flat geometry, and each layer is tied together with no defects. The assembly is allowed to be deformed as the temperature is changed from the room temperature (25 °C) to the test temperature (50 °C to 300 °C). The thermal and mechanical properties of copper and nickel are specified in Table 5.1.

Table 5.1 Thermal and mechanical parameters of Cu and Ni [249, 250]

	Copper	**Nickel**
Thermal expansion coefficient	17.7 x 10^{-6} K^{-1}	12.9 x 10^{-6} K^{-1}
Young's Modulus	117 GPa	220 GPa
Poissons ratio	0.33	0.31
Density	8.96 gcm^{-3}	8.908 gcm^{-3}
Ultimate tensile strength	220 MPa	345 MPa
Thermal conductivity	385 $Wm^{-1}K^{-1}$	90 $Wm^{-1}K^{-1}$
Output	Copper	Nickel
Plastic strain	0.05	0.05

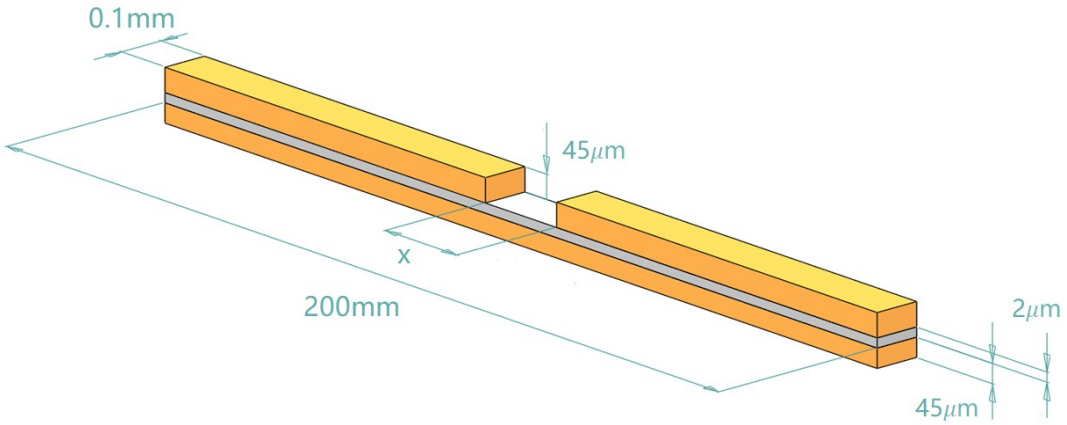

Figure 5.10 Idealised geometry boundary conditions of the trilayer Cu-Ni-Cu strip model.

Using the idealised geometry (flat and homogeneous materials) for FEA simulation, a systematic study of the trilayer strip deformation with varying gap width from 2mm to 6 mm is presented in Figure 5.11a. It can be seen that the displacement of the trilayer strip increases accordingly to the increase of the gap width. Figure 5.11b shows the validated FEA simulation with the gap width of 6 mm, which achieves the displacement as large as 9.47 mm.

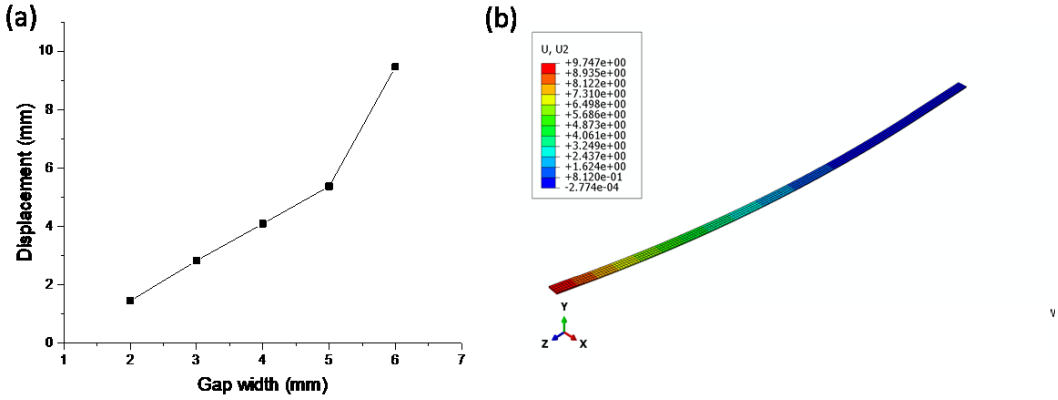

Figure 5.11 (a) The FEA simulation results of the displacement with varying gap width from 2 mm to 6mm in the trilayer strips; (b) the validated FEA simulation with the gap width of 6mm.

In comparison, experiments were conducted by measuring the displacement of the trilayer strips with different gap width of 2 mm, 4 mm, 6 mm and 8 mm. Figure 5.12 shows a linear increasing trend while enlarging gap width, indicating how this deflection can be controlled by changing the width between the Cu-Ni-Cu trilayers, with the deflection increasing as the gap distance increasing due to the larger region of exposed Cu-Ni.

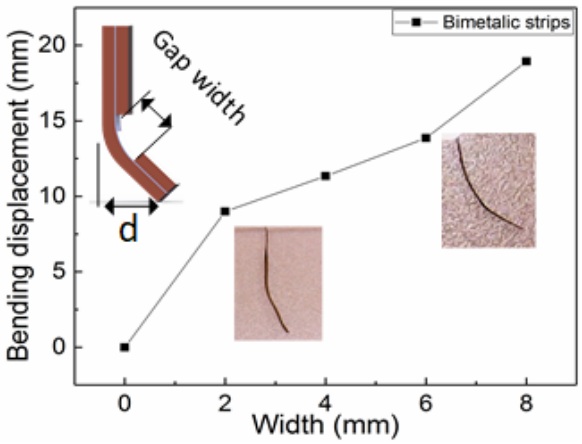

Figure 5.12 Displacement measurements of trilayer strips with varying gap.

This trend aligns well with FEA simulation results. However, the absolute deformation value of FEA simulation and ECAM experiment results is different. This is likely due to reasons as summarized in below:

- The geometric size and morphology of printed tri-layer strip is different from the input value in FEA simulation. As discussed in section 5.5.1, the printed bilayer and tri-layer strip exhibit a convex structure. However, this value was set as completely flat and unformal in FEA simulation.
- A simplified model was used at the interface where two metals were assumed to be tied firmly with no defects. For instance, the ECAM deposited nickel exhibits an uneven (Figure 5.9 XCT image) structure. Although the thickness of nickel layer was assumed 2 μm in FEA simulation, it is even thicker as a result of the geometry uncertainty. Thus, more bending force is generated at copper-nickel layer leads to a higher deformation which was underestimated in FEA simulation.
- The Young's Modulus, expansion efficient, Poisson's ratio of the ECAM fabricated strip can also be very different to the theoretical property of pure metals.

In summary, this part of the experiment verified the feasibility of using the finite element method to predict the deformation trend of 4D printed bimetallic strips. More accurate results can be obtained after further corrections based on the measurement results of the relevant properties of the printed metal strips.

Actuation of these printed bimetallic structures can also be achieved through ohmic heating since they are metallic. Figure 5.13 shows the electrical conductivity of the bimetallic strips, whereby all samples have a copper base layer fabricated with 5 hours deposition and 5 V vs. Cu potential but varying nickel deposition times ranging from 1 hr to 9 hours (2 V vs. Ni).

From the SEM images, the nickel structure was polycrystalline with nano-sized grains. Thus, it is expected that the resistivity will be higher than course grained nickel as a result of electron scattering at grain boundaries [251]. The electrical conductivity of all bimetallic samples were found varying between 1.4×10^6 S m^{-1} and 5.5×10^6 S m^{-1} which was slightly lower than the electrical conductivity of the copper single line (6.86×10^6 S m^{-1}) reported earlier [92] but is broadly in line with the conductivity of nanocrystalline copper reported by Lu *et al.* [235] 5.4×10^6 S m^{-1}. This is likely due to the lower electrical conductivity of nanocrystalline nickel (8.2×10^6 S m^{-1}) [252] compared to copper. Thus, as the deposition time of nickel increases, the electrical conductivity converges to that of nickel.

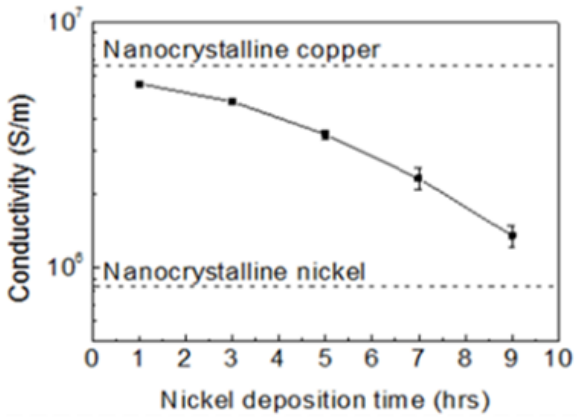

Figure 5.13 Electrical conductivity measurements of the bimetallic strips.

5.5.5 Validation of the bimetallic strips for circuit switch

Finally, to demonstrate the application of the printed bimetallic strips in high temperature environments, a simple circuit was built as shown in Figure 5.14. As the temperature increased to 300 °C, the Cu-Ni bimetallic strip bent and closed the circuit to power the LED. This highlights the potential application of this technique in fabricating structures that can sense the environment, thus opening the possibility for smarter 3D printed structures.

Figure 5.14 Schematic and photos of a simple electrical circuit actuated by the printed bimetalic strip.

5.6 Conclusions

In summary, a novel electrochemical 3D printer with 2 deposition nozzles was presented which is capable of printing temperature responsible multi-metal (copper and nickel) 4D structures. An electrospun nanofibre nib was used to provide sufficient back pressure to the hydraulic head exerted by the electrolyte, replacing the porous sponge material used in prior works by Chen *et al.* [92]. This new nib showed that it was capable of providing sufficient back pressure but with lower mass transport losses. SEM imaging and EDS analysis showed that a tightly bound interface is formed between the copper and nickel layers, with printed lines exhibiting a convex cross section due to the higher reaction current density at the centre of the nozzle. Optical microscopy during heating of various printed samples including Cu-Ni and Cu-Ni-Cu structures demonstrated the ability of the technique in creating different movements. This was highlighted through the creation of structures such as the letters “ICL” and a simple temperature sensing circuit. Design variables that were investigated included the layer thicknesses and geometric arrangement of the different layers. It was shown that, for a constant copper base layer, the deflection of the bimetallic strip increased with increasing nickel layer thickness due to the different in thermal expansion coefficients of the 2 materials resulting in internal stresses in the printed structure. When comparing measured results with the analytical solution, differences were observed which has been attributed to the uneven deposition of nickel onto the copper which is confirmed by XCT analysis. The findings here thus present the first reported multi-metal 3D printing approach for creating high temperature 4D structures which opens the possibility for creating more intelligent structures and sensors.

Chapter 6 Fabrication of an integrated copper-fibre supercapacitor via a desktop electrochemical 3D printer

This chapter presents content on the application of the electrochemical 3D printer towards electrochemical devices and some of the content has been published in a journal paper: Chen, X., Liu, X., Ouyang, M., Song, B., Childs P., Brandon N.P., Wu B., 2019. Fabrication of an integrated copper-fibre supercapacitor via a desktop electrochemical 3D printer. *Journal of Energy Storage,* 26, p.100993. As the first author of this publication, I led most of the tasks, including the copper-fibre supercapacitor fabrication, data collection, data analysis, drafting the article. The co-authors supervised and co-supervised the work, contributing to electrospinning of the fibres, critical revision of the article and final approval of the version published.

6.1 Introduction

Supercapacitors, also known as electrochemical double-layer capacitors, are energy storage devices which typically offer higher power densities and lifetimes than lithium-ion batteries over a wide temperature range [253-255]. Different from lithium-ion batteries, supercapacitors do not have charge transfer processes and changes in the structures, and instead charge through a double layer formed at the interface between a porous electronically conductive electrode and an ionically conductive electrolyte, enabling outstanding electrochemical performance in terms of high power density and long life-cycle in energy storage devices. For example, a development in supercapacitor for the application of automotive to reduce the detrimental load cycling by the combination with hydrogen fuel cells [256]. A typical supercapacitor is composed of high surface area electrodes, a porous separator and an electrolyte. Two modes of energy storage are combined in electrochemical

capacitors: electrochemical double-layer capacitors (EDLCs) and electrochemical pseudocapacitors [257].

- EDLCs use helmholtz double layer at the interface between the surface charges and ions of opposite charge to achieve higher electrostatic double-layer capacitance.
- Electrochemical pseudocapacitors achieve quick faradiaic charge transfer reactions between the electrode and electrolyte in sub-surface regions of active material.

Due to these significant advantages of supercapacitors, electrochemical energy storage devices (EESDs) have been applied in industrial applications [258] requiring high power density. AM techniques have drawn much attention as novel methods in fabricating EESDs. It is a simple process of fabricating electrode, modifying the electrolyte and assembling device of supercapacitor through sequential deposition of material in layers. The advantages over conventional techniques include the fact that the capability of fabricating complex 3D electrode architectures [259], a wide range of materials and alloys can be deposited with relatively low cost [92], and fully utilizing limited space to increase the surface area of electrode and facilitated ionic transport to potentially boost the energy density [260, 261].

A wide range of materials have been used for active electrode, such as carbon nanotubes (CNT), carbon nanofibres (CNFs), graphene oxide (GO) and carbon spheres [262]. SNFs show excellent flexibility, outstanding surface area and facile fabrication routes [263]. In terms of flexibility, the electrode can be reversibly folded up to 180° due to the continuous nature of the fibres, which is suitable for wearable devices. Polyacrylonitrile (PAN) is a precursor polymer for CNFs, presenting a typical performance varying from 100 F/g to 250 F/g [264] when used in a supercapacitor, affected by factors such as the heat treatment process and surface treatments. By adding metal oxides to the CNFs during the electrospinning process, the pseudocapacitive behaviour can be enhanced and improve the charge storage capabilities. For instance, Liu *et al.* [265] presented an all-fibre flexible electrospun supercapacitor by creating a precursor solution combining manganese acetylacetonate (MnACAC), PAN and dimethylformamide (DMF). The MnACAC was decomposed into MnO after heat treatment which decreased the electronic conductivity and increased the specific capacitance (90 F/g to 200 F/g @2.5 mV/s). This is due to the fast-redox reactions associated with the addition of the MnO. In addition, uncarbonised PAN nanofibres were used as the separator in this design, enabling a 40% improvement in performance compared with a commercial Celgard separator. The ionic diffusion resistance can be dramatically reduced by using a good separator, featuring high porosity, low through-

plane tortuosity and thin thickness [266]. And the inherent properties of electrospun structures highlights versatility of CNFs [256].

Fibre-based structures have been developed. Yang *et al.* [267] presented a method of dip coating elastic fibres in a H_3PO_4 - poly (vinyl alcohol) (PVA) gel electrolyte combined with a carbon nanotube sheet wrap to create highly flexible supercapacitors. This study featured a high degree of flexibility, but a limited surface area resulting in a low specific capacitance of 19.2 F/g and noticeable capacitance loss after 800 charge/discharge cycles. Other approaches to produce supercapacitors include roll-to-roll printing [268], screen printing [269], laser scribe burning [270], dipping and drying techniques [271], spraying and masking [272].

Additive manufacturing techniques have been used to fabricate energy storage devices, focusing on the optimization of mass transport properties via the creation of structured electrodes [190, 273, 274]. Similarly, electrospun nanofibre electrodes have been developed for supercapacitors with relatively high surface area produced via the spinning process and the flexible nature of the material. However, pure carbon-based materials present limitations in the specific capacitance, focusing on electrochemical enhancement of the material with metal oxides, such as manganese oxides, which endows pseudocapacitive behaviour [256].

In this chapter, we demonstrate a combined manufacturing method via electrochemical 3D printing and electrospinning to produce a novel copper-nanofibre supercapacitor, and how electrochemical 3D printing of copper onto composite MnO-electrospun nanofibres can enhance performance through a well-adhered integrated current collector onto the electrospun fibres. The presented hybrid capacitor uses the nanoporous carbon framework as the supercapacitor, and the MnO as the pseudocapacitance. To date, there have been no reports of combining electrospun nanofibres with electrochemical 3D printing to create integrated current collectors and as a means of enhancing electrical conductivity of the electrode. This therefore opens new possibilities in the field of additive manufacturing applied to electrochemical devices. This chapter therefore contains the following sections:

- **Fabrication strategy for copper-fibre supercapacitor**

  The copper-fibre supercapacitor is fabricated with an electrospinning equipment and a desktop electrochemical metal 3D printer. The material preparation, operation parameters and fabrication steps for printing copper-fibre supercapacitors are detailed in this section.

- **Assessment methods**

  This section outlines the assessment methods for the obtained copper-fibre supercapacitor as the application of the electrochemical 3D printer. Wettability and electrochemical assessments are presented.

- **Assessment results and discussion**

  This section presents the assessment results to explore the improvement of the conductivity of the integrated copper-fibre electrode and current collector, as well as the enhanced performance of capacitor.

6.2 Fabrication strategy for copper-fibre supercapacitor

6.2.1 The fibre electrodes preparation

The electrospinning precursor was prepared by adding 1g of PAN powder (Goodfellow Cambridge Limited Huntingdon, mean particle size 50 μm, and mean molecular weight 230,000 g mol^{-1}) into 10 mL dimethylformamide (DMF, VWR chemicals, 99.90%). To prepare a high mass loading 30 wt.% MnACAC precursor, 0.4285 g MnACAC powder (Merck Schuchardt OHG, ≥98%) was dissolved in the mixed solution of PAN and DMF by stirring at 50 °C for 12 hours.

A 10 mL polypropylene dispensing syringe (Metcal-7100LL1NPK) equipped with a 13mm length flat-tipped needle (0.41mm inside diameter, 0.71mm outside diameter) was filled with prepared precursor for electrospinning. Figure 6.1a shows the schematic setup for electrospinning process, where a distance of 175 mm was held between the needle and the polished aluminium collector plate (200 mm × 200 mm), with the prepared precursor dispensing though the needle at a speed of 0.75 mL/h by a syringe pump (Graesby 3300) under 12 kV high voltages (GenVolt 73,030). After 1 h electrospinning at room temperature (25 °C, 50% humidity), the fabricated thin and free standing nanofibre were removed from the plate. For the further use of preparing nanofibre electrodes, the obtained PAN-30 wt.% MnACAC nanofibre film was pre-carbonized at 280 °C in ambient air condition (initial ramp rate 1°C min^{-1} to 280°C, dwell time of 2h), and then heating in the nitrogen gas environment for fully carbonisation at 850 °C (initial ramp rate 2 °C min^{-1}, dwell time of 0.5 h at 550 °C, ramp rate of 3 °C min^{-1} to 850 °C, dwell time 2 h). The PAN nanofiber film with 30 wt.% MnACAC after carbonisation (30 Mn@CNF) was cut into a circular mat shape using a punch tool with diameter of 16 mm. The mass of circular mat was then weight ranging from 1.1 mg to 1.5 mg. An optical top view of the 30 Mn@CNF electrode is shown in Figure 6.2a.

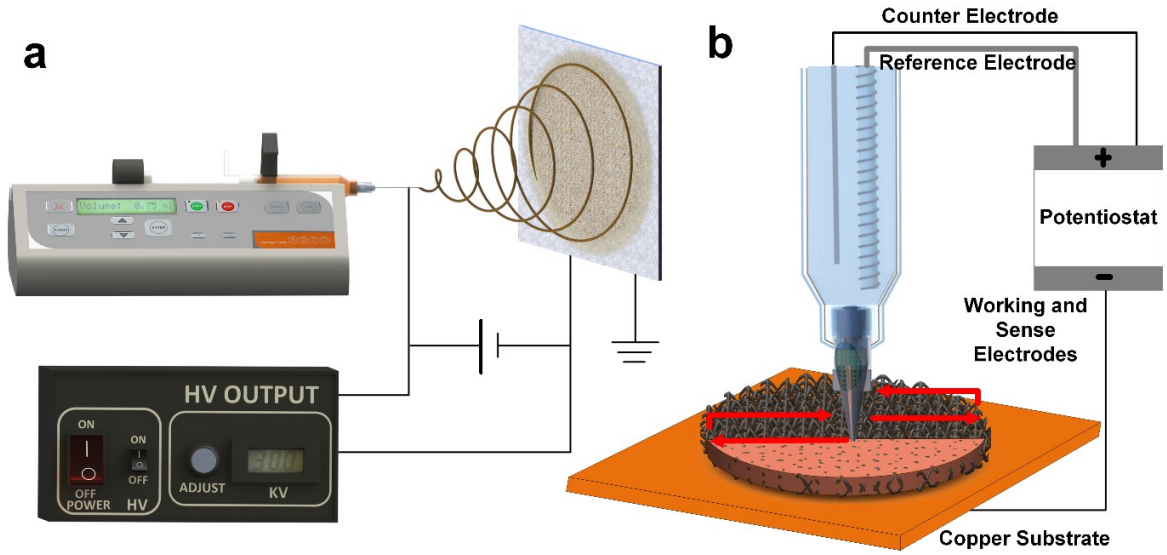

Figure 6.1 Illustration of the synthesis of a) nanofibre electrospinning and b) electrochemical 3D printing [256].

6.2.2 The copper-fibre electrodes preparation

To achieve the copper-fibre electrodes, the 30 Mn@CNF fibre mat was placed onto a copper substrate for electrochemical 3D printing of copper. The setup is shown in Figure 1b**,** which is a schematic of copper deposition process using a 10 mL polypropylene syringe (Metcal-7100LL1NPK) equipped with a 400 μm polypropylene nozzle (Metcal- 922125-DHUV). The copper is deposited and coated via the previous developed low-cost desktop electrochemical 3D printer. The x, y and z-axis movements are enabled by stepper motors, where the deposition unit moves in x and y directions with the platform moving in z direction. Copper sulphate electrolytes were prepared by mixing anhydrous copper (II) sulphate (≥99.99 % pure Sigma – Aldrich) with deionized water. For the copper sulphate syringe assembly, two copper wires were inserted into the electrolyte, acting as a counter electrode and a reference electrode, respectively. Working and sense probes of potentiostat were connected to the copper platform where the deposition occurred. The printed copper coating around 30 Mn@NCF fibre is obtained by moving the deposition unit in a zigzag path with an interval width of 200 μm at a potential of 5V versus Cu for a duration of 3 hours. Figure 6.2b presents an optical top view of fabricated copper-fibre electrode serving as both active electrode and current collector.

6.2.3 The integrated copper-fibre supercapacitor preparation

The integrated copper-fibre supercapacitor was assessed in a split flat cell (MTI Coporation) and equipped by mounting the cut copper-fibre mats with round shape (16mm diameter) in the cell. The sandwich shape fibre supercapacitor was composited of one integrated copper-

fibre component worked as both positive electrode and current collector and one integrated copper-fibre component worked as both negative electrode and current collector separating by a PAN nanofibre. 0.25 M aqueous bis(trifluoromethane)sulfonimide lithium (LiTFSI, Sigma Aldrich, purity≥99.0 %) was used as electrolyte.

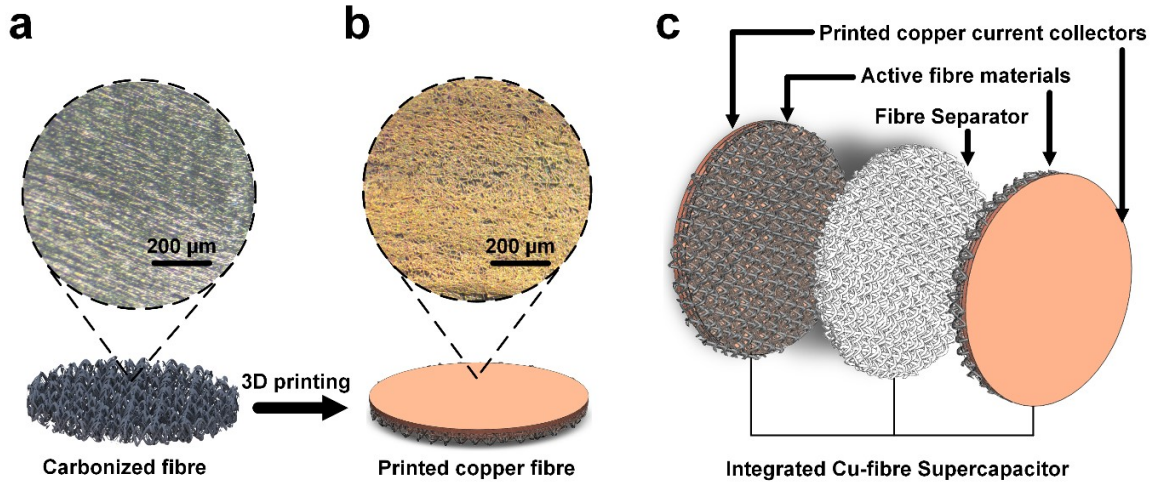

Figure 6.2 Schematic illustrations of a) carbonized PAN-30% MnACAC nanofibre film, b) electrochemical 3D printed copper at a potential 5 V versus Cu with a duration of 3 hours and c) A Cu-fibre supercapacitor with the printed Cu-30Mn@CNFs acting as both electrodes and current collectors separating by PAN-nanofibre separator [256].

6.3 Assessment methods

6.3.1 Imaging and materials analysis

Scanning electron microscopy (SEM) was presented by applying a LEO Gemini 1525 (Zeiss) Auriga Crossbeam operated at an acceleration voltage of 5 kV with no simple sputtering. All the imaged samples were coated with a 10nm layer of Chromium.

6.3.2 Wettability

Water contact angle measurements on the surfaces of the carbonized 30 Mn@CNF fibre mat were carried out with a KSV CAM 200 system (KSV Instruments, Finland). The system is equipped with a CCD video camera and a micrometric liquid dispenser to drop 2µl of distilled water on the surface of the mat. The contact angle measurements were automatically calculated with the instrument software. The water droplet was deposited at the centre of the surface for each sample.

6.3.3 Electrochemical performance characterization

The electrical performance of an integrated copper-fibre supercapacitor with well flexing cell was tested through electrodes (20mm × 20mm). The EIS, cyclic voltammetry, and CP

were carried out using a Metrohm Autolab PGSTA302N in a two-electrode configuration. Electrical conductivity measurements were carried out on the same potentiostat with a 4-electrode configuration to isolate contact resistances under potentiostatic conditions.

6.4 Assessment results and discussion

The techniques used for manufacturing the integrated Cu-fibre supercapacitor are schematically presented in Figure 6.1, consisting of electrospinning (Figure 6.1a) and electrochemical 3D printing (Figure 6.1b) techniques. In a typical electrospinning process as shown in Figure 6.1a, the precursor was initially prepared and then electrospun to create naofibre composites of MnACAC and PAN. After pre-carbonization (280 ºC, air condition) and full-carbonization (850 ºC, N_2 atmosphere), the manganese salt (MnOx) was eventually reduced to MnO. According to the research of Liu *et al.* [265], the MnO can be found within the nanofibre in a low concentration of 10 wt.% MnACAC precursor and be observed both inside and outside of the nanofibre in a high concentration of 40 wt.%. Thus, the less conductive MnO nanoparticles reduced from high concentration of 30 wt.% MnACAC precursor are then believed to embed both inside and outside of the fibre. In a typical electrochemical printing strategy exhibited in Figure 1b, the electrolyte (1M $CuSO_4$) was dispensed through a meniscus-confined moving nozzle and the copper ions were reduced to pure copper governing by applied external potentials (5V vs Cu). As a result, the printed copper was deposited around the conductive fibres. Chen *et al.* (24) reported that the printed copper exhibited a highly polycrystalline nature with a good electrical conductivity as high as 6.86×10^6 S m^{-1}. Thus, it is expected to enhance electrical conductivity of high mass loading MnO electrodes via electrochemical 3D printing.

Figure 6.2 illustrates a 30 Mn@NCF fibre mat, a copper-fibre electrode and a sandwich type copper-fibre supercapacitor. As seen in Figure 6.2a, the enlarged optical top view of 30 Mn@NCF fibres exhibit a random orientation due to the influence of gravity [265]. With the obtained 30 Mn@NCF nanofibre mat serving as the substrate, an electrochemical deposition process (potential of 5V, deposition velocity of 2 mm s^{-1}, duration of 3 hours) was conducted by the Desktop Electrochemical 3D Printer, resulting in a uniform distributed copper sheet embedded on the top of the mat as observed from Figure 6.2b. The entire piece is regarded as a Copper-fibre electrode. The configuration in Figure 6.2c shows a sandwich structure supercapacitor consisting a PAN fibre separator separating two integrated Copper-fibre electrodes assembled outside.

Figure 6.3 presents the water contact angle of 30 Mn@CNF fibre mats at the air-liquid-solid interface under room temperature and humidity of 50%. In Figure 6.3a, 1 µL deionized water with surface tension of 0.71 dyn cm^{-1} was dropped onto the 30 Mn@CNF fibre mat with an average thickness of 55 µm [275]. The static water contact angle was then measured through surface contact angle tester. Figure 6.3b shows a water contact angle of 131º for a 30 Mn@CNF mat with 290 ºC pre-carbonized temperature and 2h dwell time at 550 ºC. It indicates a highly hydrophobic surface character. Comparing with fibre mat in Figure 6.3b, a short dwell time of 0.5h at 550 ºC was applied during fibre carbonization in Figure 6.3c. As a result, a lower contact angle of 79º can be found, which shows a hydrophilic surface character. Feng *et al.* [276] reported that the surface wettability of nanofibre can be modified though either changing surface roughness or the density of fibre. Generally, higher surface roughness or lower nanofibre density is essential to the high-hydrophobicity. As opposite to the proposed theory, the annealing conditions in Figure 6.3c are likely to reduce the shrinkage of nanofibre diameter (reducing the interfiber distance) and to increase the nanofibre density. Thus, the surface wettability was modified from hydrophobicity (Figure 6.3b) to hydrophile (Figure 6.3c). Figure 6.3d exhibits a smallest contact angle of 46º for a 30 Mn@CNF mat with 280 ºC pre-carbonized temperature and 0.5h dwell time at 550 ºC. This high hydrophilic surface character is due to the use of ethanol after the nanofibre annealing process, which has improved the surface roughness. Figure 6.3e-h show the electrochemical deposition of copper printed onto 30 Mn@CNF fibre mats with different surface wettability corresponding to the Figure 6.3b-d respectively, but under the same deposition conditions (1M $CuSO_4$, 5V vs Cu, and 1-hour deposition time). The cross-section SEM configuration in Figure 6.3f demonstrates a distinct interface between the top layer of printed copper and inner layer of nanofibre. This is possibly due to the hydrophobic property of nanofibre. It prevents the electrolyte penetrating and further contacting with the nanofibre. In comparison, the hydrophilic property of nanofibre (Figure 6.3g) enables deposition of copper further along the fibre in z direction. However, the deposited copper becomes discontinuous and intermittent polycrystalline with nano-sized clusters along the nanofibre because less electrolyte is able to reach to the deeper end. The well-deposited copper can be seen on both top layer and inner layer of nanofibre (Figure 6.3h). It suggests that a high hydrophilic surface property of 30 Mn@CNF fibre mat enables a well-coated copper structure to be achieved easily.

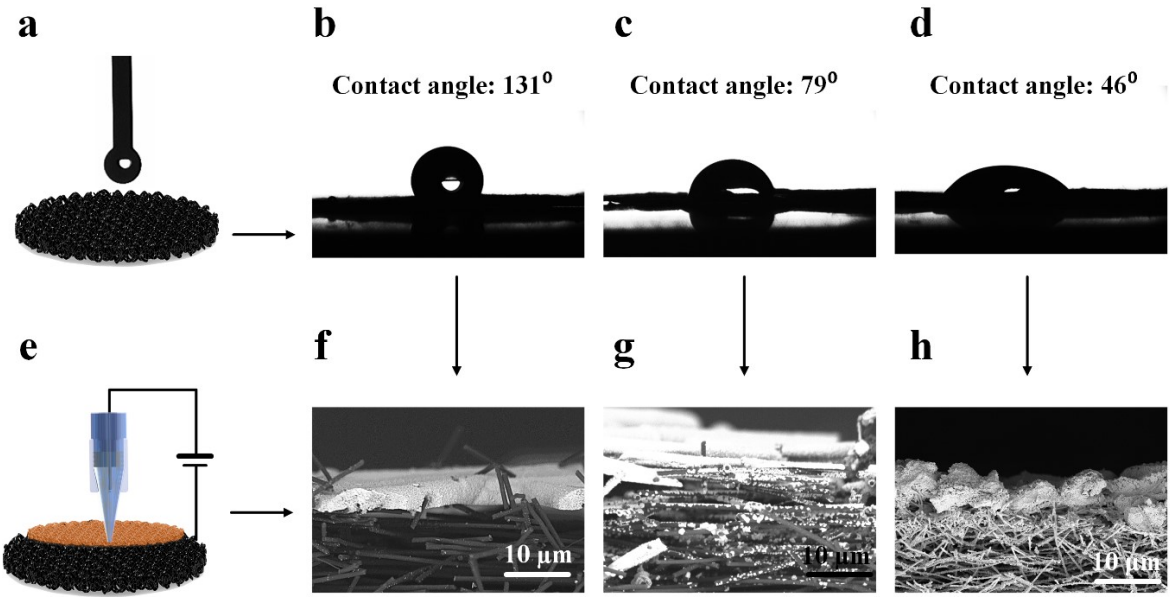

Figure 6.3 a) Water contact angle test of carbonized PAN-30% MnACAC fibre mat, for b) 290ºpre-carbonized temperature and 2h dwell time at 550º; c) 280ºpre-carbonized temperature and 0.5h dwell time at 550ºand d) using ethanol after annealing; e) Electrochemical 3D printing copper onto the nano fibre mat, the cross-section SEM image of printed copper onto f) highly hydrophobic; g) hydrophilic and h) highly hydrophilic 30 Mn@CNF fibre mats [256].

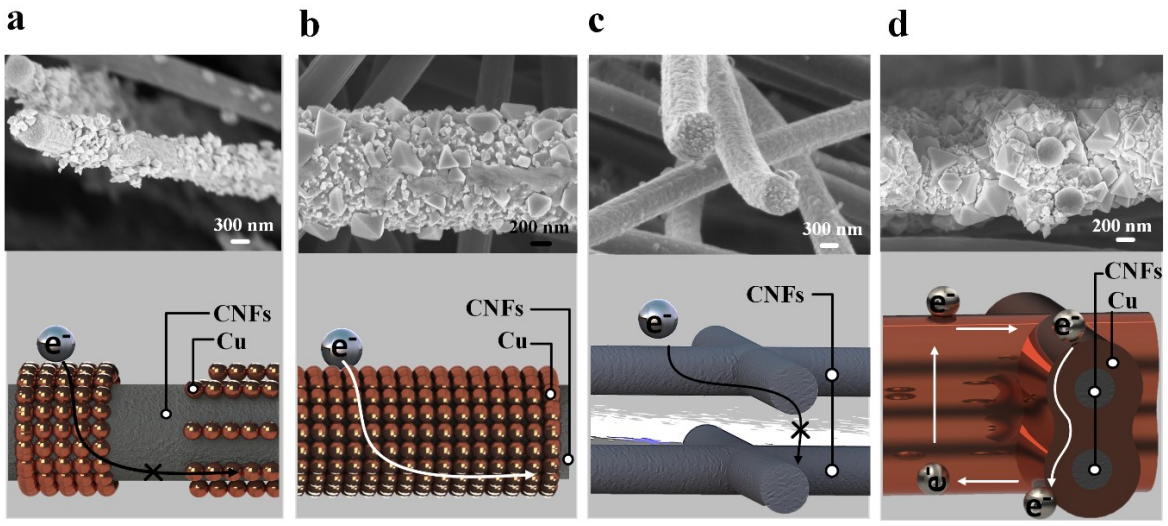

Figure 6.4 a) SEM image of a coated single 30 Mn@CNF fibre in a) one hour copper deposition with a diameter of 600 nm and b) three hours copper deposition with a diameter of 850 nm; SEM images of c) the highly hydrophobic and d) the highly hydrophilic multi-layers 30 Mn@CNF fibres in three hours copper deposition [256].

Figure 6.4a-b demonstrate electrochemical print copper onto the 30 Mn@CNF fibres with the same hydrophobic wettability and electrochemical deposition conditions (1 M $CuSO_4$, 5 V vs Cu), but in a different deposition time. After one-hour deposition, SEM image of Figure 6.4a shows a 280 nm diameter nanofibre is coated with discontinuous nano-sized copper as

a result of electron movement terminating at the grain boundary. In contrast, after three hours deposition, SEM image of Figure 6.4b shows a single nanofibre well coated with copper featuring nanocrastline nature in a diameter of 610 nm. The electrical conductivity is expected to be enhanced due to the well-coated copper-fibre microstructure. As shown in Figure 6.3f, the nanofibre repels electrolyte as a result of the deposited copper can only be found on the top layer of nanofibre. To further investigate the inner structure of Figure 6.3f, the SEM image of Figure 6.4c highlights this hydrophobic structure after three hours deposition (1 M $CuSO_4$, 5 V vs Cu) via two nanofibres. In the configuration, two nanofibres separate from each other without depositing any copper, thereby hindering the electron transfer. In Figure 6.4d, the optimized hydrophilic surface character allow electrolyte to penetrate all nanofibre layers and to print a fully dense copper-fibre structure after three hours deposition (1 M $CuSO_4$, 5 V vs Cu). It can be observed from the SEM image that two highlighted nanofibres are well connect via coated copper. Thus, the electron transformation also benefits from this dense structure.

Figure 6.5a presents the cyclic voltammetry graph of the Copper-30 Mn@CNF supercapacitor at different scan rates of 5 mV s^{-1}, 10 mV s^{-1}, 25 mV s^{-1}, 50 mV s^{-1}, 75 mV s^{-1} and 100 mV s^{-1}. The stable CV curve implies a good performance of the assembled Cu-fibre supercapacitor. As the scan rate increases, the peak current is proportional to the scan rate, which is described by the Randles–Sevcik equation. In this situation, the electron transfer at the working electrode surface is fast and the current is limited by the diffusion of analyte species to the electrode surface. Comparison of specific capacitance (C_{sp}) at different scan rates with high mass loading of 30 Mn@CNF with varying copper deposition time from 1 hour to 3 hours is shown in Figure 6.5b. The results show that with an increase in the deposition time, better specific capacitance can be achieved. Figure 6.5c presents their C_{sp} values at the 5 mV s^{-1}. It can be seen from the result that the integrated copper-30 Mn@CNF devices can achieve a higher capacitive value than pure PAN-CNF, which reaches 125 F g^{-1} at copper deposition time of 1 hour. The three-hour copper and 30 Mn@CNF device exhibits a highest C_{sp} as 208 F g^{-1}, and two-hour device also reaches a high value of 187 F g^{-1}. The one-hour copper and 30 Mn@CNF devices also shows a higher capacitive value than zero-hour and 30 Mn@CNF device (91 F g^{-1}) and pure PAN-CNF (99 F g^{-1}), which reaches 122 F g^{-1}. The Figure 6.5e also demonstrates that the mean value of coated Cu-fibre diameter is proportional to the specific capacitance. After three hours deposition, the diameter of copper-fibre composite is 610 nm which is three times larger than that of pure 30 Mn@CNF fibre with 260 nm.

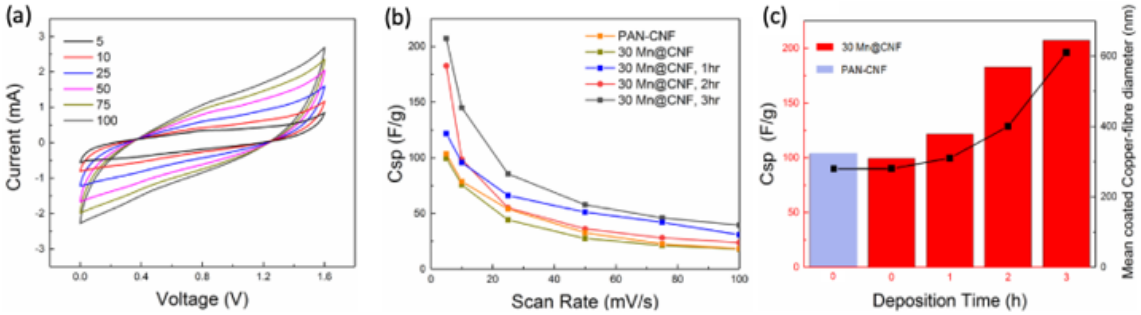

Figure 6.5 a) the CV curve of copper-30 Mn@CNF supercapacitor at different scan rate (5 mV s^{-1} , 10 mV s^{-1}, 25 mV s^{-1}, 50 mV s^{-1}, 75 mV s^{-1} and 100 mV s^{-1}); b) Specific capacitance of the copper-30 Mn@CNF supercapacitor as a function of scan rate with different copper deposition time (1-3 hours); c) Specific capacitance with different copper deposition time at scan rate of 5 mV s^{-1} and with the corresponding mean coated copper-fibre diameters [256].

As shown in Figure 6.6a, the Impedance Nyquist plots of three different copper and 30 Mn@CNF electrodes (1 hour, 2 hours and 3 hours) based supercapacitor present decreased resistance. The observed decreased charge transfer resistance and contact resistance are attributed to the increasing pseudocapacitive behaviour of the integrated supercapacitors due to the increase of copper deposition time. It can also be observed from Figure 6.6b that the conductivity of integrated copper-30 Mn@CNF electrodes is positively proportional to the copper printing time due to the good electrical conductivity of copper. The reduced resistance and increased electrical conductivity of integrated copper (3hours deposition)-30 Mn@CNF electrodes both contribute to the better specific capacitance as shown in Figure 6.5b. Therefore, an increasing copper deposition time not only attributes to create a denser and more continuous copper-fire structure of both the top layer and inner layer but helps of facilitating the electrical and ionic transport in the supercapacitor.

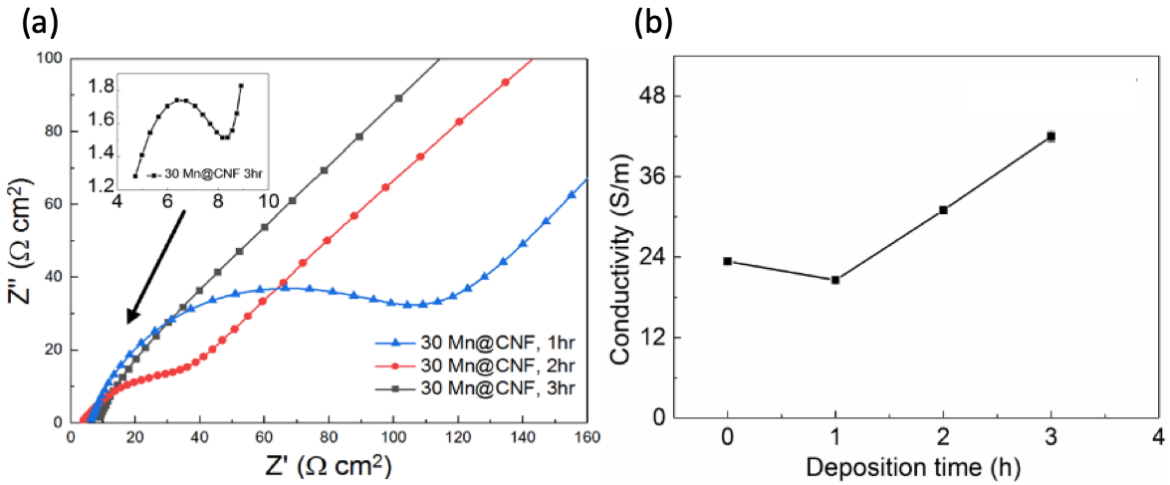

Figure 6.6 a) Impedance Nyquist plots of the copper and 30 Mn@CNF integrated electrodes with different copper deposition time in 1 hour, 2 hours and 3hours; b) The

conductivity of coated copper and 30 Mn@CNF film with different copper deposition time [256].

6.5 Conclusions

In summary, a novel manufacturing method of the electrochemical 3D printing combined with electrospining is proposed for preparing an integrated high mass loading copper and 30 Mn@CNF supercapacitor. It has been demonstrated that the specific capacitance of copper and 30 Mn@CNF supercapacitor fabricated using this combined techniques can be increased from 99 F g^{-1} to 208 F g^{-1} at 5 mV s^{-1}. The analysis of Impedance Nyquist plots and conductivity support the assumption that performance of supercapacitor can be improved via increasing the electrochemical deposition time of the copper, where the conductivity increases up to 46 S m^{-1} and contact resistance decreases down to 8 Ω cm^2 as a result. In order to achieve a dense and continuous copper-fibre structure, wettability of fibres is carefully controlled via decreasing dwell time to 0.5 h during carbonization and adding chemical, such as ethanol, after fibre carbonization. The hydrophilic surface wettability of electrospun high mass loading fibres with a contact angle of 46 °C present an outstanding ability in creating the dense and continuous copper-fibre structure. The finding here thus presents first reported electrochemical 3D printing and electrospinning approaches for building a high mass loading and high performance copper-fibre based supercapacitor which enables further possibility to create more integrated electrodes and eventually to enhance the performance of supercapacitor.

Chapter 7 Conclusions and future work

7.1 Conclusions

AM is being considered for industrial uptake in various fields due to the high design flexibility Metal-based AM techniques are often limited to high costs systems which can only print in single materials using inert gas environments and requiring high power lasers. ECAM is a relatively new form of metal AM which uses the localised electrochemical deposition of metal ions from electrolyte solutions to create metal structures. As an emerging technology, there are limitations to be solved. Current systems using ECAM methods (Localized Electrochemical Deposition (LED) and Meniscus Confined Electrochemical Deposition (MCED)) are not able to produce large-scale functional structures of complex geometries.

The aim of this work was to develop a low-cost electrochemical 3D printer for large-scale metal fabrication and validate the system by accessing the performance and properties of the fabricated metal structures. This thesis presents and discusses for the first time the use of large scale (400 μm nozzle) meniscus confined electrochemical printing. The achievement has been accomplished in four stages, which are: design and fabrication of the electrochemical 3D printer; 3D printing single dots and lines; 4D printing multi-material structures; and fabrication of pure copper-coated carbonized PAN-MnO electrospun nanofibre film for both electrode and current collector in a supercapacitor. And the noval 3D printing and electrospinning combined approaches make it possible to fabricate a high mass loading and high performance copper-fibre based supercapacitor which enabling further possibility to create more integrated electrodes and eventually to enhance the performance of supercapacitor.

Within the work in the first stage on system design and fabrication the following has been presented in this thesis:

- This low-cost desktop electrochemical 3D printer was converted from a commercial fused deposition modelling 3D printer, where a xyz movement system was maintained but with the replacement with a new meniscus-confined electrochemical deposition system;

- This printer first time uses sponge-filled and electrospun nanofiber-filled nozzles to form a stable meniscus by balancing the hydraulic head of a static electrolyte with the back pressure, allowing for a faster volumetric deposition speed of up to 19,667 $\mu m^3.s^{-1}$;

- Initially, static printing of copper dots and lines from a 1 M CuSO4 solution at voltages of 1V – 3V vs. Cu shows dense structures without noticeable dendritic formations with a faster deposition speed (19,667 $\mu m^3.s^{-1}$), which is 3 orders of magnitude faster than previously reported copper deposition studies;

- SEM results confirmed the printed structures had a noticeable polycrystalline grain structure, with decreasing grain size with increasing deposition potential. Mechanical and electrical characterization, show that the Vickers hardness and electrical resistivity are higher than cold worked cast copper due to the fine grain structure;

- This initial validation confirms the printability of the ECAM system at high moving speed and low cost.

Further investigations were conducted by printing multi-material (Cu-Ni and Cu-Ni-Cu multi –layer) functional structures. The following has been presented:

- The printer was improved by replacing a dual print head enabling multiple material printing;

- SEM imaging and EDS analysis showed that a tightly bound interface was formed between the copper and nickel layers, with printed lines exhibiting a convex cross section due to the higher reaction current density at the centre of the nozzle;

- Optical microscopy during heating of various printed samples including Cu-Ni and Cu-Ni-Cu structures demonstrated the ability of the technique in creating different movements. This was highlighted through the creation of structures such as the letters “ICL” and a simple temperature sensing circuit;

- When comparing measured results with the analytical solution, differences were observed which has been attributed to the uneven deposition of nickel onto the copper which is confirmed by XCT analysis;

- The findings here thus present the first reported multi-metal 3D printing approach for creating high temperature 4D structures which opens the possibility for creating more intelligent structures and sensors.

A combined manufacturing method via electrochemical 3D printing and electrospinning was proposed to produce a novel copper-nanofibre supercapacitor. The following were presented in this thesis regarding the application of the developed technology:

- An integrated high mass loading copper and 30 Mn@CNF supercapacitor has been fabricated using this combined technique with the specific capacitance increased from 99 F g^{-1} to 208 F g^{-1} at 5 mV s^{-1};
- The analysis of Impedance Nyquist plots and conductivity show that performance of supercapacitor has been improved with an increased conductivity up to 46 S m^{-1} and a decrease of contact resistance down to 8 Ω cm^2;
- The hydrophilic surface wettability of electrospun high mass loading fibres with a contact angle of 46º present an outstanding ability in creating the dense and continuous copper-fibre structure;

This combined approach enables further possibility to create more integrated electrodes and eventually to enhance the performance of supercapacitor.

The contents of the thesis therefore present current state-of-art the electrochemical additive manufacturing techniques for producing metal parts in terms of various systems, fabrication scales and applications. The aim of this thesis was to develop an electrochemical metal 3D printer to realize large-scale metal 3D/4D printing of low cost. The author realises macro-scale metal 3D printing of multiple shapes, such as dots, lines and letters, using electrochemical AM technique, which enables this technique not to be limited in micro-/nano- scale fabrication. Furthermore, the findings in the thesis present the first reported multi-metal 3D printing approach for creating high temperature 4D structures that opens the possibility for creating more intelligent structures and sensors. The presented low-cost metal 3D printing system have shown the capability of fabricating single, multiple metal structures which is promising for macro-scale applications in the fields of circuit boards fabrication, supercapacitor, biomedical engineering, etc.

7.2 Future Work

This low-cost ECAM desktop 3D printer is capable of producing single and multi-metal complex 3D and 4D structures at higher deposition speeds. Applications that may benefit from this technology include intelligent functional structures for sensors and energy storage technologies. In order to further improve the system, the following research activities should be conducted in the future:

i. Currently, the printer is still in the proof of concept prototype. Future work includes: improved meniscus stability control, along with temperature and voltage control in the software in order to fully automate the system.
ii. The simple mechanical sample removal method from the substrate can be a barrier to scale up and can limit in the design complexity of components. The foundational work done on multi-metal ECAM has demonstrated that bi-metallic structures can be created which opens the possibility for creating sacrificial support structures and easier removal of the component from the substrate through chemical removal methods. This however, requires further research in the future.
iii. In the present work, only single metal depositions were demonstrated, however there are a number of electrochemical deposition systems which can produce alloys of materials. Future work could expand into the deposition of alloys.
iv. The current approach used in this work used a meniscus confined approach for localising the deposition with a challenge being the stability of the meniscus, since crystal deposits on the substrate from the residual liquid left behind from meniscus trail, affecting the printing process and will result in low print quality. Alternative methods such as using a hydrogel-based tip could be investigated to improve the stability of the localised deposition.
v. The humidity control during the ECAM process was not considered, but it has great impact on the growth rate and geometry uniformity of the deposits. Precise humidity control will be included in the future works.

References

[1] W. Gao, Y. Zhang, D. Ramanujan, K. Ramani, Y. Chen, C.B. Williams, C.C. Wang, Y.C. Shin, S. Zhang, P.D. Zavattieri, The status, challenges, and future of additive manufacturing in engineering, Computer-Aided Design 69 (2015) 65-89.
[2] B. Dutta, F.H.S. Froes, The additive manufacturing (AM) of titanium alloys, Titanium powder metallurgy, Elsevier2015, pp. 447-468.
[3] R. Liu, Z. Wang, T. Sparks, F. Liou, J. Newkirk, Aerospace applications of laser additive manufacturing, Laser Additive Manufacturing, Elsevier2017, pp. 351-371.
[4] T. Page, A feasibility study of additive fabrication in component replacement and customised automotive modifications, International Journal of Manufacturing, Materials, and Mechanical Engineering (IJMMME) 8(4) (2018).
[5] A. Youssef, S.J. Hollister, P.D. Dalton, Additive manufacturing of polymer melts for implantable medical devices and scaffolds, Biofabrication 9(1) (2017) 012002.
[6] T. Duda, L.V. Raghavan, 3D metal printing technology, IFAC-PapersOnLine 49(29) (2016) 103-110.
[7] F. Mangano, L. Chambrone, R. Van Noort, C. Miller, P. Hatton, C. Mangano, Direct metal laser sintering titanium dental implants: a review of the current literature, International journal of biomaterials 2014 (2014).
[8] W.E. Frazier, Metal additive manufacturing: a review, Journal of Materials Engineering and Performance 23(6) (2014) 1917-1928.
[9] K.A. Ibrahim, B. Wu, N.P. Brandon, Electrical conductivity and porosity in stainless steel 316L scaffolds for electrochemical devices fabricated using selective laser sintering, Materials & Design 106 (2016) 51-59.
[10] G. Kardys, Factors to Consider When 3D Printing or Additive Manufacturing Metal Parts, Engineering 360, 2017.
[11] M. Paunovic, M. Schlesinger, Fundamentals of electrochemical deposition, john wiley & sons2006.
[12] S. Shailendar, M.M. Sundaram, A Feasibility Study of Localized Electrochemical Deposition Using Liquid Marbles, Materials and Manufacturing Processes 31(1) (2016) 81-86.
[13] Y. Lei, X. Zhang, D. Xu, M. Yu, Z. Yi, Z. Li, A. Sun, G. Xu, P. Cui, J. Guo, Dynamic “Scanning-Mode” Meniscus Confined Electrodepositing and Micropatterning of Individually Addressable Ultraconductive Copper Line Arrays, The journal of physical chemistry letters 9(9) (2018) 2380-2387.
[14] S. Daryadel, A. Behroozfar, S.R. Morsali, S. Moreno, M. Baniasadi, J. Bykova, R.A. Bernal, M. Minary-Jolandan, Localized Pulsed Electrodeposition Process for Three-Dimensional Printing of Nanotwinned Metallic Nanostructures, Nano letters 18(1) (2017) 208-214.
[15] A.P. Suryavanshi, M.-F. Yu, Probe-based electrochemical fabrication of freestanding Cu nanowire array, Applied Physics Letters 88(8) (2006) 083103.
[16] S.K. Seol, D. Kim, S. Lee, J.H. Kim, W.S. Chang, J.T. Kim, Electrodeposition‐based 3D Printing of Metallic Microarchitectures with Controlled Internal Structures, Small 11(32) (2015) 3896-3902.
[17] R. Von Gutfeld, D. Vigliotti, High‐speed electroplating of copper using the laser‐jet technique, Applied Physics Letters 46(10) (1985) 1003-1005.
[18] K.V. Wong, A. Hernandez, A review of additive manufacturing, ISRN Mechanical Engineering 2012 (2012).
[19] A. Ambrosi, M. Pumera, 3D-printing technologies for electrochemical applications, Chemical Society Reviews 45(10) (2016) 2740-2755.

[20] S.H. Huang, P. Liu, A. Mokasdar, L. Hou, Additive manufacturing and its societal impact: a literature review, The International Journal of Advanced Manufacturing Technology 67(5-8) (2013) 1191-1203.
[21] B.C. Gross, J.L. Erkal, S.Y. Lockwood, C. Chen, D.M. Spence, Evaluation of 3D printing and its potential impact on biotechnology and the chemical sciences, ACS Publications, 2014.
[22] D. Systems, 30 Years of Innovation. http://www.3dsystems.com/30-years-innovation
[23] B. Mueller, Additive manufacturing technologies–Rapid prototyping to direct digital manufacturing, Assembly Automation 32(2) (2012).
[24] R. Singh, Some investigations for small-sized product fabrication with FDM for plastic components, Rapid Prototyping Journal 19(1) (2013) 58-63.
[25] J. Deckers, J. Vleugels, J.-P. Kruth, Additive manufacturing of ceramics: a review, Journal of Ceramic Science and Technology 5(4) (2014) 245-260.
[26] Z. Quan, A. Wu, M. Keefe, X. Qin, J. Yu, J. Suhr, J.-H. Byun, B.-S. Kim, T.-W. Chou, Additive manufacturing of multi-directional preforms for composites: opportunities and challenges, Materials Today 18(9) (2015) 503-512.
[27] Y. Song, Y. Yan, R. Zhang, D. Xu, F. Wang, Manufacture of the die of an automobile deck part based on rapid prototyping and rapid tooling technology, Journal of materials processing technology 120(1-3) (2002) 237-242.
[28] C.L. Thomas, T.M. Gaffney, S. Kaza, C.H. Lee, Rapid prototyping of large scale aerospace structures, Aerospace Applications Conference, 1996. Proceedings., 1996 IEEE, IEEE, 1996, pp. 219-230.
[29] J.I. Lipton, M. Cutler, F. Nigl, D. Cohen, H. Lipson, Additive manufacturing for the food industry, Trends in food science & technology 43(1) (2015) 114-123.
[30] F. Rengier, A. Mehndiratta, H. Von Tengg-Kobligk, C.M. Zechmann, R. Unterhinninghofen, H.-U. Kauczor, F.L. Giesel, 3D printing based on imaging data: review of medical applications, International journal of computer assisted radiology and surgery 5(4) (2010) 335-341.
[31] H. Daanen, S.-A. Hong, Made-to-measure pattern development based on 3D whole body scans, International Journal of Clothing Science and Technology 20(1) (2008) 15-25.
[32] Z. Wang, R. Abdulla, B. Parker, R. Samanipour, S. Ghosh, K. Kim, A simple and high-resolution stereolithography-based 3D bioprinting system using visible light crosslinkable bioinks, Biofabrication 7(4) (2015) 045009.
[33] E.J. Mott, M. Busso, X. Luo, C. Dolder, M.O. Wang, J.P. Fisher, D. Dean, Digital micromirror device (DMD)-based 3D printing of poly (propylene fumarate) scaffolds, Materials Science and Engineering: C 61 (2016) 301-311.
[34] P.J. Bártolo, Stereolithography: materials, processes and applications, Springer Science & Business Media2011.
[35] C. Sun, N. Fang, D. Wu, X. Zhang, Projection micro-stereolithography using digital micro-mirror dynamic mask, Sensors and Actuators A: Physical 121(1) (2005) 113-120.
[36] S.H. Park, D.Y. Yang, K.S. Lee, Two‐photon stereolithography for realizing ultraprecise three‐dimensional nano/microdevices, Laser & Photonics Reviews 3(1‐2) (2009) 1-11.
[37] E. Rune, Measuring instrument of the recording type, Google Patents, 1951.
[38] R.G. Sweet, High frequency recording with electrostatically deflected ink jets, Review of scientific instruments 36(2) (1965) 131-136.
[39] S.I. Zoltan, Pulsed droplet ejecting system, Google Patents, 1972.
[40] M. Singh, H.M. Haverinen, P. Dhagat, G.E. Jabbour, Inkjet printing—process and its applications, Advanced materials 22(6) (2010) 673-685.
[41] B.J. de Gans, P.C. Duineveld, U.S. Schubert, Inkjet printing of polymers: state of the art and future developments, Advanced materials 16(3) (2004) 203-213.
[42] T. Villwock, Magnetic fluid suitable for high speed and high resolution dot-on-demand inkjet printing and method of making, Google Patents, 2016.
[43] J.J. Beaman, C.R. Deckard, Selective laser sintering with assisted powder handling, Google Patents, 1990.

[44] A. Pfister, R. Landers, A. Laib, U. Hübner, R. Schmelzeisen, R. Mülhaupt, Biofunctional rapid prototyping for tissue‐engineering applications: 3D bioplotting versus 3D printing, Journal of Polymer Science Part A: Polymer Chemistry 42(3) (2004) 624-638.
[45] J.L. Bennett, S.J. Wolff, G. Hyatt, K. Ehmann, J. Cao, Thermal effect on clad dimension for laser deposited Inconel 718, Journal of Manufacturing Processes 28 (2017) 550-557.
[46] S.H. Ko, I. Park, H. Pan, C.P. Grigoropoulos, A.P. Pisano, C.K. Luscombe, J.M. Fréchet, Direct nanoimprinting of metal nanoparticles for nanoscale electronics fabrication, Nano letters 7(7) (2007) 1869-1877.
[47] L. Costa, R. Vilar, Laser powder deposition, Rapid Prototyping Journal 15(4) (2009) 264-279.
[48] J. Bennett, R. Dudas, J. Cao, K. Ehmann, G. Hyatt, Control of heating and cooling for direct laser deposition repair of cast iron components, Flexible Automation (ISFA), International Symposium on, IEEE, 2016, pp. 229-236.
[49] W. King, A. Anderson, R. Ferencz, N. Hodge, C. Kamath, S. Khairallah, A. Rubenchik, Laser powder bed fusion additive manufacturing of metals; physics, computational, and materials challenges, Applied Physics Reviews 2(4) (2015) 041304.
[50] Y. Lee, W. Zhang, Modeling of heat transfer, fluid flow and solidification microstructure of nickel-base superalloy fabricated by laser powder bed fusion, Additive Manufacturing 12 (2016) 178-188.
[51] S. Crump, Fused deposition modeling (FDM): putting rapid back in prototyping, Proc. 2nd Int. Conf. Rapid Prototyping, 23–26 June, Dayton, OH, 1991, pp. 358-361.
[52] S.S. Crump, Apparatus and method for creating three-dimensional objects, Google Patents, 1992.
[53] R. Jones, P. Haufe, E. Sells, P. Iravani, V. Olliver, C. Palmer, A. Bowyer, RepRap–the replicating rapid prototyper, Robotica 29(1) (2011) 177-191.
[54] P. Dudek, FDM 3D printing technology in manufacturing composite elements, Archives of Metallurgy and Materials 58(4) (2013) 1415-1418.
[55] L. Novakova-Marcincinova, J. Novak-Marcincin, J. Barna, J. Torok, Special materials used in FDM rapid prototyping technology application, Intelligent Engineering Systems (INES), 2012 IEEE 16th International Conference on, IEEE, 2012, pp. 73-76.
[56] O. Carneiro, A. Silva, R. Gomes, Fused deposition modeling with polypropylene, Materials & Design 83 (2015) 768-776.
[57] B. Kianian, Wohlers Report 2017: 3D Printing and Additive Manufacturing State of the Industry, Annual Worldwide Progress Report: Chapters titles: The Middle East, and other countries, (2017).
[58] M. Shofner, K. Lozano, F. Rodríguez‐Macías, E. Barrera, Nanofiber‐reinforced polymers prepared by fused deposition modeling, Journal of applied polymer science 89(11) (2003) 3081-3090.
[59] W. Zhong, F. Li, Z. Zhang, L. Song, Z. Li, Short fiber reinforced composites for fused deposition modeling, Materials Science and Engineering: A 301(2) (2001) 125-130.
[60] R. Singh, S. Singh, F. Fraternali, Development of in-house composite wire based feed stock filaments of fused deposition modelling for wear-resistant materials and structures, Composites Part B: Engineering 98 (2016) 244-249.
[61] F. Ning, W. Cong, Y. Hu, H. Wang, Additive manufacturing of carbon fiber-reinforced plastic composites using fused deposition modeling: Effects of process parameters on tensile properties, Journal of Composite Materials 51(4) (2017) 451-462.
[62] S. Singh, R. Singh, Characterization of Al–Al2O3 composite prepared using reinforced fused deposition pattern in investment casting, Proceedings of the Institution of Mechanical Engineers, Part L: Journal of Materials: Design and Applications 230(2) (2016) 689-696.
[63] S. Fernández, M. Jiménez, J. Porras, L. Romero, M. Espinosa, M. Domínguez, Additive manufacturing and performance of functional hydraulic pump impellers in fused deposition modeling technology, Journal of Mechanical Design 138(2) (2016) 024501.
[64] S.R. Barber, E.D. Kozin, M. Dedmon, B.M. Lin, K. Lee, S. Sinha, N. Black, A.K. Remenschneider, D.J. Lee, 3D-printed pediatric endoscopic ear surgery simulator for surgical training, International journal of pediatric otorhinolaryngology 90 (2016) 113-118.

[65] A. Salea, R. Prathumwan, J. Junpha, K. Subannajui, Metal oxide semiconductor 3D printing: Preparation of copper (II) oxide by fused deposition modelling for multi-functional semiconducting applications, Journal of Materials Chemistry C 5(19) (2017) 4614-4620.
[66] Y. Xie, S. Ye, C. Reyes, P. Sithikong, B.-I. Popa, B.J. Wiley, S.A. Cummer, Microwave metamaterials made by fused deposition 3D printing of a highly conductive copper-based filament, Applied Physics Letters 110(18) (2017) 181903.
[67] S. Hwang, E.I. Reyes, K.-s. Moon, R.C. Rumpf, N.S. Kim, Thermo-mechanical characterization of metal/polymer composite filaments and printing parameter study for fused deposition modeling in the 3D printing process, Journal of Electronic Materials 44(3) (2015) 771-777.
[68] A.L. Rutz, K.E. Hyland, A.E. Jakus, W.R. Burghardt, R.N. Shah, A multimaterial bioink method for 3D printing tunable, cell‐compatible hydrogels, Advanced materials 27(9) (2015) 1607-1614.
[69] A.E. Jakus, R. Shah, Multi and mixed 3D‐printing of graphene‐hydroxyapatite hybrid materials for complex tissue engineering, Journal of Biomedical Materials Research Part A 105(1) (2017) 274-283.
[70] M.E. Hoque, Y.L. Chuan, I. Pashby, Extrusion based rapid prototyping technique: an advanced platform for tissue engineering scaffold fabrication, Biopolymers 97(2) (2012) 83-93.
[71] A. Bellini, Fused deposition of ceramics: a comprehensive experimental, analytical and computational study of material behavior, fabrication process and equipment design, 2002.
[72] H. Almeida, P. Bartolo, C. Mota, A. Mateus, N. Ferreira, M. Domingos, Processo e equipamento de fabrico rápido por bioextrusão, Portuguese Patent Application 104247 (2010).
[73] L.G. Zhang, J.P. Fisher, K. Leong, 3D Bioprinting and nanotechnology in tissue engineering and regenerative medicine, Academic Press2015.
[74] M. Feygin, A. Shkolnik, M.N. Diamond, E. Dvorskiy, Laminated object manufacturing system, Google Patents, 1998.
[75] J. Park, M.J. Tari, H.T. Hahn, Characterization of the laminated object manufacturing (LOM) process, Rapid Prototyping Journal 6(1) (2000) 36-50.
[76] H. Windsheimer, N. Travitzky, A. Hofenauer, P. Greil, Laminated Object Manufacturing of Preceramic‐Paper‐Derived Si? SiC Composites, Advanced materials 19(24) (2007) 4515-4519.
[77] M. Prechtl, A. Otto, M. Geiger, Rapid tooling by laminated object manufacturing of metal foil, Advanced Materials Research, Trans Tech Publ, 2005, pp. 303-312.
[78] H.L. Marcus, J.J. Beeman, J.W. Barlow, D.L. Bourell, R.H. Crawford, Solid Freeform Fabrication Symposium Proceedings, NASA STI/Recon Technical Report N 94 (1993).
[79] J. Stampfl, S. Baudis, C. Heller, R. Liska, A. Neumeister, R. Kling, A. Ostendorf, M. Spitzbart, Photopolymers with tunable mechanical properties processed by laser-based high-resolution stereolithography, Journal of Micromechanics and Microengineering 18(12) (2008) 125014.
[80] N.T. Dinh, E. Sowade, T. Blaudeck, S. Hermann, R.D. Rodriguez, D.R. Zahn, S.E. Schulz, R.R. Baumann, O. Kanoun, High-resolution inkjet printing of conductive carbon nanotube twin lines utilizing evaporation-driven self-assembly, Carbon 96 (2016) 382-393.
[81] B.W. An, K. Kim, H. Lee, S.Y. Kim, Y. Shim, D.Y. Lee, J.Y. Song, J.U. Park, High‐resolution printing of 3D structures using an electrohydrodynamic inkjet with multiple functional inks, Advanced Materials 27(29) (2015) 4322-4328.
[82] I. Theodorakos, F. Zacharatos, R. Geremia, D. Karnakis, I. Zergioti, Selective laser sintering of Ag nanoparticles ink for applications in flexible electronics, Applied surface science 336 (2015) 157-162.
[83] B. Duan, M. Wang, W.Y. Zhou, W.L. Cheung, Z.Y. Li, W.W. Lu, Three-dimensional nanocomposite scaffolds fabricated via selective laser sintering for bone tissue engineering, Acta biomaterialia 6(12) (2010) 4495-4505.
[84] A. Boschetto, L. Bottini, Accuracy prediction in fused deposition modeling, The international journal of advanced manufacturing technology 73(5-8) (2014) 913-928.
[85] J. Skowyra, K. Pietrzak, M.A. Alhnan, Fabrication of extended-release patient-tailored prednisolone tablets via fused deposition modelling (FDM) 3D printing, European Journal of Pharmaceutical Sciences 68 (2015) 11-17.

[86] B.N. Turner, S.A. Gold, A review of melt extrusion additive manufacturing processes: II. Materials, dimensional accuracy, and surface roughness, Rapid Prototyping Journal 21(3) (2015) 250-261.
[87] B.K. Paul, V. Voorakarnam, Effect of layer thickness and orientation angle on surface roughness in laminated object manufacturing, Journal of manufacturing processes 3(2) (2001) 94.
[88] M. Vaezi, S. Yang, Extrusion-based additive manufacturing of PEEK for biomedical applications, Virtual and Physical Prototyping 10(3) (2015) 123-135.
[89] Y. Liu, Y. Yang, D. Wang, A study on the residual stress during selective laser melting (SLM) of metallic powder, The International Journal of Advanced Manufacturing Technology 87(1-4) (2016) 647-656.
[90] P. Edwards, M. Ramulu, Fatigue performance evaluation of selective laser melted Ti–6Al–4V, Materials Science and Engineering: A 598 (2014) 327-337.
[91] G. Strano, L. Hao, R. Everson, K. Evans, A new approach to the design and optimisation of support structures in additive manufacturing, The International Journal of Advanced Manufacturing Technology 66(9-12) (2013) 1247-1254.
[92] X. Chen, X. Liu, P. Childs, N. Brandon, B. Wu, A Low Cost Desktop Electrochemical Metal 3D Printer, Advanced Materials Technologies 2(10) (2017).
[93] A. Brant, M. Sundaram, A novel electrochemical micro additive manufacturing method of overhanging metal parts without reliance on support structures, Procedia Manufacturing 5 (2016) 928-943.
[94] A. Kamaraj, S. Lewis, M. Sundaram, Numerical study of localized electrochemical deposition for micro electrochemical additive manufacturing, Procedia CIRP 42 (2016) 788-792.
[95] A.J. Bard, O.E. Huesser, D.H. Craston, High resolution deposition and etching in polymer films, Google Patents, 1990.
[96] M. Paunovic, M. Schlesinger, Fundamentals of electrochemical deposition, New York (1998).
[97] M. Schlesinger, M. Paunovic, Modern electroplating, John Wiley & Sons2011.
[98] A.L. Cohen, Method for electrochemical fabrication, Google Patents, 2000.
[99] A. Cohen, G. Zhang, F.-G. Tseng, U. Frodis, F. Mansfeld, P. Will, EFAB: rapid, low-cost desktop micromachining of high aspect ratio true 3-D MEMS, Micro Electro Mechanical Systems, 1999. MEMS'99. Twelfth IEEE International Conference on, IEEE, 1999, pp. 244-251.
[100] T.M. Braun, D.T. Schwartz, The Emerging Role of Electrodeposition in Additive Manufacturing, The Electrochemical Society Interface 25(1) (2016) 69-73.
[101] G. Zhang, Monitoring of instant-mask plating for fabrication of patterned copper microstructures, ECS Transactions 3(10) (2006) 325-335.
[102] D. Wang, C. Wen, Y. Chang, W. Lin, S.-C. Chen, Ultrafast laser-enabled 3D metal printing: A solution to fabricate arbitrary submicron metal structures, Precision Engineering (2017).
[103] W. Wang, M.R. Holl, D.T. Schwartz, Rapid prototyping of masks for through-mask electrodeposition of thick metallic components, Journal of the Electrochemical Society 148(5) (2001) C363-C368.
[104] S.D. Leith, D.T. Schwartz, In-situ fabrication of sacrificial layers in electrodeposited NiFe microstructures, Journal of Micromechanics and Microengineering 9(1) (1999) 97.
[105] S.E. Alper, I.E. Ocak, T. Akin, Ultrathick and high-aspect-ratio nickel microgyroscope using EFAB multilayer additive electroforming, Journal of Microelectromechanical Systems 16(5) (2007) 1025-1035.
[106] A. Cohen, R. Chen, U. Frodis, M.-T. Wu, C. Folk, Microscale metal additive manufacturing of multi-component medical devices, Rapid Prototyping Journal 16(3) (2010) 209-215.
[107] A.H. Gosline, N.V. Vasilyev, A. Veeramani, M. Wu, G. Schmitz, R. Chen, V. Arabagi, J. Pedro, P.E. Dupont, Metal MEMS tools for beating-heart tissue removal, Robotics and Automation (ICRA), 2012 IEEE International Conference on, IEEE, 2012, pp. 1921-1926.
[108] B. Fernandez, J. Kubby, Design, processing, and materials for large-stroke actuators, MEMS Adaptive Optics, International Society for Optics and Photonics, 2007, p. 64670T.
[109] A.A. Yazdi, A. Popma, W. Wong, T. Nguyen, Y. Pan, J. Xu, 3D printing: an emerging tool for novel microfluidics and lab-on-a-chip applications, Microfluidics and Nanofluidics 20(3) (2016) 50.

[110] J.B. Nelson, D.T. Schwartz, Electrochemical printing: in situ characterization using an electrochemical quartz crystal microbalance, Journal of Micromechanics and Microengineering 15(12) (2005) 2479.
[111] J.D. Madden, I.W. Hunter, Three-dimensional microfabrication by localized electrochemical deposition, Journal of Microelectromechanical Systems 5(1) (1996) 24-32.
[112] K. Chen, G. Evans, Two-dimensional modeling of nickel electrodeposition in LIGA microfabrication, Microsystem technologies 10(6-7) (2004) 444-450.
[113] R. Said, Localized electro-deposition (LED): the march toward process development, Nanotechnology 15(10) (2004) S649.
[114] H.C. Shin, J. Dong, M. Liu, Nanoporous structures prepared by an electrochemical deposition process, Advanced materials 15(19) (2003) 1610-1614.
[115] A. Müller, F. Müller, M. Hietschold, Localized electrochemical deposition of metals using micropipettes, Thin Solid Films 366(1-2) (2000) 32-36.
[116] S.K. Seol, A.R. Pyun, Y. Hwu, G. Margaritondo, J.H. Je, Localized Electrochemical Deposition of Copper Monitored Using Real‐Time X‐ray Microradiography, Advanced Functional Materials 15(6) (2005) 934-937.
[117] A.M. Brant, M. Sundaram, A fundamental study of nano electrodeposition using a combined molecular dynamics and quantum mechanical electron force field approach, Procedia Manufacturing 10 (2017) 253-264.
[118] E. El‐Giar, R. Said, G. Bridges, D. Thomson, Localized electrochemical deposition of copper microstructures, Journal of the Electrochemical Society 147(2) (2000) 586-591.
[119] M.H. Gelchinski, L.T. Romankiw, D.R. Vigliotti, R.J.V. Gutfeld, Laser-enhanced jet-plating and jet-etching: high-speed maskless patterning method, Google Patents, 1985.
[120] S. Yeo, J. Choo, Effects of rotor electrode in the fabrication of high aspect ratio microstructures by localized electrochemical deposition, Journal of Micromechanics and Microengineering 11(5) (2001) 435.
[121] S. Yeo, J. Choo, K. Sim, On the effects of ultrasonic vibrations on localized electrochemical deposition, Journal of Micromechanics and Microengineering 12(3) (2002) 271.
[122] J. Lin, T. Chang, J. Yang, Y. Chen, C. Chuang, Localized electrochemical deposition of micrometer copper columns by pulse plating, Electrochimica Acta 55(6) (2010) 1888-1894.
[123] S. Lajevardi, T. Shahrabi, Effects of pulse electrodeposition parameters on the properties of Ni–TiO2 nanocomposite coatings, Applied Surface Science 256(22) (2010) 6775-6781.
[124] Y. Yang, Y. Cheng, Fabrication of Ni–Co–SiC composite coatings by pulse electrodeposition—Effects of duty cycle and pulse frequency, Surface and Coatings Technology 216 (2013) 282-288.
[125] M.M. Sundaram, A.B. Kamaraj, V.S. Kumar, Mask-less electrochemical additive manufacturing: a feasibility study, Journal of Manufacturing Science and Engineering 137(2) (2015) 021006.
[126] M. Chandrasekar, M. Pushpavanam, Pulse and pulse reverse plating—Conceptual, advantages and applications, Electrochimica Acta 53(8) (2008) 3313-3322.
[127] L. Hirt, S. Ihle, Z. Pan, L. Dorwling‐Carter, A. Reiser, J.M. Wheeler, R. Spolenak, J. Vörös, T. Zambelli, Template‐Free 3D Microprinting of Metals Using a Force‐Controlled Nanopipette for Layer‐by‐Layer Electrodeposition, Advanced materials 28(12) (2016) 2311-2315.
[128] S.C. Lai, R.A. Lazenby, P.M. Kirkman, P.R. Unwin, Nucleation, aggregative growth and detachment of metal nanoparticles during electrodeposition at electrode surfaces, Chemical science 6(2) (2015) 1126-1138.
[129] J. Hu, M.-F. Yu, Meniscus-confined three-dimensional electrodeposition for direct writing of wire bonds, Science 329(5989) (2010) 313-316.
[130] J. Eastoe, J. Dalton, Dynamic surface tension and adsorption mechanisms of surfactants at the air–water interface, Advances in colloid and interface science 85(2-3) (2000) 103-144.
[131] D.T. Schwartz, J.D. Whitaker, Electrochemical micromanufacturing system and method, Google Patents, 2009.
[132] I.W. Hunter, S.R. Lafontaine, J.D. Madden, Three dimensional microfabrication by localized electrodeposition and etching, Google Patents, 1997.

[133] T. Watanabe, M. Sagiyama, M. Kawabe, T. Tsujihara, S. Takushima, Apparatus for removing electroplating metal deposited onto surface of conductor roll, Google Patents, 1990.
[134] E.J. Taylor, M.E. Inman, B.T. Skinn, T.D. Hall, S.T. Snyder, S.C. Lucatero, E.L. Kathe, Apparatus and method for recovery of material generated during electrochemical material removal in acidic electrolytes, Google Patents, 2018.
[135] D.M. Wirth, D.F. Pain, J.W. Herman, Three dimensional additive manufacturing of metal objects by stereo-electrochemical deposition, Google Patents, 2017.
[136] M. Sundaram, Additive manufacturing by localized electrochemical deposition, Google Patents, 2019.
[137] J. Hu, Interfacial physics in meniscus-confined electrodeposition and its applications for fabricating electronic structures, University of Illinois at Urbana-Champaign, 2011.
[138] A.P. Suryavanshi, Meniscus Controlled Three-Dimensional Nanofabrication, Department of Mechanical Science and Engineering, University of Illinois, Urbana-Champaign, 2007.
[139] A.J. Brad, Faulkner, L. R., Electrochemical Methods: Fundamentals and Applications, John Wiley, New York, 2001.
[140] N. Elgrishi, K.J. Rountree, B.D. McCarthy, E.S. Rountree, T.T. Eisenhart, J.L. Dempsey, A practical beginner's guide to cyclic voltammetry, Journal of Chemical Education 95(2) (2018) 197-206.
[141] S. Morsali, S. Daryadel, Z. Zhou, A. Behroozfar, M. Baniasadi, S. Moreno, D. Qian, M. Minary-Jolandan, Multi-physics simulation of metal printing at micro/nanoscale using meniscus-confined electrodeposition: Effect of nozzle speed and diameter, Journal of Applied Physics 121(21) (2017) 214305.
[142] E. Pitts, The stability of a meniscus joining a vertical rod to a bath of liquid, Journal of Fluid Mechanics 76(4) (1976) 641-651.
[143] D. Michael, Meniscus stability, Annual Review of Fluid Mechanics 13(1) (1981) 189-216.
[144] V. Tatarchenko, Capillary shaping in crystal growth from melts: I. Theory, Journal of Crystal Growth 37(3) (1977) 272-284.
[145] G. Satunkin, V. Tatarchenko, Shape analysis and meniscus height calculations for various types of capillary shaping, Journal of colloid and interface science 104(2) (1985) 318-333.
[146] K.I. Popov, S.S. Djokić, N.D. Nikolić, V.D. Jović, Morphology of electrochemically and chemically deposited metals, Springer2016.
[147] V.A. Tatarchenko, Shaped crystal growth, Springer Science & Business Media2013.
[148] M. Seo, I. Sawamura, L. Grasjo, Y. Haga, N. Sato, Measurement of minute corrosion of copper thin film by a quartz crystal microbalance, Journal of the Society of Materials Science, Japan 39(439) (1990) 357-361.
[149] H. Ghasemi, C. Ward, Sessile-Water-Droplet Contact Angle Dependence on Adsorption at the Solid− Liquid Interface, The Journal of Physical Chemistry C 114(11) (2010) 5088-5100.
[150] C. Laslau, D.E. Williams, B. Kannan, J. Travas‐Sejdic, Scanned pipette techniques for the highly localized electrochemical fabrication and characterization of conducting polymer thin films, microspots, microribbons, and nanowires, Advanced Functional Materials 21(24) (2011) 4607-4616.
[151] <http://nw3weather.co.uk/wx10.php>, (accessed 01/12/2020.2020).
[152] E. Cakmak, K.C. Tekin, U. Malayoglu, S. Shrestha, The effect of substrate composition on the electrochemical and mechanical properties of PEO coatings on Mg alloys, Surface and Coatings Technology 204(8) (2010) 1305-1313.
[153] R. Ambat, W. Zhou, Electroless nickel-plating on AZ91D magnesium alloy: effect of substrate microstructure and plating parameters, Surface and Coatings Technology 179(2-3) (2004) 124-134.
[154] R. Yerushalmi, A. Scherz, M.E. Van Der Boom, H.-B. Kraatz, Stimuli responsive materials: new avenues toward smart organic devices, Journal of Materials Chemistry 15(42) (2005) 4480-4487.
[155] P. Theato, B.S. Sumerlin, R.K. O'Reilly, T.H. Epps III, Stimuli responsive materials, Chemical Society Reviews 42(17) (2013) 7055-7056.

[156] Z.X. Khoo, J.E.M. Teoh, Y. Liu, C.K. Chua, S. Yang, J. An, K.F. Leong, W.Y. Yeong, 3D printing of smart materials: A review on recent progresses in 4D printing, Virtual and Physical Prototyping 10(3) (2015) 103-122.
[157] Q. Ge, A.H. Sakhaei, H. Lee, C.K. Dunn, N.X. Fang, M.L. Dunn, Multimaterial 4D printing with tailorable shape memory polymers, Scientific reports 6 (2016) 31110.
[158] S. Tibbits, 4D printing: multi‐material shape change, Architectural Design 84(1) (2014) 116-121.
[159] D. Raviv, W. Zhao, C. McKnelly, A. Papadopoulou, A. Kadambi, B. Shi, S. Hirsch, D. Dikovsky, M. Zyracki, C. Olguin, Active printed materials for complex self-evolving deformations, Scientific reports 4 (2014) 7422.
[160] S. Miao, W. Zhu, N.J. Castro, M. Nowicki, X. Zhou, H. Cui, J.P. Fisher, L.G. Zhang, 4D printing smart biomedical scaffolds with novel soybean oil epoxidized acrylate, Scientific reports 6 (2016) 27226.
[161] M. Bodaghi, A. Damanpack, W. Liao, Self-expanding/shrinking structures by 4D printing, Smart Materials and Structures 25(10) (2016) 105034.
[162] T.-H. Kwok, C.C. Wang, D. Deng, Y. Zhang, Y. Chen, Four-dimensional printing for freeform surfaces: design optimization of origami and kirigami structures, Journal of Mechanical Design 137(11) (2015) 111413.
[163] Y. Zhang, F. Zhang, Z. Yan, Q. Ma, X. Li, Y. Huang, J.A. Rogers, Printing, folding and assembly methods for forming 3D mesostructures in advanced materials, Nature Reviews Materials 2(4) (2017) 17019.
[164] F. Momeni, X. Liu, J. Ni, A review of 4D printing, Materials & Design 122 (2017) 42-79.
[165] Q. Ge, H.J. Qi, M.L. Dunn, Active materials by four-dimension printing Applied Physics Letters 103(13) (2013) 131901.
[166] J. Wu, C. Yuan, Z. Ding, M. Isakov, Y. Mao, T. Wang, M.L. Dunn, H.J. Qi, Multi-shape active composites by 3D printing of digital shape memory polymers, Scientific reports 6 (2016) 24224.
[167] K. Yu, A. Ritchie, Y. Mao, M.L. Dunn, H.J. Qi, Controlled sequential shape changing components by 3D printing of shape memory polymer multimaterials, Procedia Iutam 12 (2015) 193-203.
[168] Q. Zhang, K. Zhang, G. Hu, Smart three-dimensional lightweight structure triggered from a thin composite sheet via 3D printing technique, Scientific reports 6 (2016) 22431.
[169] Y. Mao, K. Yu, M.S. Isakov, J. Wu, M.L. Dunn, H.J. Qi, Sequential self-folding structures by 3D printed digital shape memory polymers, Scientific reports 5 (2015) 13616.
[170] S.E. Bakarich, R. Gorkin III, M.I.H. Panhuis, G.M. Spinks, 4D printing with mechanically robust, thermally actuating hydrogels, Macromolecular rapid communications 36(12) (2015) 1211-1217.
[171] L. Zhang, H. Liang, J. Jacob, P. Naumov, Photogated humidity-driven motility, Nature communications 6 (2015) 7429.
[172] K. Zhang, A. Geissler, M. Standhardt, S. Mehlhase, M. Gallei, L. Chen, C.M. Thiele, Moisture-responsive films of cellulose stearoyl esters showing reversible shape transitions, Scientific reports 5 (2015) 11011.
[173] H. Okuzaki, T. Saido, H. Suzuki, Y. Hara, H. Yan, A biomorphic origami actuator fabricated by folding a conducting paper, Journal of Physics: Conference Series, IOP Publishing, 2008, p. 012001.
[174] H. Lu, Y. Liu, J. Gou, J. Leng, S. Du, Electrical properties and shape-memory behavior of self-assembled carbon nanofiber nanopaper incorporated with shape-memory polymer, Smart materials and Structures 19(7) (2010) 075021.
[175] S.-H. Hu, T.-Y. Liu, D.-M. Liu, S.-Y. Chen, Nano-ferrosponges for controlled drug release, Journal of Controlled Release 121(3) (2007) 181-189.
[176] D. Kokkinis, M. Schaffner, A.R. Studart, Multimaterial magnetically assisted 3D printing of composite materials, Nature communications 6 (2015) 8643.
[177] A.M. Kloxin, A.M. Kasko, C.N. Salinas, K.S. Anseth, Photodegradable hydrogels for dynamic tuning of physical and chemical properties, Science 324(5923) (2009) 59-63.
[178] C.A. DeForest, D.A. Tirrell, A photoreversible protein-patterning approach for guiding stem cell fate in three-dimensional gels, Nature materials 14(5) (2015) 523.

[179] M. Nadgorny, Z. Xiao, C. Chen, L.A. Connal, Three-dimensional printing of pH-responsive and functional polymers on an affordable desktop printer, ACS applied materials & interfaces 8(42) (2016) 28946-28954.
[180] S. Shaffer, K. Yang, J. Vargas, M.A. Di Prima, W. Voit, On reducing anisotropy in 3D printed polymers via ionizing radiation, Polymer 55(23) (2014) 5969-5979.
[181] Y.Y.C. Choong, S. Maleksaeedi, H. Eng, J. Wei, P.-C. Su, 4D printing of high performance shape memory polymer using stereolithography, Materials & Design 126 (2017) 219-225.
[182] M. Armand, J. Tarascon, Issues and challenges facing rechargeable batteries, Nature 414 (2001) 359-367.
[183] L. Mai, X. Tian, X. Xu, L. Chang, L. Xu, Nanowire electrodes for electrochemical energy storage devices, Chemical reviews 114(23) (2014) 11828-11862.
[184] C. Liu, F. Li, L.P. Ma, H.M. Cheng, Advanced materials for energy storage, Advanced materials 22(8) (2010) E28-E62.
[185] D. Aurbach, Review of selected electrode–solution interactions which determine the performance of Li and Li ion batteries, Journal of Power Sources 89(2) (2000) 206-218.
[186] Y. Gogotsi, P. Simon, True performance metrics in electrochemical energy storage, Science 334(6058) (2011) 917-918.
[187] R. Wu, D.P. Wang, X. Rui, B. Liu, K. Zhou, A.W. Law, Q. Yan, J. Wei, Z. Chen, In‐Situ Formation of Hollow Hybrids Composed of Cobalt Sulfides Embedded within Porous Carbon Polyhedra/Carbon Nanotubes for High‐Performance Lithium‐Ion Batteries, Advanced materials 27(19) (2015) 3038-3044.
[188] C. Bergmann, M. Lindner, W. Zhang, K. Koczur, A. Kirsten, R. Telle, H. Fischer, 3D printing of bone substitute implants using calcium phosphate and bioactive glasses, Journal of the European Ceramic Society 30(12) (2010) 2563-2567.
[189] A. Goulas, J.G. Binner, R.A. Harris, R.J. Friel, Assessing extraterrestrial regolith material simulants for in-situ resource utilisation based 3D printing, Applied Materials Today 6 (2017) 54-61.
[190] D. Qi, Y. Liu, Z. Liu, L. Zhang, X. Chen, Design of architectures and materials in in‐plane micro‐supercapacitors: current status and future challenges, Advanced Materials 29(5) (2017) 1602802.
[191] J.W. Long, B. Dunn, D.R. Rolison, H.S. White, Three-dimensional battery architectures, Chemical Reviews 104(10) (2004) 4463-4492.
[192] L. Baggetto, R.A. Niessen, F. Roozeboom, P.H. Notten, High energy density all‐solid‐state batteries: a challenging concept towards 3D integration, Advanced Functional Materials 18(7) (2008) 1057-1066.
[193] H. Li, Q. Zhao, W. Wang, H. Dong, D. Xu, G. Zou, H. Duan, D. Yu, Novel planar-structure electrochemical devices for highly flexible semitransparent power generation/storage sources, Nano letters 13(3) (2013) 1271-1277.
[194] M. Beidaghi, Y. Gogotsi, Capacitive energy storage in micro-scale devices: recent advances in design and fabrication of micro-supercapacitors, Energy & Environmental Science 7(3) (2014) 867-884.
[195] E. Malone, M. Berry, H. Lipson, Freeform fabrication and characterization of Zn-air batteries, Rapid Prototyping Journal 14(3) (2008) 128-140.
[196] J. Hu, Y. Jiang, S. Cui, Y. Duan, T. Liu, H. Guo, L. Lin, Y. Lin, J. Zheng, K. Amine, 3D‐printed cathodes of LiMn1− xFexPO4 nanocrystals achieve both ultrahigh rate and high capacity for advanced lithium‐ion battery, Advanced Energy Materials 6(18) (2016) 1600856.
[197] J. Yan, Q. Wang, T. Wei, Z. Fan, Recent advances in design and fabrication of electrochemical supercapacitors with high energy densities, Advanced Energy Materials 4(4) (2014).
[198] G. Wang, L. Zhang, J. Zhang, A review of electrode materials for electrochemical supercapacitors, Chemical Society Reviews 41(2) (2012) 797-828.
[199] B.E. Conway, Electrochemical supercapacitors: scientific fundamentals and technological applications, Springer Science & Business Media2013.

[200] X.Y. Yu, L. Yu, X.W. Lou, Metal sulfide hollow nanostructures for electrochemical energy storage, Advanced Energy Materials 6(3) (2016) 1501333.
[201] C. Zhu, T. Liu, F. Qian, T.Y.-J. Han, E.B. Duoss, J.D. Kuntz, C.M. Spadaccini, M.A. Worsley, Y. Li, Supercapacitors based on three-dimensional hierarchical graphene aerogels with periodic macropores, Nano letters 16(6) (2016) 3448-3456.
[202] A. Ambrosi, J.G.S. Moo, M. Pumera, Helical 3D‐Printed Metal Electrodes as Custom‐Shaped 3D Platform for Electrochemical Devices, Advanced Functional Materials 26(5) (2016) 698-703.
[203] X. Liu, R. Jervis, R.C. Maher, I.J. Villar‐Garcia, M. Naylor‐Marlow, P.R. Shearing, M. Ouyang, L. Cohen, N.P. Brandon, B. Wu, 3D‐Printed Structural Pseudocapacitors, Advanced Materials Technologies 1(9) (2016) 1600167.
[204] X. Wang, Y. Chen, O.G. Schmidt, C. Yan, Engineered nanomembranes for smart energy storage devices, Chemical Society Reviews 45(5) (2016) 1308-1330.
[205] F. Soavi, L.G. Bettini, P. Piseri, P. Milani, C. Santoro, P. Atanassov, C. Arbizzani, Miniaturized supercapacitors: key materials and structures towards autonomous and sustainable devices and systems, Journal of power sources 326 (2016) 717-725.
[206] K. Sun, T.S. Wei, B.Y. Ahn, J.Y. Seo, S.J. Dillon, J.A. Lewis, 3D printing of interdigitated Li‐Ion microbattery architectures, Advanced Materials 25(33) (2013) 4539-4543.
[207] K. Fu, Y. Wang, C. Yan, Y. Yao, Y. Chen, J. Dai, S. Lacey, Y. Wang, J. Wan, T. Li, Graphene oxide‐based electrode inks for 3D‐printed lithium‐ion batteries, Advanced materials 28(13) (2016) 2587-2594.
[208] G. Xiong, C. Meng, R.G. Reifenberger, P.P. Irazoqui, T.S. Fisher, Graphitic Petal Micro‐Supercapacitor Electrodes for Ultra‐High Power Density, Energy Technology 2(11) (2014) 897-905.
[209] D.P. Dubal, O. Ayyad, V. Ruiz, P. Gomez-Romero, Hybrid energy storage: the merging of battery and supercapacitor chemistries, Chemical Society Reviews 44(7) (2015) 1777-1790.
[210] T. Tooming, T. Thomberg, H. Kurig, A. Jänes, E. Lust, High power density supercapacitors based on the carbon dioxide activated d-glucose derived carbon electrodes and 1-ethyl-3-methylimidazolium tetrafluoroborate ionic liquid, Journal of Power Sources 280 (2015) 667-677.
[211] G. Sun, J. An, C.K. Chua, H. Pang, J. Zhang, P. Chen, Layer-by-layer printing of laminated graphene-based interdigitated microelectrodes for flexible planar micro-supercapacitors, Electrochemistry Communications 51 (2015) 33-36.
[212] Y. Jiang, H. Shao, C. Li, T. Xu, Y. Zhao, G. Shi, L. Jiang, L. Qu, Versatile Graphene Oxide Putty‐Like Material, Advanced Materials 28(46) (2016) 10287-10292.
[213] L. Besra, M. Liu, A review on fundamentals and applications of electrophoretic deposition (EPD), Progress in materials science 52(1) (2007) 1-61.
[214] A.J. Pascall, F. Qian, G. Wang, M.A. Worsley, Y. Li, J.D. Kuntz, Light‐Directed electrophoretic deposition: a new additive manufacturing technique for arbitrarily patterned 3D composites, Advanced Materials 26(14) (2014) 2252-2256.
[215] K.T. Sullivan, C. Zhu, E.B. Duoss, A.E. Gash, D.B. Kolesky, J.D. Kuntz, J.A. Lewis, C.M. Spadaccini, Controlling material reactivity using architecture, Advanced Materials 28(10) (2016) 1934-1939.
[216] L. Ye, K. Wen, Z. Zhang, F. Yang, Y. Liang, W. Lv, Y. Lin, J. Gu, J.H. Dickerson, W. He, Highly efficient materials assembly via electrophoretic deposition for electrochemical energy conversion and storage devices, Advanced Energy Materials 6(7) (2016) 1502018.
[217] D. Pech, M. Brunet, H. Durou, P. Huang, V. Mochalin, Y. Gogotsi, P.-L. Taberna, P. Simon, Ultrahigh-power micrometre-sized supercapacitors based on onion-like carbon, Nature nanotechnology 5(9) (2010) 651-654.
[218] K. Lee, H. Lee, Y. Shin, Y. Yoon, D. Kim, H. Lee, Highly transparent and flexible supercapacitors using graphene-graphene quantum dots chelate, Nano Energy 26 (2016) 746-754.
[219] R. Qiang, K. Hou, J. Wang, S. Yang, Smooth and dense graphene quantum dots-based lubricating coatings prepared by electrophoretic deposition, Applied Surface Science (2020) 145338.

[220] W. Qian, M. Cao, F. Xie, C. Dong, Thermo-electrochemical cells based on carbon nanotube electrodes by electrophoretic deposition, Nano-micro letters 8(3) (2016) 240-246.
[221] J.A. Hondred, I.L. Medintz, J.C. Claussen, Enhanced electrochemical biosensor and supercapacitor with 3D porous architectured graphene via salt impregnated inkjet maskless lithography, Nanoscale Horizons 4(3) (2019) 735-746.
[222] H. Zhang, P.V. Braun, Three-dimensional metal scaffold supported bicontinuous silicon battery anodes, Nano letters 12(6) (2012) 2778-2783.
[223] J.H. Pikul, H.G. Zhang, J. Cho, P.V. Braun, W.P. King, High-power lithium ion microbatteries from interdigitated three-dimensional bicontinuous nanoporous electrodes, Nature communications 4(1) (2013) 1-5.
[224] S.R. Gowda, A. Leela Mohana Reddy, X. Zhan, H.R. Jafry, P.M. Ajayan, 3D nanoporous nanowire current collectors for thin film microbatteries, Nano letters 12(3) (2012) 1198-1202.
[225] C. Zhu, T. Liu, F. Qian, W. Chen, S. Chandrasekaran, B. Yao, Y. Song, E.B. Duoss, J.D. Kuntz, C.M. Spadaccini, 3D printed functional nanomaterials for electrochemical energy storage, Nano Today 15 (2017) 107-120.
[226] X. Chen, N. Brandon, P. Childs, B. Wu, X. Liu, Design and fabrication of a low cost desktop electrochemical 3D printer, (2018).
[227] J. Kretschmer, The Ink Cartridge as a Major Component of an InkJet System, NIP & Digital Fabrication Conference, Society for Imaging Science and Technology, 2001, pp. 43-48.
[228] X. Chen, X. Liu, M. Ouyang, J. Chen, O. Taiwo, Y. Xia, P.R. Childs, N.P. Brandon, B. Wu, Multi-metal 4D printing with a desktop electrochemical 3D printer, Scientific reports 9(1) (2019) 1-9.
[229] F. Haque, M. Rahman, E. Ahmed, P. Bakshi, A. Shaikh, A cyclic voltammetric study of the redox reaction of Cu (II) in presence of ascorbic acid in different pH media, Dhaka University Journal of Science 61(2) (2013) 161-166.
[230] D. Grujicic, B. Pesic, Electrodeposition of copper: the nucleation mechanisms, Electrochimica acta 47(18) (2002) 2901-2912.
[231] F.A. Lowenheim, Electroplating--Fundamentals of Surface Finishing, McGraw-Hill Book Co., New York. 1978, 560 (1978).
[232] M.T. Molares, V. Buschmann, D. Dobrev, R. Neumann, R. Scholz, I.U. Schuchert, J. Vetter, Single‐crystalline copper nanowires produced by electrochemical deposition in polymeric ion track membranes, Advanced Materials 13(1) (2001) 62-65.
[233] M.-Z. Zhang, M. Wang, Z. Zhang, J.-M. Zhu, R.-W. Peng, N.-B. Ming, Periodic structures of randomly distributed Cu/Cu2O nanograins and periodic variations of cell voltage in copper electrodeposition, Electrochimica acta 49(14) (2004) 2379-2383.
[234] J. Yeung, L.C. Keong, Hardness measurement of copper bonding wire, Procedia Engineering 75 (2014) 134-139.
[235] L. Lu, Y. Shen, X. Chen, L. Qian, K. Lu, Ultrahigh strength and high electrical conductivity in copper, Science 304(5669) (2004) 422-426.
[236] S. Morsali, S. Daryadel, Z. Zhou, A. Behroozfar, D. Qian, M. Minary-Jolandan, Multi-physics simulation of metal printing at micro/nanoscale using meniscus-confined electrodeposition: Effect of environmental humidity, Journal of Applied Physics 121(2) (2017) 024903.
[237] C. Ponce de Leon, R. Field, On the determination of limiting current density from uncertain data, Journal of applied electrochemistry 30(9) (2000) 1087-1090.
[238] F. Li, Z. Gao, L. Li, Y. Chen, Microstructural study of MMC layers produced by combining wire and coaxial WC powder feeding in laser direct metal deposition, Optics & Laser Technology 77 (2016) 134-143.
[239] B. Onuike, B. Heer, A. Bandyopadhyay, Additive manufacturing of Inconel 718—copper alloy bimetallic structure using laser engineered net shaping (LENS™), Additive Manufacturing 21 (2018) 133-140.
[240] D.C. Hofmann, J. Kolodziejska, S. Roberts, R. Otis, R.P. Dillon, J.-O. Suh, Z.-K. Liu, J.-P. Borgonia, Compositionally graded metals: A new frontier of additive manufacturing, Journal of Materials Research 29(17) (2014) 1899-1910.

[241] A. Kobelev, V. Lysak, V. Chernyshev, Proizvodstvo metallicheskikh sloistykh kompozitsionnykh materialov, Production of Laminar Metallic Composites), Moscow: Intermet Engineering, 2002.
[242] B.G. Thomas, Modeling of the continuous casting of steel—past, present, and future, Metallurgical and materials transactions B 33(6) (2002) 795-812.
[243] B. Crossland, Explosive welding of metals and its application, (1982).
[244] A. Sharif Ullah, A. Fuji, A. Kubo, J.i. Tamaki, M. Kimura, On the surface metrology of bimetallic components, Machining Science and Technology 19(2) (2015) 339-359.
[245] D. Pan, K. Gao, J. Yu, Cold roll bonding of bimetallic sheets and strips, Materials science and technology 5(9) (1989) 934-939.
[246] A. Bykov, Bimetal production and applications, Steel in Translation 41(9) (2011) 778.
[247] F. Cverna, ASM ready reference: thermal properties of metals, ASM International2002.
[248] T.W. Clyne, S.C. Gill, Residual stresses in thermal spray coatings and their effect on interfacial adhesion: a review of recent work., Journal of Thermal Spray Technology 5(4) (1996).
[249] <http://www-ferp.ucsd.edu/LIB/PROPS/PANOS/cu.html>, (accessed 30/09/2020.2020).
[250] <http://www.matweb.com/search/DataSheet.aspx?MatGUID=e6eb83327e534850a062dbca3bc758dc&ckck=1>, (accessed 01/09/2020.2020).
[251] M.J. Aus, B. Szpunar, U. Erb, A.M. EL-Sherik, G. Palumbo, K.T. Aust, Electrical resistivity of bulk nanocrystalline nickel, Journal of applied physics 75(7) (1994) 3632-3634.
[252] B.C. Johnson, Electrical resistivity of copper and nickel thin‐film interconnections, Journal of Applied Physics 67(6) (1990) 3018-3024.
[253] K. Hung, C. Masarapu, T. Ko, B. Wei, Wide-temperature range operation supercapacitors from nanostructured activated carbon fabric, Journal of Power Sources 193(2) (2009) 944-949.
[254] A. Yu, V. Chabot, J. Zhang, Electrochemical supercapacitors for energy storage and delivery: fundamentals and applications, CRC press2013.
[255] X. Liu, C. Yin, J. Yang, M. Liang, J. Wei, Z. Zhang, H. Wang, Q. Wang, Controllable preparation of an eggshell membrane supported hydrogel electrolyte with thickness-dependent electrochemical performance, Journal of Materials Chemistry A 4(46) (2016) 17933-17938.
[256] X. Chen, X. Liu, M. Ouyang, P. Childs, N. Brandon, B. Wu, Electrospun composite nanofibre supercapacitors enhanced with electrochemically 3D printed current collectors, Journal of Energy Storage 26 (2019) 100993.
[257] F. Beguin, E. Frackowiak, Carbons for electrochemical energy storage and conversion systems, Crc Press2009.
[258] X. Liu, B. Wu, N. Brandon, Q. Wang, Tough Ionogel‐in‐Mask Hybrid Gel Electrolytes in Supercapacitors with Durable Pressure and Thermal Tolerances, Energy Technology 5(2) (2017) 220-224.
[259] Y.-C. Li, Y.S. Zhang, A. Akpek, S.R. Shin, A. Khademhosseini, 4D bioprinting: the next-generation technology for biofabrication enabled by stimuli-responsive materials, Biofabrication 9(1) (2016) 012001.
[260] A.M. Gaikwad, G.L. Whiting, D.A. Steingart, A.C. Arias, Highly flexible, printed alkaline batteries based on mesh‐embedded electrodes, Advanced materials 23(29) (2011) 3251-3255.
[261] L. Dai, D.W. Chang, J.B. Baek, W. Lu, Carbon nanomaterials for advanced energy conversion and storage, small 8(8) (2012) 1130-1166.
[262] Y.B. Tan, J.-M. Lee, Graphene for supercapacitor applications, Journal of Materials Chemistry A 1(47) (2013) 14814-14843.
[263] L.-F. Chen, Y. Lu, L. Yu, X.W.D. Lou, Designed formation of hollow particle-based nitrogen-doped carbon nanofibers for high-performance supercapacitors, Energy & Environmental Science 10(8) (2017) 1777-1783.
[264] L. Zhang, A. Aboagye, A. Kelkar, C. Lai, H. Fong, A review: carbon nanofibers from electrospun polyacrylonitrile and their applications, Journal of Materials Science 49(2) (2014) 463-480.

[265] X. Liu, M.N. Marlow, S.J. Cooper, B. Song, X. Chen, N.P. Brandon, B. Wu, Flexible all-fiber electrospun supercapacitor, Journal of Power Sources 384 (2018) 264-269.
[266] K. Tõnurist, A. Jänes, T. Thomberg, H. Kurig, E. Lust, Influence of mesoporous separator properties on the parameters of electrical double-layer capacitor single cells, Journal of The Electrochemical Society 156(4) (2009) A334-A342.
[267] Z. Yang, J. Deng, X. Chen, J. Ren, H. Peng, A highly stretchable, fiber‐shaped supercapacitor, Angewandte Chemie International Edition 52(50) (2013) 13453-13457.
[268] J. Yeo, G. Kim, S. Hong, M.S. Kim, D. Kim, J. Lee, H.B. Lee, J. Kwon, Y.D. Suh, H.W. Kang, Flexible supercapacitor fabrication by room temperature rapid laser processing of roll-to-roll printed metal nanoparticle ink for wearable electronics application, Journal of Power Sources 246 (2014) 562-568.
[269] K. Jost, D. Stenger, C.R. Perez, J.K. McDonough, K. Lian, Y. Gogotsi, G. Dion, Knitted and screen printed carbon-fiber supercapacitors for applications in wearable electronics, Energy & Environmental Science 6(9) (2013) 2698-2705.
[270] Y. Chen, J. Xu, Y. Yang, Y. Zhao, W. Yang, X. He, S. Li, C. Jia, Enhanced electrochemical performance of laser scribed graphene films decorated with manganese dioxide nanoparticles, Journal of Materials Science: Materials in Electronics 27(3) (2016) 2564-2573.
[271] C. Zhang, X. Geng, S. Tang, M. Deng, Y. Du, NiCo 2 O 4@ rGO hybrid nanostructures on Ni foam as high-performance supercapacitor electrodes, Journal of Materials Chemistry A 5(12) (2017) 5912-5919.
[272] A.A. Yadav, S. Jadhav, D. Chougule, P. Patil, U. Chavan, Y. Kolekar, Spray deposited Hausmannite Mn3O4 thin films using aqueous/organic solvent mixture for supercapacitor applications, Electrochimica Acta 206 (2016) 134-142.
[273] C. Zhao, C. Wang, R. Gorkin Iii, S. Beirne, K. Shu, G.G. Wallace, Three dimensional (3D) printed electrodes for interdigitated supercapacitors, Electrochemistry Communications 41 (2014) 20-23.
[274] X. Tian, J. Jin, S. Yuan, C.K. Chua, S.B. Tor, K. Zhou, Emerging 3D‐printed electrochemical energy storage devices: a critical review, Advanced Energy Materials 7(17) (2017) 1700127.
[275] R.H. Dettre, R.E. Johnson Jr, Contact Angle Hysteresis. IV. Contact Angle Measurements on Heterogeneous Surfaces1, The journal of physical chemistry 69(5) (1965) 1507-1515.
[276] A.M. Coclite, Y. Shi, K.K. Gleason, Super-hydrophobic and oloephobic crystalline coatings by initiated chemical vapor deposition, Physics procedia 46 (2013) 56-61.

Appendices

Xiaolong Chen, Billy Wu, Peter Childs

Dyson School of Design Engineering, Imperial College London, UK

Appendix A FDM 3D printed parts for the print unit of Desktop Electrochemical 3D Printer

A.1 part 1 of print cartridge

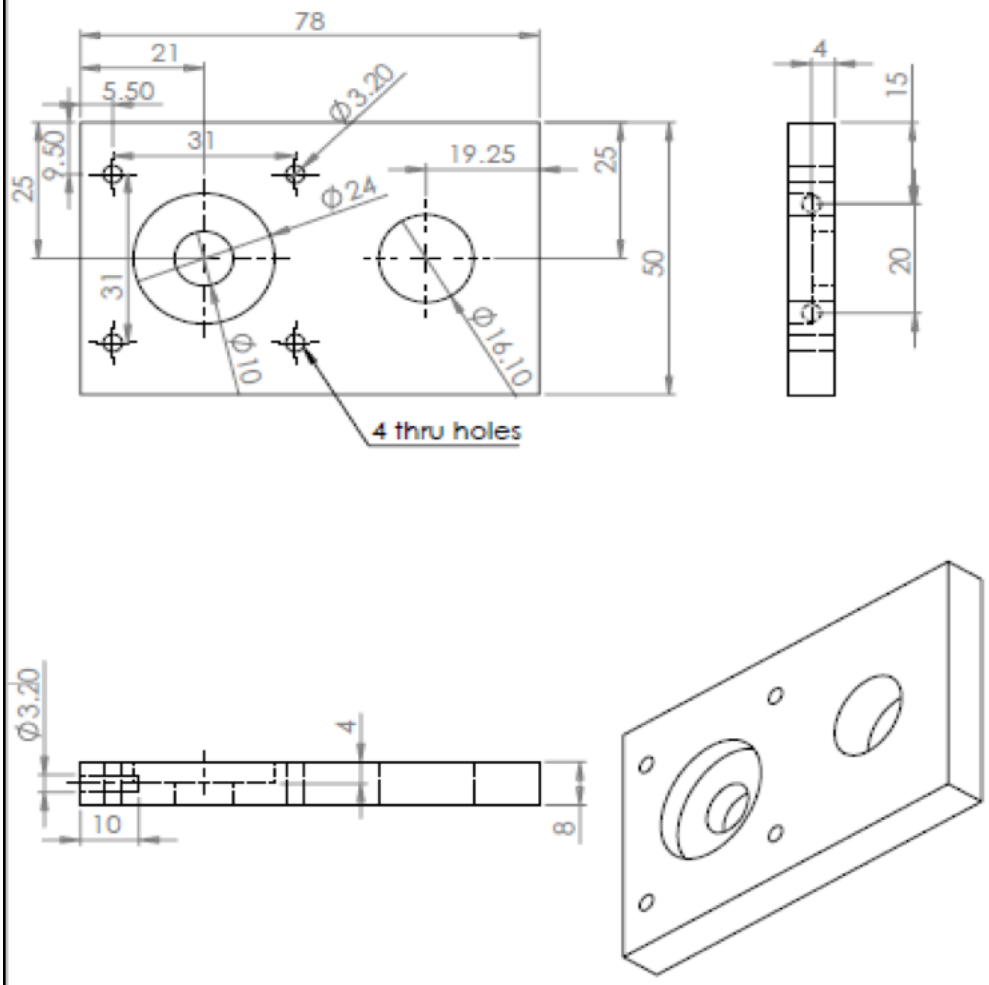

- **Manufacturing Method: FDM 3D Printing**
- **Use Drawing with CAD Model provided**
- **Dimensions Tolerances +/-0.1mm unless stated otherwise**
- **All Dimensions are in Millimetres (mm)**

Dyson School of Design Engineering	**NAME**	X.Chen	**Title**	Cartridge_ 1
	Date	23/04/2015	**Scale**	2:1
	Programme	PhD research	**Material**	ABS
Imperial college London	Email: x.chen15@imperial.ac.uk			

A.2 part 2 of print cartridge

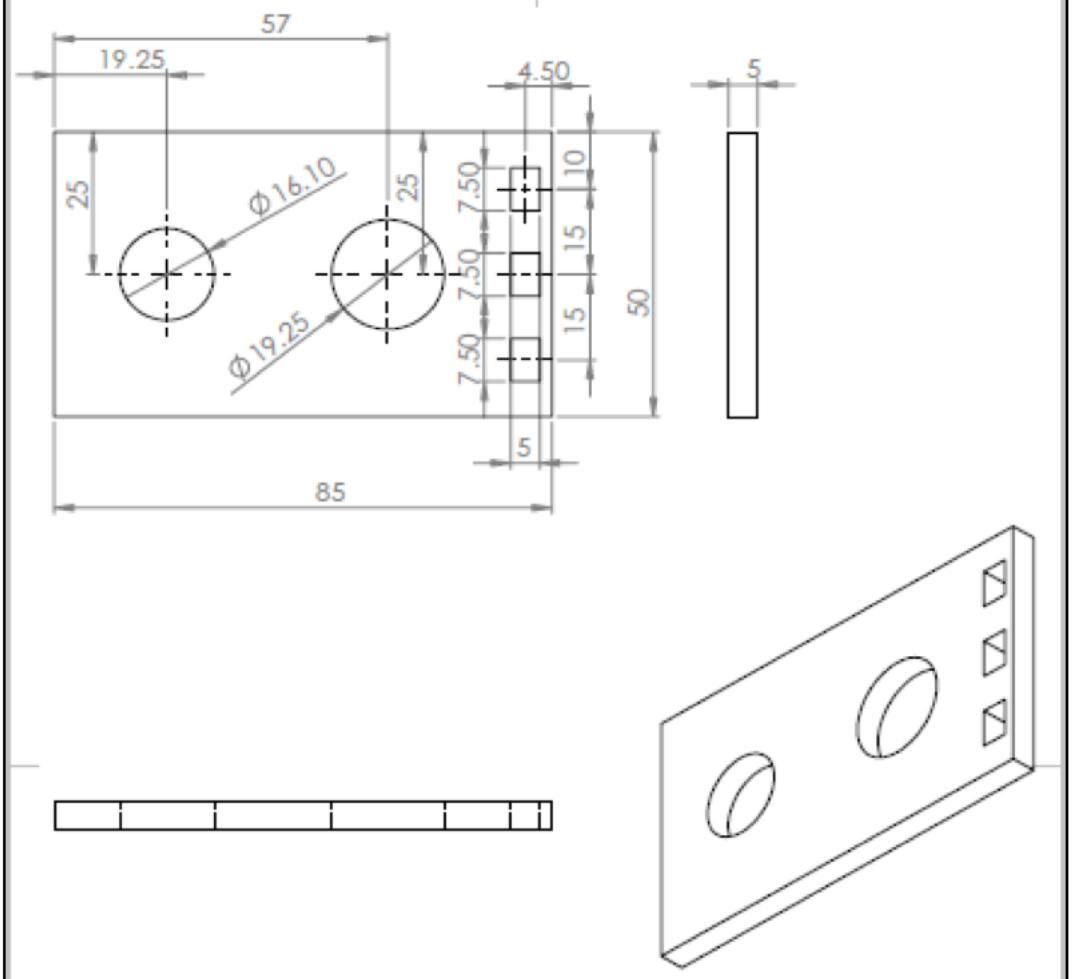

- **Manufacturing Method: FDM 3D Printing**
- **Use Drawing with CAD Model provided**
- **Dimensions Tolerances +/-0.1mm unless stated otherwise**
- **All Dimensions are in Millimetres (mm)**

Dyson School of Design Engineering	**NAME**	X.Chen	**Title**	Cartridge_ 2
	Date	23/04/2015	**Scale**	2:1
	Programme	PhD research	**Material**	ABS
Imperial college London	Email: x.chen15@imperial.ac.uk			

A.3 part 3 of print cartridge

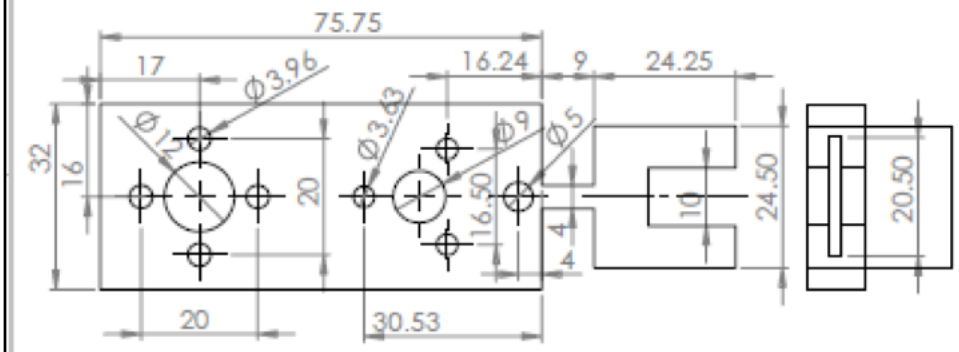

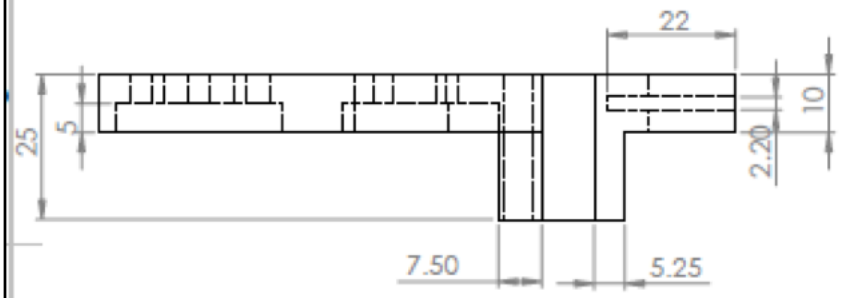

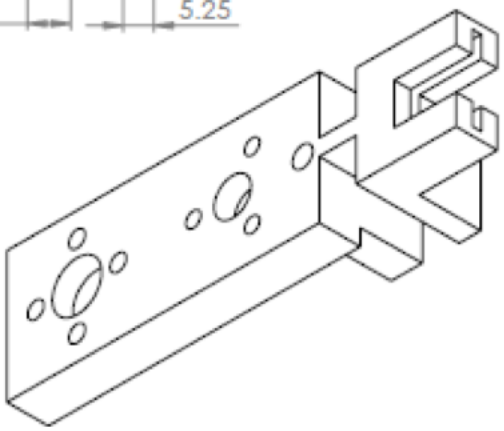

- **Manufacturing Method: FDM 3D Printing**
- **Use Drawing with CAD Model provided**
- **Dimensions Tolerances +/- 0.1mm unless stated otherwise**
- **All Dimensions are in Millimetres (mm)**

Dyson School of Design Engineering	**NAME**	X.Chen	**Title**	Cartridge_ 3
	Date	23/04/2015	**Scale**	2:1
	Programme	PhD research	**Material**	ABS
Imperial college London	Email: x.chen15@imperial.ac.uk			

A.4 part 4 of print cartridge

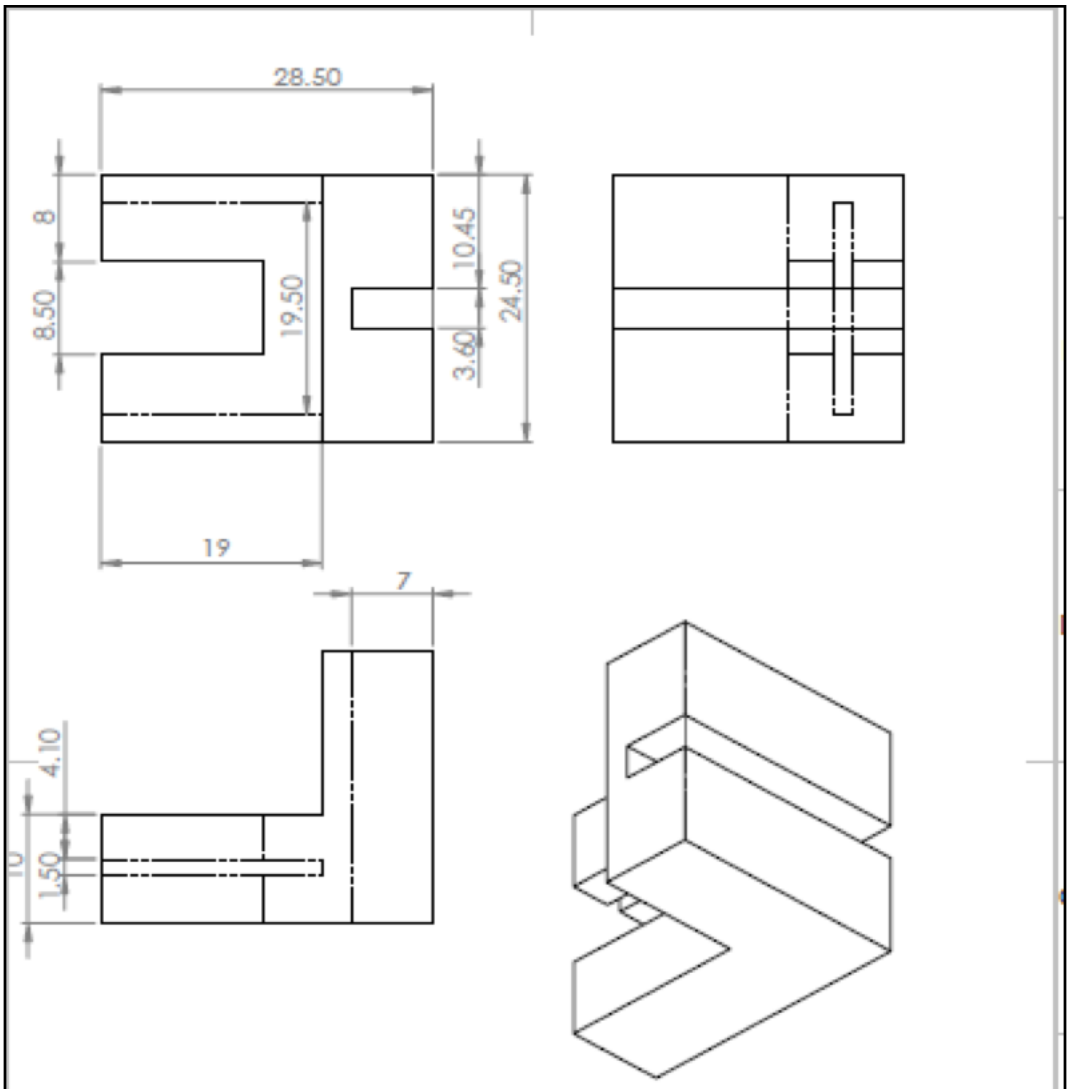

- **Manufacturing Method: FDM 3D Printing**
- **Use Drawing with CAD Model provided**
- **Dimensions Tolerances +/-0.1mm unless stated otherwise**
- **All Dimensions are in Millimetres (mm)**

Dyson School of Design Engineering	**NAME**	X.Chen	**Title**	Cartridge_ 4
	Date	23/04/2015	**Scale**	2:1
	Programme	PhD research	**Material**	ABS
Imperial college London	Email: x.chen15@imperial.ac.uk			

A.5 Adapter for dual print heads

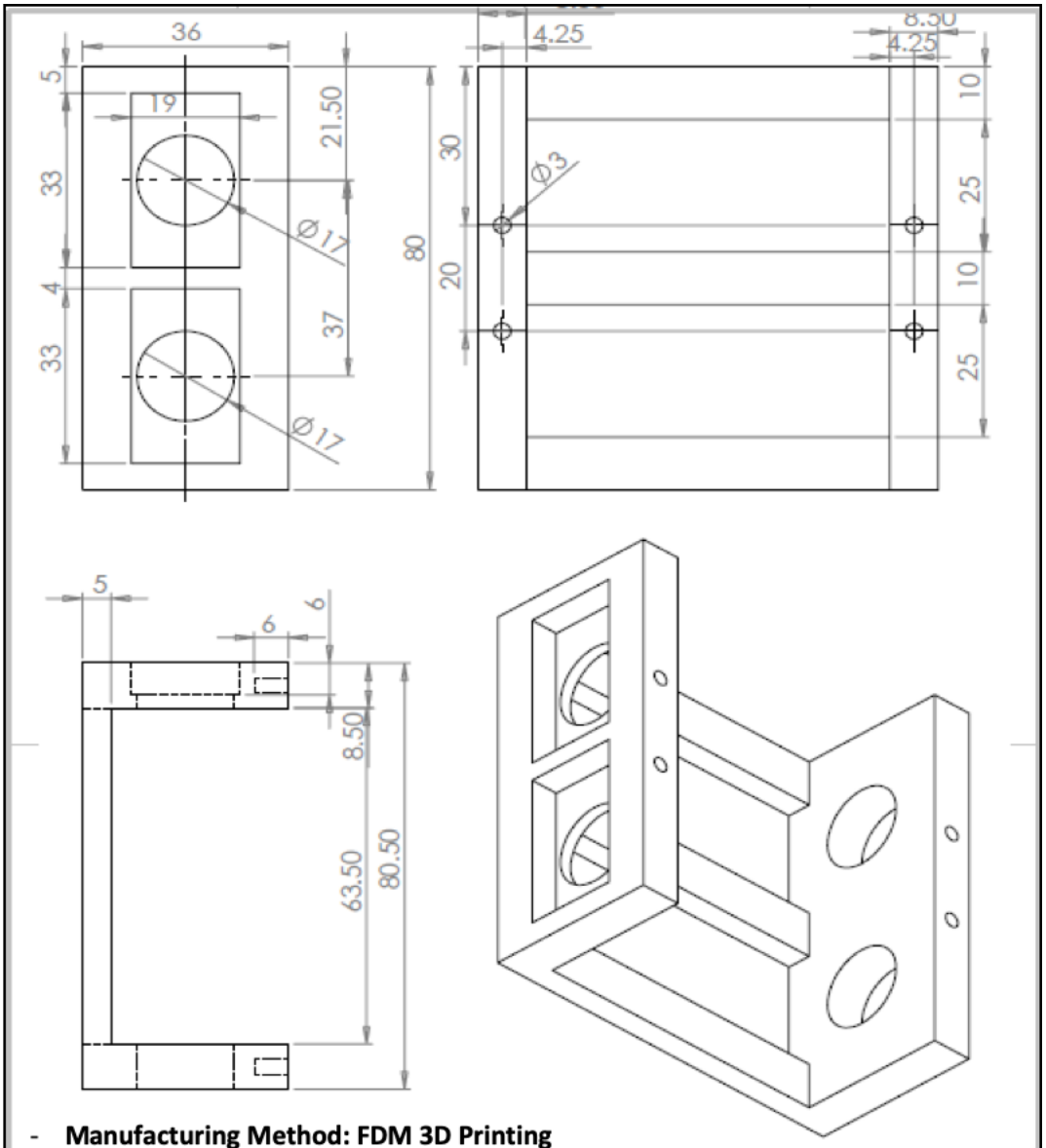

- **Manufacturing Method: FDM 3D Printing**
- **Use Drawing with CAD Model provided**
- **Dimensions Tolerances +/-0.1mm unless stated otherwise**
- **All Dimensions are in Millimetres (mm)**

Dyson School of Design Engineering	**NAME**	X.Chen	**Title**	Adapter for dual print head
	Date	23/04/2015	**Scale**	2:1
Imperial college London	**Programme**	PhD research	**Material**	ABS
	Email: x.chen15@imperial.ac.uk			

Appendix B Purchased list for Desktop Electrochemical 3D Printer

Sub-systems	Item	Supplier
Print system	10ml polypropylene dispensing syringe	RS (Metcal-7100LL1NPK)
	400 μm polypropylene nozzle	RS (Metcal-7922125DHUV)
	Sanyo Denki Stepper motor (for screw rotation and material section unit).	RS
	Polymide (Nylon) for the fabricated syringe holder	UPs
	Copper rods serve as electrodes	RS
	Portable USB digital 1000x microscope	Amazon
Moving system	WER Me Creator fused deposition modelling 3D printer	Amazon
	Replaced Sanyo Denki stepper motor for actuation in x, y and z axes	IGUS
	Replaced Arduino control board	IGUS
Chemicals	Anhydrous Copper sulfate electrolyte (≥ 99.99%)	Sigma-Aldrich
	Anhydrous Nickel chloride powder	Sigma-Aldrich
	Anhydrous Nickel sulfate powder	Sigma-Aldrich
	Boric acid powder	Sigma-Aldrich

Appendix C Total cost of Desktop Electrochemical 3D Printer

Item	Cost
WER Me Creator fused deposition modelling 3D printer	£300
Arduino Control Board	£55
Portable USB digital 1000x microscope	£17
Dispensing syringe	£23
nozzle	£19
4 Sanyo Denki Stepper motors	£150
Total: £564	

Appendix D Copyright permission table

Page No.	Type of work:	Name of work	Source of work	Copyright holder and contact	permission requested on	I have permission yes /no	Permission note
30	Figure	Figure 2.13 (a)	A practical beginner's guide to cyclic voltammetry. *Journal of Chemical Education*, *95*(2), pp.197-206.	Copyright © 2017 The American Chemical Society and Division of Chemical Education, Inc	02.01.2020	yes	Permission is attached in Appendix D.1
30	Figure	Figure 2.13 (b)	Meniscus Controlled Three-Dimensional Nanofabrication, Department of Mechanical Science and Engineering, University of Illinois, Urbana-Champaign, 2007.	University of Illinois Library	02.01.2020	yes	Permission is attached in Appendix D.2
Chapter 3	Manuscript reuse for thesis	Design and fabrication of a low-cost electrochemical 3D printer	***3****rd International Conference on Progress in Additive Manufacturing (Pro-AM),* Singapore	Copyright © NTU Library	02.01.2020	yes	From the NTU library reply, as the author of Elsevier article, you retain the right to include it in a thesis or dissertation, provided it is not published commercially. Permission is not required. Email reply is attached in Appendix D.3.
Chapter 4	Manuscript reuse for thesis	A low cost desktop electrochemical metal 3D printer.	*Advanced Materials Technologies*, *2*(10), p.1700148.	© Wiley permissions@wiley.com	28.12.19	yes	Permission is attached in Appendix D.4

Chapter 5	Manuscript reuse for thesis	Multi-metal 4D printing with a desktop electrochemical 3D printer.	*Scientific reports*, *9*(1), p.3973.	© 2019 Springer Nature Limited	27.12.19	yes	*Scientific Reports* does not require authors to assign copyright of their published original research papers to the journal. See the link: https://www.nature.com/srep/journal-policies/editorial-policies#license-agreement
Chapter 6	Manuscript reuse for thesis	Electrospun composite nanofibre supercapacitors enhanced with electrochemically 3D printed current collectors.	*Journal of Energy Storage*, *26*, p.100993.	Copyright © 2019 Elsevier	28.12.19	yes	As the author of Elsevier article, you retain the right to include it in a thesis or dissertation, provided it is not published commercially. Permission is not required. https://www.elsevier.com/about/policies/copyright#Author-rights

D.1

ACS Chemistry for Life®

Dear Dr. Xiaolong,

Thank you for contacting ACS Publications Support.

Your permission requested is granted and there is no fee for this reuse. In your planned reuse, you must cite the ACS article as the source, add this direct link https://pubs.acs.org/doi/10.1021/acs.jchemed.7b00361, and include a notice to readers that further permissions related to the material excerpted should be directed to the ACS.

If you need further assistance, please let me know.

Thank you,

Ranjith Alexander

ACS Customer Services & Information

Incident Information:

Incident #:	3231588
Date Created:	2020-01-02T19:33:05
Priority:	3
Customer:	Xiaolong Chen
Title:	permission enquires for reuse a figure and part of content from ACS article
Description:	Dear Editor, I am Xiaolong Chen, a PhD student at Imperial College London. I would like to re-use figure 3(H), and contents in section 'UNDERSTANDING THE SIMPLE VOLTAMMOGRAM' in an article 'A Practical Beginner's Guide to Cyclic Voltammetry' (https://pubs.acs.org/doi/pdf/10.1021/acs.jchemed.7b00361) for my PhD thesis.

D.2

Request to reproduce an extract from a third party's published work

02/01/2020

Dear Abhijit Suryavanshi,

I am completing my PhD thesis at Imperial College London entitled 'Electrochemical Metal 3D Printing'.

I seek your permission to reprint, in my thesis an extract from: "Meniscus Controlled Three-Dimensional Nanofabrication," Ph. D., Department of Mechanical Science and Engineering, University of Illinois at Urbana-Champaign, 2007. The extract to be reproduced is: Figure 2.7 (b) Cyclic voltammetry plot acquired in ec-FPN for 5 mM Q1SO4 (pH = 1) with respect to a AgCl reference electrode at a scan rate of 100 mV/s.

I would like to include the extract in my thesis which will be added to Spiral, Imperial's institutional repository http://spiral.imperial.ac.uk/ and made available to the public under a Creative Commons Attribution-NonCommercial 4.0 International Licence (CC BY-NC)

If you are happy to grant me all the permissions requested, please return a signed copy of this letter. If you wish to grant only some of the permissions requested, please list these and then sign.

Yours sincerely,

Xiaolong Chen

[redacted]

Permission granted for the use requested above:

I confirm that I am the copyright holder of the extract above and hereby give permission to include it in your thesis which will be made available, via the internet, for non-commercial purposes under the terms of the user licence.

Signed: [redacted]

Name: Abhijit Suryavanshi

Organisation: T-mobile

Job title: Principal Statistician

D.3

Gmail

Fwd: [NTU Library] ask for copyright permission

10 March 2020 at 12:20

From: **NTU Library** <library@ntu-sg.libanswers.com>
Date: Tue, Mar 10, 2020 at 6:27 AM
Subject: [NTU Library] ask for copyright permission
To: Xiaolong Chen <xiaolongchenphd@gmail.com>

--# Type your reply above this line #--

Bee Eng Er

Mar 10 2020, 02:27pm via System

Hi Xiaolong,

You are the copyright owner of the paper. You retain the right to include it in a thesis or dissertation, provided it is not published commercially.
Permission is not required.

Thank you,

Bee Eng (beeeng@ntu.edu.sg)

Original Question

Feb 27 2020, 12:45am via Email

ask for copyright permission
Dear Sir/Madam

I am completing my PhD thesis at Imperial College London entitled 'Electrochemical Metal 3D Printing'.

I seek your permission to reprint my previous conference paper 'Design and fabrication of a low cost desktop electrochemical 3D printer' publicated at Pro-AM conference, in my thesis. the link is https://dr.ntu.edu.sg/handle/10356/88560.

I would like to include the extract in my thesis which will be added to Spiral, Imperial's institutional repository http://spiral.imperial.ac.uk/ and made available to the public under a Creative Commons Attribution-NonCommercial 4.0 International Licence (CC BY-NC)

If you are happy to grant me all the permissions requested, please return a signed copy of this letter. If you wish to grant only some of the permissions requested, please list these and then sign.

Yours sincerely,

Xiaolong Chen

Attached Files

- enquiries_for_copyright_permission_form.docx

Email address of requestor:
Thank you for contacting NTU Library!

D.4

JOHN WILEY AND SONS LICENSE
TERMS AND CONDITIONS

Mar 10, 2020

This Agreement between imperial college london -- xiaolong chen ("You") and John Wiley and Sons ("John Wiley and Sons") consists of your license details and the terms and conditions provided by John Wiley and Sons and Copyright Clearance Center.

License Number	4740790630547
License date	Jan 02, 2020
Licensed Content Publisher	John Wiley and Sons
Licensed Content Publication	Advanced Materials Technologies
Licensed Content Title	A Low Cost Desktop Electrochemical Metal 3D Printer
Licensed Content Author	Billy Wu, Nigel Brandon, Peter Childs, et al
Licensed Content Date	Aug 28, 2017
Licensed Content Volume	2
Licensed Content Issue	10
Licensed Content Pages	6
Type of use	Dissertation/Thesis
Requestor type	Author of this Wiley article

Format	Electronic
Portion	Full article
Will you be translating?	No
Title of your thesis / dissertation	Electrochemical Metal 3D Printing
Expected completion date	Jan 2020
Expected size (number of pages)	130
Requestor Location	imperial college london Lensfield Rd, Cambridge Cambridge, Cambridgeshire CB2 1EW United Kingdom Attn: imperial college london
Publisher Tax ID	EU826007151
Total	0.00 GBP

Terms and Conditions

TERMS AND CONDITIONS

This copyrighted material is owned by or exclusively licensed to John Wiley & Sons, Inc. or one of its group companies (each a"Wiley Company") or handled on behalf of a society with which a Wiley Company has exclusive publishing rights in relation to a particular work (collectively "WILEY"). By clicking "accept" in connection with completing this licensing transaction, you agree that the following terms and conditions apply to this transaction (along with the billing and payment terms and conditions established by the Copyright Clearance Center Inc., ("CCC's Billing and Payment terms and conditions"), at the time that you opened your RightsLink account (these are available at any time at http://myaccount.copyright.com).